# Efficient pheromone navigation via antagonistic detectors

Xuan Wan[1,2], Tingtao Zhou*[3,4], Vladislav Susoy*[5], Core Francisco Park[5], Alessandro Groaz[1,2], John F. Brady[3,4], Aravinthan D.T. Samuel[5], Paul W. Sternberg†[1,2].

*These authors contributed equally to this work.
† corresponding author

1. Division of Biology and Biological Engineering, California Institute of Technology, Pasadena, CA 91125, USA.
2. Tianqiao and Chrissy Chen Institute for Neuroscience, California Institute of Technology, Pasadena, CA 91125, USA.
3. Division of Engineering and Applied Science, California Institute of Technology, Pasadena, CA 91125, USA.
4. Division of Chemistry and Chemical Engineering, California Institute of Technology, Pasadena, CA 91125, USA.
5. Department of Physics and Center for Brain Science, Harvard University, Cambridge, MA, USA

Author information:

| Name | Email | ORCID |
|---|---|---|
| Xuan Wan | wanxuan@caltech.edu | 0000-0002-6165-6340 |
| Tingtao Zhou | tingtaoz@caltech.edu | 0000-0002-1766-719X |
| Vladislav Susoy | vladislav_susoy@fas.harvard.edu | 0000-0002-0669-0087 |
| Core Francisco Park | corefranciscopark@g.harvard.edu | 0000-0002-9542-2913 |
| Alessandro Groaz | agroaz@caltech.edu | 0000-0002-3873-7409 |
| John F. Brady | jfbrady@caltech.edu | 0000-0001-5817-9128 |
| Aravinthan D.T. Samuel | samuel@g.harvard.edu | 0000-0002-1672-8720 |
| Paul W. Sternberg | pws@caltech.edu | 0000-0002-7699-0173 |


**Abstract**

Chemotaxis to a potential mate who is moving and emitting a volatile sex pheromone poses a navigation challenge that requires rapid, precise responses to maximize reproductive success. We demonstrate that *Caenorhabditis elegans* males address this challenge by utilizing two pheromone detectors located in head and tail sensory neurons. Despite sharing a receptor SRD-1, AWA head neurons promote forward movement and acceleration, while tail PHD neurons induce reversals and deceleration. In increasing pheromone gradients AWA dominates; whereas weakening gradients inactivate AWAs, allowing PHDs to fine-tune the response and correct the path. Head AWAs are essential for mate-searching, while tail PHDs are crucial for complex tasks. The navigation mode and velocity adapt as males climb a pheromone gradient. A minimal-parameter computational model recapitulates key findings and illuminates the interplay between head and tail signals in adaptive navigation.

**Keywords:** sensory integration, chemotaxis modeling, sex pheromone, orthokinesis, sexual dimorphism

## Introduction

In the animal kingdom, finding a mate presents an essential task. This is an especially significant challenge for those organisms that rely on volatile pheromones for mate detection, as the potential mate often moves in a complex environment and establishes a gradient of pheromones that is fleeting and at low concentration. To obtain a mechanistic understanding of how animals can rise to this challenge, we sought to study navigation in *C. elegans* as it has a highly accessible nervous system. *C. elegans* males are well able to locate their mates, initially self-fertilizing hermaphrodites that emit a volatile pheromone when sperm are depleted and are thus essentially females [1-5].

These chemosensory signals are fundamental across diverse species, facilitating complex behaviors such as strategic navigation, active sampling, and sequential decision-making; they are crucial for reproductive success [6-8]. *C. elegans* produces both soluble and volatile sex attractants. Soluble nematode-specific ascarosides, glycosides of the dideoxy sugar ascarylose, are modulators of social/sexual behaviors and developmental regulation [9-27]. In addition, one or more volatile, as yet unidentified non-ascaroside sex pheromones (referred to as sex pheromone here) facilitate sexual communication by signaling fertility and sexual maturity [3, 4]. Only hermaphrodites bearing no sperm – because of depletion or dysfunction – can produce sex pheromone. Hermaphrodites with no sperm can be considered females, and thus here we refer to the pheromone as female sex pheromone. The one known receptor for sex pheromone is the G protein-coupled receptor (GPCR) SRD-1; it is expressed in the sex-shared amphid neuron AWA only in males implying underlying sexually dimorphic sensory processing [5]. In other animals, volatile sex pheromones guide both innate and learned mate-searching activities and provide an opportunity to study the neurobiological underpinnings of sexually dimorphic behaviors. The differential responses of males and females to identical stimuli, such as sex pheromones, also raise questions about the sensory and neural circuit bases of sexual dimorphism in behavior. Despite the recognition of the role of sex pheromones in various organisms, including insects, fish, and mammals, our understanding of the intricate molecular and neural mechanisms that mediate these behaviors remains incomplete. This gap is partly due to the limited knowledge of the molecular mechanism and neuronal assemblies responsive to pheromonal cues, which are crucial for the decoding of odor perception and driving sex-specific behaviors.

The complexity of neural circuit questions makes studies in simple models such as *C. elegans* highly useful to rigorously define neural algorithms used by animals. The neural circuitry underlying chemoattraction in *C. elegans* has been mapped with increasing precision, suggesting that sensory neurons process environmental stimuli with remarkable reliability [28]. It also has a network of interneurons that plays critical roles in processing sensory information and guiding behavioral responses that collectively facilitate navigation and avoidance behaviors: AIA amplifies olfactory signals, AIB controls reversals, AIY mediates response to gradients, AIZ modulates turns, and AVA initiates backward movement [29-37]. These circuits facilitate essential survival behaviors, employing mechanisms such as temporal integration [28], rapid desensitization [38], and the modulation of behavioral responses based on previous experiences and current conditions [29, 33, 39-50]. The probabilistic nature of behavioral outcomes in *C. elegans* can be traced to the dynamic state of the neural network beyond sensory neurons, potentially explaining the variability in behavior outcomes from identical stimuli in the same individual [39, 51].

*C. elegans* exhibits a remarkable ability to navigate complex environments using chemical cues. Three established navigation strategies have been observed in this organism [52-58]: (1) Klinokinesis: A

random walk biased toward the stimulus, such as in bacterial chemotaxis, requires comparing concentrations over time and adjusting turning rate based on the comparison. However, it lacks directionality in the new heading. (2) Klinotaxis: A more refined navigation, it utilizes directional turns to achieve more accurate gradient navigation [52, 59-62]. (3) Orthokinesis: The organism modulates its speed based on the stimulus intensity [52, 63-65].

Previous studies have shown that *C. elegans* employs sensory detectors on opposite sides of its body for rapid avoidance responses to aversive stimuli like SDS, H2O2, and glycerin [63, 65, 66], where quick response is prioritized over accuracy. In contrast, our study uncovers a novel volatile attractant chemotaxis mechanism in which these dual detectors are repurposed for target searching, a process that demands both rapid responses and high precision to successfully locate the target. Here, we describe a unique attractant dual-sampling that utilizes controlled expression of a single receptor to achieve two key outcomes: 1) sexually dimorphic chemosensory responses, and 2) an innate, adaptive navigation strategy for efficient volatile chemical chemotaxis.

## Main

### Volatile pheromone receptor SRD-1 is expressed in PHD, a male-specific neuron in the tail

Male *C. elegans* senses the volatile female sex pheromone via SRD-1 [3, 5], a GPCR. In males, SRD-1 is expressed in AWA and ASI sensory neurons of the anterior ganglia, whereas in hermaphrodites it is expressed only in ASI, not AWA. Additionally, in the hermaphrodite, SRD-1 is also expressed in the tail neuron PHA. In the male, SRD-1 has been reported to be expressed in a pair of tail neurons [67, 68], which we now have identified as the newly discovered pair of PHD neurons, based on their location, morphology, and marker gene expression (Figure 1A,B,D and S1B-C). We further verified SRD-1 expression in PHD neurons using a split cGAL driver with *lin-48d* and *srd-1* promoter, where *lin-48* is known to be expressed in PHD neurons [69]. This approach also generated a PHD-specific driver targeted manipulation of PHD neurons for subsequent experiments (Figure 1D). In *C. elegans* males, AWA has been shown required for chemotaxis towards the sex pheromone [3, 5]. While, previous studies have linked male tail-specific neuron PHD to various aspects of male behavior [69, 70], their specific function remains unclear.

AWA neurons are known to respond to multiple volatile attractants [56, 71-74], whereas PHA neurons are involved in repellent avoidance behaviors [56, 63, 75]. ASI mediates multiple sensory resp onses, including repulsion [76]. This sex-specific expression pattern of SRD-1 suggests that the differing behavioral responses to the sex pheromone—strong attraction in males and weak repulsion in hermaphrodites—may result from the sexually dimorphic expression of the chemoreceptor SRD-1. The dual-site expression of SRD-1 in both head and tail neurons suggests that males may integrate SRD-1-mediated sensory inputs from the anterior and posterior regions to navigate effectively toward the volatile pheromone. This integration of sensory information from dual detectors could be crucial for accurate and efficient navigation.

### Male-specific PHD is activated by the volatile pheromone

We next tested if PHD neurons activate in response to the sex pheromone. Sex pheromones were extracted from both *C. elegans* hermaphrodites and *C. remanei* females, and male tail neuron activity was recorded upon exposure. We observed that PHD is activated by the sex pheromone from both *C. elegans fog-2* hermaphrodites and *C. remanei* females (Figure 1C and S1D). To test if this response was mediated via SRD-1, we repeated the experiment in *srd-1(eh1)* loss-of-function mutant males. *srd-1* mutant males showed no PHD activation upon sex pheromone stimulation (Figure 1C). We conclude that

133 male-specific PHD neurons sense this volatile sex pheromone via SRD-1. These findings, combined with
134 the known role of PHD in mate-related behaviors [69], suggest its potential involvement in pheromone-
135 guided navigation. The SRD-1 mediated response in both head (AWA) and tail (PHD) neurons implies
136 males might utilize dual detectors for efficient navigation towards pheromone sources.
137
138 **PHD neurons enhance mate-searching efficiency in complex environments**
139 To test the hypothesis that these spatially separated detectors for pheromone aid navigation we used
140 four types of chemoattraction assays designed to replicate the varying levels of difficulty males might
141 encounter in natural conditions, comparing intact males to those with HisCl inhibited-PHD neurons. We
142 achieved specific expression of the HisCl effector (a chemogenetic silencer) in PHD under the control of a
143 split cGAL-UAS line: *lin-48d*p::NLS::cGAL (DBD); *srd-1*p::NLS::cGAL (AD). Our experimental design
144 included wild-type males and PHD-HisCl lines without histamine treatment as controls. Our data showed
145 no significant differences between the two control groups in their response to sex pheromones under all
146 test conditions (Figure 1D). Therefore, any observed effects can be attributed to the treatment-induced
147 inactivation of PHD neurons.
148
149 We first challenged PHD-inhibited males to locate a sex pheromone source placed at the same distance
150 (3 cm)from the source, using two different diameters (6 and 8 cm)agar-filled Petri dishes. All males
151 located the source within 30 mins (Figure 1D-c,d). PHD-inhibited males performed as effectively as
152 controls at both distances, indicating that tail neuron input is not essential for simple, close-range
153 navigation tasks. By contrast, when we placed males 5 cm from the source in an 8 cm-Petri dish, all test
154 subgroup males were unable to locate the source (Figure 1D-e).
155
156 We then tested males' ability to locate a more dilute odor. We diluted the sex pheromone concentration
157 10-fold and observed the responses of both WT, HisCl-untreated control, and PHD-inhibited males
158 (Figure 1D-f). PHD-inhibited males exhibited notable difficulties in identifying the diluted pheromone
159 source, unlike the two control group males. This differential response underscores the essential role of
160 male tail PHD neurons in navigating toward weak pheromone signals.
161
162 To understand the effects of increased distance versus stimulus dilution, we conducted Finite Element
163 Simulations of the pheromone concentration field (Figure S3). In our assay setup, the stimulus was
164 placed on the lid of the plate that was half-filled with agar, creating a bi-layer distribution of the
165 pheromone. As illustrated in Figure S3A, the volatile component diffuses rapidly in the air, while the agar
166 absorbs and then slowly releases the volatile component. The concentration field simulation revealed
167 that in experiments where males were positioned far away from the pheromone source, they
168 encountered areas of low absolute concentration without a clear gradient. Conversely, in experiments in
169 which males were nearer to a diluted pheromone source, a Gaussian distribution with a discernible
170 gradient was likely despite the overall low concentration (Figure S3B). These findings suggest that the
171 concentration gradient plays a crucial role in guiding males to the pheromone source.
172
173 Since *C. elegans* navigate through three-dimensional (3D) soil and rotting fruit in their natural habitat, we
174 examined the efficacy of PHD-inhibited males in a 3D search paradigm using gellan gum gel (see
175 Method), which likely better mimics natural conditions than a 2D Petri dish surface. In this endpoint
176 assay, we record the number of worms that reach the target spot every 5 mins. PHD-inhibited males had
177 reduced proficiency in identifying pheromone sources within 3D spaces, underscoring the importance of
178 PHD neuron inputs for environmental navigation that mirrors natural conditions (Figure 1D-g).
179

Analysis of the distribution of males at multiple timepoints after the addition of stimulus revealed a uniformly low chemotaxis index for the PHD-inhibited male group across all intervals in weak signal and 3D exploration tasks (Figure S2B). In our 2D experiments involving weak signals, most control males successfully located the target within 10 mins. However, in 3D exploration tasks, the peak arrival time at the target extended to a significantly longer 20 mins (Figure S2C). Notably, we observed distinct impairments in the navigational behaviors of PHD-inhibited males between weak signal detection and 3D spatial exploration tasks. In weak signal detection, the low chemotaxis index resulted from an equal distribution of males reaching both the test and control spots. Conversely, in 3D searching tasks, the low chemotaxis index stemmed from fewer males reaching both spots (Figure S2B-D).

Lastly, we tested PHD laser-ablated males in real female-seeking scenarios, targeting both uncoordinated *C. remanei* and actively moving *C. elegans fog-2 mutant* females, and quantified the search time, successful rate, and the mate attraction index (MAI) (See Method). These experiments increased search difficulty in two key aspects: the unpredictability of a free-moving target and the significantly higher sex pheromone emission levels of the dioecious species *C. remanei*, which can be up to 20 times greater than those of *C. elegans* [77]. As shown in Figures S2A and S4, PHD-ablated males showed no significate delay in locating immobile *C. remanei* female targets, with all males—both PHD-ablated and control—completing this task. However, when attempting to locate freely moving *C. elegans* females, which presented a greater navigational challenge due to unpredictable movements and weaker signals, PHD-ablated males experienced a minor delay (about 5min) and a lower success rate, with 51% successfully locating the targets compared to 67% of mock control males.

Together, these chemoattraction assays suggested that PHD neurons are likely crucial to real-world mate-searching, especially under more challenging conditions.

**Optogenetic dissection of SRD-1 positive neurons and PHD neuron's role in male locomotion**

To examine the effects of head versus tail SRD-1 positive neurons on sex pheromone-induced behavior, we used the red-shifted Chrimson variant of channelrhodopsin [78]. We first evaluated the UAS::Chrimson effector driven by a pan-neuronal promoter demonstrating the system's efficacy: worms temporarily ceased movement during light stimulation, promptly resuming normal behavior once the light was switched off (Figure S5A).

We then activated all SRD-1 positive neurons with Chrimson expressed under the *srd-1* regulatory control, using an *srd-1*p cGAL driver. The absence of ATR served as a control to negate any potential effects of light alone, confirming that the observed changes in velocity were attributable from targeted neuron activation. Under ATR+ conditions, males exhibited continuous forward movement throughout the 12.5s light stimulation period, transitioning to rapid steering or reduced speed after stimulation ceased, but not in ATR- males (Figure 2B and S5C). The hermaphrodite response was more variable, suggesting a sex-specific response to the activation of SRD-1 positive neurons (Figure 2B). To further confirm the role of SRD-1-positive neuron stimulation in modulating locomotor behaviors, we investigated the effects using extended stimulation protocols (30s or 60s light-on intervals followed by 10s light-off intervals). As shown in Figure 2D, during prolonged stimulation, forward movement was sustained, while turning behaviors remained consistently suppressed. Additionally, the cessation of stimulation was associated with reduced movement speed and an increase in turning rate, consistent with the observed dynamics under shorter stimulation conditions. Using the *odr-10*p cGAL driver to activate AWA neurons in both sexes showed no behavioral change, suggesting AWA activation alone does not drive forward motion or the *odr-10* promoter is insufficient (Figure S5B).

We next targeted PHD neurons exclusively. Using a split cGAL driver under the control of *lin-48d* and *srd-1* promoters to achieve PHD-specific Chrimson expression. Upon PHD activation, males elicited a decline in average velocity throughout the red light stimulation period, after which males resumed movement (Figures 2C and S5D). This result contrasts with the overall movement patterns observed upon and after the activation of all SRD-1 positive neurons (Figure 2B). Previous studies also suggest that PHD neurons have a potential role in maintenance of backward locomotion during the mating partner body scanning [69]. We also observed that repeated activation of PHD neurons also resulted in a gradual reduction in velocity (Figure 2C), suggesting a persistent slow down effect on locomotor behavior after activation.

Frequency spectrum analysis of total velocity during SRD-1-positive and PHD neuron stimulation revealed prominent peaks at 0.05 Hz and 0.025 Hz, corresponding to the 20 s and 40 s alternating stimulation protocols, respectively (Figure S5E). Notably, the peak amplitude was significantly higher in males compared to hermaphrodites under both stimulation protocols, indicating that the response pattern is more robust in males than in hermaphrodites.

**Head and tail neurons have distinct micro-behavioral responses to optogenetic activation**

To confirm and further investigate how activating SRD-1 positive neurons in the head versus the tail affects behavior, we targeted either the head or tail of freely moving males expressing *srd-1* Chrimson cGAL-UAS. As shown in Figures 2E and S6, we analyzed males' behavior in 2s intervals across four motifs: (1) forward, (2) backward, (3, 4) transitions between these two states. Initial observations showed that males predominantly moved forward without stimulation (Figure 2E).

Presentation of a short light pulse to the tail region, alternating every 2s over a 15-cycle period, induced a shift from forward to backward motion, with increased hesitancy in movement direction (Figure 2E). During periods of hesitation, males continually alternate between forward and backward movements. With 30 seconds of head stimulation, we noted behaviors analogous to those from activating all SRD-1 positive neurons, including persistent forward movement during light exposure followed by rapid directional adjustment (Figure 2E and S6). We also observed that after head stimulation, males exhibited self-exploratory behavior, using their tails to probe against their bodies, a behavior that can persist for several mins (Figure 2E). We chose this approach based on the distinct nature of the behaviors elicited by each stimulation. Tail stimulation primarily induces reversals, a rapid transition from forward to backward movement. To capture multiple reversals, we used short and repeated pulses. In contrast, head stimulation predominantly leads to sustained forward movement. To evaluate the duration and persistence of this response, we applied extended stimulation pulses.

**Circuit that combines head and tail inputs to control locomotion direction**

The male connectome [79] suggests locomotion command neurons as the likely locus of integration of the head and tail inputs. Specifically, PHDs have strong connections to EF and PVN interneurons [79], which connect to pre-motor command neurons (Figure 1B). The direction of locomotion is controlled by reciprocal inhibition of forward and reverse command neurons [29, 35, 80, 81]. To investigate the circuitry between sex pheromone sensory neurons and these motor command neurons, we specifically activated SRD-1 positive neurons with Chrimson and monitored pan-neuronal calcium dynamics using GCaMP6s (Figure 3A-C). SRD-1 positive neurons, including PHD, AWA, and ASI neurons in males, had robust responses to light stimulation (Figure 3B-C). In addition, two groups of neurons within the male tail region—presumably a pair of PVN neurons in ROI1 and a single EF neuron in ROI2 (Figure 3 A-B and S7)—had a strong positive correlation with PHD activity in ATR+ and not in ATR- males (Figures 3D and S8). In the male head region, we observed a more negative correlation with light stimulation. About 4 neurons in the head region are positively correlated with AWA neuron activity and about 10 neurons are negatively correlated (Figure 3D and S9).

We observed a strong negative correlation between the activity of the reversal command neurons (AVAs) and SRD-1-positive neurons in the head region (AWAs and ASIs). Although this inverse relationship was also present in the ATR untreated control group, it was less pronounced. In ATR untreated worms, the decrease in AVA activity may have been influenced by factors such as movement of the microscope objective or nonspecific light responses.

**AWA and PHD have distinct response properties**

AWA neurons have been suggested to adjust their response based on fold-changes in odor concentration, reducing turning behavior with minimal increases in odor concentration [38]. We used prolonged, behaviorally relevant high concentration sex pheromone stimulation with a thin layer micro-diffusion (TLMD) unit, facilitating pan-neuronal calcium imaging (Figure S10A) [5]. As shown in figure 3E, upon pheromone application, AWA and ASI neurons showed immediate calcium influx followed by rapid desensitization to a low, steady state within 1.5 mins, maintaining this level for at least 5 mins. This pattern indicates a robust desensitization to even a relatively high pheromone concentration. In contrast, PHD neurons exhibited sustained activation for at least 9.5 mins with a gradual decline, indicative of their threshold-sensing properties. (Figure 3F). Calcium imaging across individuals revealed that 62.5% of males exhibited a rapid response to pheromone exposure and sustained high levels of activity, whereas the remainder displayed a slow response, with delayed activation (2.5 mins post-stimulus) with a 40% reduced calcium signal amplitude (Figure 3E). The fast and slow responses of PHD neurons are particularly intriguing. This pattern appears to arise because PHDs are actively inhibited by other neurons. According to the connectome, PHDs are post-synaptic to several neurons [79], which may modulate their activity and contribute to the observed variability in response dynamics.

During the initial phase of neuronal activity, before the activation of PHD neurons, pheromone-stimulated calcium imaging revealed a negative correlation between reversal command neurons (AVAs and AVEs) and head sensory neuron activities (AWA and ASI) (Figure 3E). This negative correlation suggests that the inhibition of reversal command neurons by head neurons is pivotal for forward movement during gradient ascent. As demonstrated by the set of optogenetic experiments (see Figure 3), gradient-sensing neurons in the head region dominate PHD input and primarily drive forward movement, suggesting that head neuron activity may override or mask tail neuron activity.

In the subsequent phase, AWA and ASI activity became hyperpolarized, and all PHD neurons were activated. This allowed us to examine the direct correlation between PHD neurons and reversal command neurons (AVAs and AVEs). We observed that reversal command neurons exhibited a negative correlation with head sensory neurons and a positive correlation with tail sensory neurons (PHD), suggesting PHD-mediated activation of reversal command neurons, consistent with the observed reversal behavior during gradient descent (Figure 3E).

**PHD and AWA neurons have distinct concentration thresholds**

To confirm the correlation between reversal command neurons and anterior and posterior SRD-1-positive neurons in different sex pheromone concentrations, and to determine the concentration threshold for behavior changes, we fabricated a head and tail multi-inlet microfluidic chip (Figure 4A). We utilized immobilized worms within microfluidic chips to precisely control the delivery of varying concentration stimulations to the head or tail independently. This setup enables accurate stimulus application to distinct regions and facilitates switching between a control buffer and three different stimulus concentrations.

*C. elegans* has five pairs of premotor command interneurons, two of which promote forward locomotion and three of which promote reverse locomotion. These groups are interconnected and control distinct motor neurons [29, 35, 80, 81]. AVA neuron activity spikes at the start of a reorientation [29, 34, 35, 37, 80] and AVA interneurons integrate opposing signals from head and tail sensory neurons, guiding behavior [66, 82]. AVA's diverse activities across time scales position it as a key neuron in coordinating forward and backward movements[66, 82]. Therefore, monitoring AVA neuron activity provides a useful indicator of the animal's forward and reversal behaviors.

Using diacetyl as a baseline attractant to validate our device, we observed that all tested concentrations led to decreased AVA neuron activity, suggesting an enhancement of forward movement (Figure 4B-b). Diacetyl at higher concentrations more effectively suppresses AVA neuron activity. We then tested pheromones at varying concentrations applied to both ends and separately to the head and tail. Simultaneous stimulus of both ends immediately decreased AVA activity, indicating forward movement (Figure 4B-c). Remarkably, head-only stimulation caused a greater reduction in AVA activity compared with stimuli to both ends whereas tail-only stimulation resulted in increased AVA activity; this difference suggests antagonism of head and tail input (Figure 4B-d,e), consistent with our optogenetic and sex pheromone stimulation calcium imaging that head neurons activation promotes forward movement and tail PHD neuron activation triggers reversal (see Figure 2). These increases and decreases in AVA activity only last for one minute.

Notably, SRD-1 positive neurons in the head and tail show different preferences for sex pheromone concentrations. Higher pheromone concentrations more effectively suppress AVA activity when applied to both ends or exclusively to the head. In contrast, pheromone dilutions of 100–500X applied to the tail elicit a stronger activation of AVA neurons compared to higher or lower dilutions (Figure 4C). At dilutions of 500X, 1000X, and 2000X, AVA neurons displayed predominantly random oscillations when pheromones were applied to the head or both ends (Figure S11D). These findings suggest that higher pheromone concentrations promote forward movement more effectively, with head neurons strongly inhibiting AVA activity and weaker tail neuron activation contributing to sustained forward movement and increased speed. At moderate concentrations, the inhibition from head neurons diminishes, and tail neuron activation becomes more prominent, resulting in reduced forward movement. These dynamics are concordant with our trajectory analysis, where males exhibit a sprint behavior as they approach a high-concentration pheromone source (Figure 5B). We also noted significant spontaneous oscillations in AVA neuron signals across individuals, a finding shown in similar studies using microfluidic chips [51, 83, 84]. These fluctuations are likely due to the inherent spontaneous oscillation nature of AVA neurons, individual animals' internal status, and the restrictive environment of the microfluidic channels, which may discomfort the worms and trigger attempts to escape, causing variable AVA neuron signal patterns.

**Integration of antagonistic inputs from the head and tail**

The integration of inputs from SRD-1-positive neurons in the head and tail regions reveals a sophisticated signal-processing algorithm that optimizes navigation. Optogenetic stimulation data (Figure 2B, C, E) demonstrate that activation of tail-region neurons induces reversal behavior and slows locomotion, while stimulation of head-region neurons suppresses turning, promotes forward locomotion, and increases speed. Notably, head-region activation alone mimics the effects of activating all SRD-1-positive neurons, highlighting the dominant role of anterior SRD-1-positive neurons in guiding behavior. This aligns with findings from AWA-defective *odr-7* mutants and AWA laser-ablated males [3, 5], where AWA neurons are critical for locating pheromone sources, while ASI and PHD neurons are insufficient on their own. Conversely, the absence of tail-region PHD neurons impairs pheromone localization under natural, complex conditions, though it has minimal effects in controlled laboratory settings with high pheromone

concentrations, reduced noise, and simpler navigation challenges (Figures 1D). Together, these data suggest a dual-detector system in males, where head and tail neurons integrate sensory input, with tail neuron activation acting as a corrective mechanism during navigational errors to enhance chemotaxis efficiency.

Pheromone stimulation calcium imaging data further elucidate this integration (Figure 3G). By fitting AVA neuronal activity to a linear model incorporating AWA and PHD activity, the best-fit equation was determined to be: AVA activity = −0.7 × AWA activity + 0.1 × PHD activity − 0.2, indicating that AVA responses are primarily driven by inhibitory input from AWA neurons in the head, with a smaller excitatory contribution from PHD neurons in the tail.

Microfluidic experiments (Figure 4D) further validate this integration mechanism. The area under the curve (AUC) of AVA neuron activation during head-specific and tail-specific stimulation closely matches the trends observed with dual stimulation. This suggests that the neuronal response results from a combination of antagonistic inputs from head and tail regions, providing a robust computational framework for navigating pheromone gradients. This dual-system integration reflects a sex-specific chemoreceptor-driven behavioral adaptation for efficient navigation in complex environments.

**Orthokinetic responses to sex pheromone gradients affected by input from male tail PHD neurons**

Navigation strategies (klinokinesis, klinotaxis, and orthokinesis) are each characterized by distinct movement or orientation modalities in response to environmental cues. It is well-documented that *C. elegans* integrates biased random walks (klinokinesis) with klinotaxis, to navigate chemical gradients efficiently [52, 59-62]. Orthokinesis refers to a change in the speed of movement in response to the intensity of a stimulus, without a directional component. To elucidate the range of navigation strategies employed we evaluated changes in speed during gradient climbing.

Successful navigation depends on an organism's ability to adjust locomotion based on signal strength, integrating speed and direction for efficient environmental interaction. To assess this in *C. elegans* males, we acclimated them on agar (2 min) followed by 5 min of pre-stimulation recording. Sex pheromone introduction then triggered a 15 min post-stimulation recording, allowing us to observe potential activity modulation. Indeed, we observed a consistent adjustment in speed, and a positive correlation with gradient fluctuations across all phases of sex pheromone navigation in *C. elegans* males (Figures 5A and S12A).

We segmented the trajectories into fragments lasting 6.7 seconds (50 frames) each, plotting both the radial and total velocities. Trajectories nearing the pheromone source predominantly belonged to the group with velocities surpassing the average velocity (Figure 5C). This behavior was not observed in the control buffer M9 (Figure S12B). Also, more trajectories were observed moving towards the attractant. This approach offers an alternative way of detailing the traditional chemoattraction index, eliminating the need for arbitrary endpoint determination (Figure S12B). There is also a notable positive correlation between acceleration and movement towards additional volatile attractants, namely pyrazine, diacetyl, benzaldehyde, and IAA (Figure S13). These behavioral data suggest the pervasive occurrence of orthokinesis in *C. elegans'* navigation toward volatile odor targets.

Fragmented trajectory analysis of WT males revealed a pronounced absence of orthokinesis initiation in individuals who failed to navigate toward sex pheromones (Figure 5C, E). PHD-laser ablated and -HisCl inhibited males showed a significant decrease in orthokinesis when navigating toward diluted pheromones on larger plates (Figure 12C) and a complete lack when targeting actual females (Figure 5D). Intriguingly, as shown in Figures 5D and E, this reduction or absence in acceleration was observed across

both failed and successful free-moving target-searching attempts. There is thus a significant deficiency in the onset of orthokinesis in the absence of PHD neuron input. Collectively, PHD neurons significantly modulate orthokinetic behavior, although head neurons may also contribute. However, isolating the specific role of head neurons in orthokinesis is challenging, as animals with defective head neurons are completely impaired in pheromone chemotaxis.

The velocity distribution during successful pheromone searching was bimodal, while unsuccessful attempts and pre-stimulation phases were unimodal, indicating failed orthokinesis initiation in unsuccessful navigators (Figure 5D). This difference indicates that individuals failing in navigation also failed to initiate orthokinesis. During moving-target navigation toward conspecific females, mock control males exhibited bimodal velocity distributions in both successful and successful attempts subgroups with a larger peak in the acceleration group and a smaller peak in the deceleration group during successful attempts compared to unsuccessful ones. Notably, in unsuccessful attempts, PHD-ablated males lacked the pronounced bimodal velocity distribution observed in the control group. This finding highlights the critical role of PHD neuron input in initiating orthokinesis, which is essential for successful navigation (Figure 5G).

**A simple model for spatially separated detectors navigation in *C. elegans***

Sensory neuron inputs are typically conserved through the connectome and determine the behavioral outcomes [38]. Summarizing the experimental observations of the strong correlations between the AWA, PHD and AVA neurons (Figures 3-4), we propose a simple model to demonstrate the roles of head and tail sensory inputs. We focused on the macroscopic navigation behavior and neglected details of microscopic traits and changes in worm body curvature in motion.

During kinesis searching, the locomotion of a worm is modeled as a mixture of active Brownian motion [85] and run-and-tumble motion [86] (see Methods). Our first key assumption is that sensory inputs from the head and tail are converted into confidence variables $Q^H$ and $Q^T$, which then determine the worm's dynamical state (Figure 6A). As the activity of reversal command neurons AVA and AVE is found to correlate negatively with AWA activation but positively with PHD neuron activation, we propose a simple form to qualitatively capture these correlations:

$$\gamma = \gamma_0 e^{-\lambda_K (Q^H - Q^T)}, U = U_0 + U_1 (Q^H - Q^T + \eta).$$

Here $\gamma_0 = 0.067/s$ is the baseline tumbling rate. $U_0 = 0.064$ mm/s is the baseline average speed, and $U_1 = 0.03$ mm/s is the magnitude of speed fluctuation. $\lambda_K$ represents the strength of klinokinesis, and $\eta$ represents a Gaussian noise in the velocity. The worm's dynamical state is characterized by its velocity and tumble rate $(U, \gamma)$.

Our model is based on the idea that sensory information coming from the worm's head and tail is translated into a signal that is a measure of 'confidence' ($Q$). These signals directly determine the worm's behavior and movements (Figure 6A). AWA neurons become more active as sex pheromone concentration increases [5]. In our microfluidic experiment, we found that input from head neurons suppressed AVA neuron activity (Figure 4D). Therefore, in our model the confidence signal based on head input ($Q^H$) will rise with increasing pheromone concentration until it reaches saturation (see blue line in Figure 6A). Interestingly, high pheromone concentrations at the tail suppress AVA neuron activity, in contrast to the activation observed at low concentrations (Figure 4B). Furthermore, continuous activation of the PHD neuron will result in a reduction in baseline velocity, along with the sprint behavior exhibited upon proximity to the target, suggesting that $Q^T$ should decrease below zero to capture these observations (see red line in Figure 6A). We propose using the $Q^H - Q^T$ model (see purple line in Figure 6A) to represent the negative correlation between AVA/AVE command neurons and AWA activation, and

the positive correlation with PHD neuron activation. Importantly, only $Q^H - Q^T$ accurately captures the observed increase in speed towards the end of navigation, which wouldn't be captured by simply adding the two signals together (compare purple and green lines in Figure 6A).

To determine the dynamics of $Q^H$ and $Q^T$ given external concentration field evolution, we adopt the simplest dynamics model with a single memory timescale:

$$\frac{dQ^H}{dt} = -k_1 Q^H + k_2^H f_H\left(C, \frac{dC}{dt}\right),$$

$$\frac{dQ^T}{dt} = -k_1 Q^T + k_2^T f_T(C).$$

Here $\frac{1}{k_1}$ is the timescale of memory, while the values of $k_2^{H,T}$ represent the sensitivity of SRD-1 positive neurons. $f_H$ and $f_T$ represent the sensory inputs, and they are chosen to qualitatively reflect the observations in this work and AWA calcium dynamics in [38] (see Methods). Key assumptions are: (1) the long decay time of PHD activity level during constant sex pheromone stimulation, as seen in Figure 3F, indicates that PHD sensory input mainly depends on the absolute concentration, hence $f_T$ is only a function of $C$. (2) PHD response is positive at intermediate concentration ranges but becomes strongly suppressed at high concentration, as shown in Figure 6A. (3) The relatively short decay time of AWA activity level during constant stimulation, as shown in Figure 2 of ref [38], indicates that AWA sensory response mainly reflects the detected concentration change, with a mild increase as absolute concentration increases.

For simplicity, in this model worms will make directional (taxis) turns when they (1) detect a high enough concentration above a threshold value, and (2) if they currently experience a concentration decrease. Such turns are assumed perfectly accurate toward the source direction. Based on our experimental observations, head-inhibited worms will not perform taxis turns.

We performed simulations for navigation on a small Petri dish with the concentration simulation for 30 mins (Figure 6B). Each simulation contains 10000 worms, initialized with random orientations. When both head and tail sensory inputs are missing, $Q^H = Q^T = 0$, the worms perform a standard active random walk with constant mean velocity and tumble rate (Figure 6C-F). Only a small fraction – about 10% of worms – were able to find the pheromone source by luck, as seen in the grey curve of Figure 6F and SI video S2. Their velocity distribution is simply determined by the Gaussian noise $\eta$ (Figure 6D right row). As expected, the successful trajectories showed more segments going toward the source and the failed ones showed more away from the source (Figure 6E right row). However, at no time is there a correlation between the velocity and direction.

Adding tail sensory input alone significantly enhanced the chance of finding the pheromone source, almost doubling the probability (Figure 6F blue curve). Qualitatively, PHD input alone results in a bimodal shape of velocity distributions for the successful worms yet a monomodal shape for the failed ones (Figure 6D), consistent with the experimental observations (Figure 5F). Statistics of the radial vs. total velocity (Figure 6E) also display the same trend as in the experiments (Figure 5E), where successful trajectories show clear positive correlations between acceleration and moving toward the source. Adding head sensory input boosts the overall success rate to nearly 100%, simply due to the dominating effect of taxis turns (SI video S1). However, the qualitative statistics of velocity distributions and correlations with movement directions remain unchanged. Overall, with tail input, the trajectories are biased closer to the pheromone source, as shown in Figure 6G. We compute the maximum distance away from the pheromone source that reach worm reaches during the search, denoted as $d_{max}$. For successful worms with head inputs, the addition of tail inputs accelerates their search so that their $d_{max}$

is slightly smaller compared with those without tails. In the absence of either head or tail inputs, worms only perform random walks and are stay near the starting position; adding tail inputs effectively incentivizes them to explore larger areas and more biased to the source, manifested in significantly larger $d_{max}$ values. These simulations suggest that (1) tail input significantly improves the success rate of mate-searching when the effect of taxis turns is not overly dominating. (2) Tail input alone determines the qualitative statistics of velocity distributions and correlations with movement directions, while head input only quantitatively modifies these distributions.

## Discussion

### Enhancing mating success with airborne and water-soluble pheromones in open environments

Nematodes, thriving in nutrient-rich, microorganism-abundant habitats like garden soil, exhibit varying outcross rates—from 0.1% in lab conditions for the N2 strain to up to 22% in natural settings [87, 88]. How do sex-related cues work together to make a successful mating happen, especially where visual cues are negligible or absent? Previous studies have noted that water-soluble pheromones, ascarosides, released by hermaphrodites can attract males from a certain range [21]; however, in open environments, animals cannot rely exclusively on water-soluble pheromones for mate attraction because they diffuse too slowly over large areas.

In contrast to ascarosides, which signal multiple aspects of nematode development and physiology [11-14, 89, 90], volatile sex pheromones are reported solely as signals of fertility status, sexual maturity, and mating readiness. This pheromone can attract mates from a distance and trigger copulation-related behavior. Its production depends on the female somatic gonad, which ceases post-mating but resumes several hours after mating ends [3, 4]. Furthermore, both *C. remanei* and *C. brenneri* females, along with *C. elegans* hermaphrodites that are virgin, self-sperm-depleted or -defective, can emit these pheromones once sexually mature [3-5]. Thus, the volatile sex pheromone in nematodes may function as a universal mate attractant across *Caenorhabditis* species, with minimal variation between them. Consequently, it does not trigger species-specific responses in *Caenorhabditis* males. There are successful mating behaviors between different *Caenorhabditis* species, as evidenced by the males leaving mating plugs on the females [91, 92] indicating that males in *Caenorhabditis* species might not possess a mechanism for distinguishing females from closely related species.

### A navigation strategy based on an integrative dual-detector mechanism

The dual detectors are a more elaborate form of directional movement, with multiple sensory organs allowing simultaneous comparison of stimulus rather than a single organ comparing in time. In *C. elegans*, the phasmid neurons in the tail, similar to the amphid chemosensory organs in the head, perform a chemosensory function [63]. Indeed, amphid and phasmid neurons influence the worm's backward movements when exposed to repellents, integrating sensory inputs from both the head and tail to promote effective escape behaviors [63-65]. Subsequent research demonstrates that the AVA interneuron consolidates signals from the head and tail sensory neurons to steer behavioral choices [64]. Our study provides the first evidence of dual detectors in attractant navigation. Repellents demand rapid avoidance (reversal), while attractant sensing requires complex, targeted navigation strategies.

Head- and tail- located neurons utilize the same receptor but drive distinct and opposing sensorimotor responses: AWA promotes forward movement and speeding up while PHD induces reverse movement and slowing down. Behavioral output is typically dominated by AWA activation, while PHD input provides antagonistic modulation of AWA-driven behavior. The head neuron exhibits gradient-sensing properties and rapid desensitization in constant concentrations, while the tail neuron displays threshold-sensing

properties and remains activated under constant concentrations. This demonstrates a fundamental aspect of neural circuitry: different neurons are co-opted to handle distinct environmental stimuli. Additionally, PHD neurons are activated at low pheromone concentration, thus preventing males from false taxis turns induced by rapid temporal evolution of volatile pheromone concentration. PHD neurons are inactive at high pheromone concentration, promoting rapid acceleration (sprints) as the male approaches the pheromone source. We computationally model the response, proposing that males have a measure of confidence that they are proceeding in the right direction; absence of PHD input disrupts directional confidence, preventing the acceleration response.

Contrary to prior hypotheses [93-96], *C. elegans* do not rely solely on simple head-tail concentration comparisons but instead employ a complex antagonistic mechanism involving head and tail sensory neurons, each with distinct preferred concentrations for optimal activation. Our proposed mechanism focuses not on the spatial separation of receptors but on comparing signals from two distinct sensory neuron types, AWA and PHD, with different response properties. This comparison enables the animal to integrate various aspects of pheromone gradient dynamics and make adaptive behavioral decisions. While the mechanism relies on comparing outputs from these neurons, their differences stem from their response characteristics rather than their physical locations. This strategy would be particularly beneficial for navigating a volatile gradient, such as a shallow and low-concentration pheromone gradient, where there is minimal difference in concentration between the worm's head and tail, making head-tail absolute concentration comparisons unreliable.

Besides our work, other studies have shown that numerous chemosensory GPCRs are also co-expressed in the head amphid and tail phasmid neuron classes [63, 97-100], which raises the possibility that tropotaxis is a general mechanism in *C. elegans* and exists beyond responding to volatile sex pheromones.

**Klinokinesis, Klinotaxis and Orthokinesis**

Organisms have diverse ways of navigating the natural world. Klinokinesis and klinotaxis represent non-directional and directional navigation behaviors, respectively (Figure S12B). The major difference between kinesis and taxis lies in whether the new heading exhibits a directional bias. Klinokinesis involves turning rate modifications based on stimulus intensity, facilitating random exploration and environmental adjustment without a direct orientation towards or away from stimulus. Conversely, the animal continuously corrected its direction during klinotaxis to follow the steepest gradient. Studies on *C. elegans* have significantly advanced our understanding of chemotaxis. *C. elegans* employs all four primary behavioral strategies shared in the animal kingdom for resource localization [52-58]. Pierce-Shimomura et al. and Iino and Yoshida revealed the role of pirouettes in chemotaxis [59, 60], also showing that *C. elegans* employs both biased random walks and taxis to navigate NaCl gradients. These nematodes optimize their path towards more favorable environments by extending runs towards higher concentrations and shortening them when moving away.

Orthokinesis, which differs from other navigation behaviors, involves speed modulation in response to stimulus intensity. It emphasizes the adaptability of organisms to environmental cues through activity level adjustments. This behavior, along with directional navigation, illustrates the complex nature of behavioral responses, integrating both orientation and speed modulation for environmental navigation. Prior research noted that orthotaxis has a diminished effect on locomotion in shallow, water-soluble stimulus gradients during chemotaxis [52]. In our study, orthokinesis was observed throughout the entire pheromone navigation process. Moreover, we tested several other volatile attractants, all exhibiting orthokinesis during the entire target-searching process (Figure S11). This may be due to differences in the chemical properties of the substances used in previous studies, which focused on water-soluble chemicals,

whereas our study concentrated on volatile components, resulting in distinct concentration fields. Animals engage in orthokinesis instead of maintaining a uniform speed during navigation as a strategy to balance the economical use of energy with the urgency of locating a source before it is depleted by competitors or potential mating partners who have departed or mated with others. As we demonstrated, *C. elegans* increase their speed when confident about their direction and slow down to conduct more restricted area searching when uncertain. This adaptive behavior enables them to efficiently reach targets while minimizing energy expenditure during the search.

**Sexual dimorphic decision-making in *C. elegans* stems from sensory neuron inputs**

The distinct responses of males and females to the same sex pheromone prompt questions about the neural foundations of behavioral sexual dimorphism [3-5]. Our findings indicate that sexual dimorphism in naïve *C. elegans* males' response to sex pheromone stimulation stems from variations in receptor expression. This leads to differential sensory neuron activity propagating through neural circuits, culminating in distinct behaviors. Although existing data from other organisms suggest that sex-specific pheromone responses arise from sexually dimorphic neural circuits, not differential sensory perception [101-103], incomplete characterizations of neural networks in complex model organisms may bias our interpretation of this phenomenon. *C. elegans* demonstrates an olfactory system where sophisticated modulation of a single receptor's expression allows both efficient tropotaxis and the execution of distinct sex-specific behaviors. Therefore, modeling the activity of the key sex pheromone sensory neurons, AWAs and PHDs, allows for the prediction of behavioral outcomes in naïve *C. elegans*.

**Decision in uncertainty: how worms navigate complex gradients with imperfect sensory input and inaccurate steering angle control**

As a complementary approach to experimental tests of our hypothesis, we used computational modeling to examine its plausibility. We developed a simple mathematical model that allowed us to deduce optimal navigation strategies. From our examination of optimal navigation strategies, we propose a scenario involving an idealized worm with precise short-term memory of its trajectory and the ability to detect concentration gradients in its path precisely. This setup presumes that the worm's sensory systems are infallible, enabling it to sample two distinct directions during its search. Such accurate sampling is theoretically sufficient to identify the gradient's direction, assuming the worm's neural circuitry can process this information. In practice, however, a worm's memory and sensory perception are inaccurate due to inherent noise, complicating the task of gradient estimation. This challenge mirrors a regression problem where the objective is to select an optimal turning angle for a second sample that minimizes the uncertainty in determining the gradient's direction.

Our analysis, grounded in a least-squared-error regression framework, suggests that the optimal choice for a second sampling direction consistently exceeds 90 degrees regardless of the initial sampling orientation relative to the actual gradient direction. With an initial orientation distributed uniformly randomly, the preferable turning angle is approximately 120 degrees (Figure S15). This direction is chosen to be away from the gradient if the initial angle is qualitatively aligned (less than 90 degrees from the gradient) and towards the gradient otherwise. Given the worm's lack of precise knowledge of gradient direction, it faces a choice: turn 120 degrees in either direction or, as a compromise, nearly 180 degrees (Figure S15). Observations suggest that worms likely opt for turns close to 180 degrees in early search stages, indicating a strategic approach to maximize information gain about the gradient's direction. This investigation highlights the intricate balance by which worms maintain between their behavioral strategies and their sensation, motor control, and cognitive limitations.

**Implications of our computational modeling**

We observe from the finite element method (FEM) simulations that the concentration field deviates from Gaussian distributions, which are often assumed. The main reason for this deviation may be that the sex pheromone studied here is air-borne, while previous studies involve water-soluble chemicals like salt. Air-borne pheromone diffuses rapidly, and the diffusion timescale in air is short compared to the diffusion into the agar, due to the 1000-fold density difference between the two media. The resulting diffusion process is nonlinear: the region of agar right below the pheromone droplet initially absorbs pheromone and reaches high concentration, but later emits pheromone back into the air. We emphasize that the non-Gaussian distribution is general for chemicals that transport in both air and agar phases and should be considered for modeling chemotaxis for such species.

From the mate-searching simulations, beyond a certain distance from the source, the concentration is relatively low but always increases due to the finite size of the plate. Worms in this outer region can experience positive $\dot{C} > 0$ even if they are moving away from the source, which would lead to a fake continuous increase of head confidence $Q^H$. Without tail input antagonistic to the head input, worms are misled to lower tumble rate and higher speed and spread out to even further regions as a result (SI video S1 and S2). The tail input suppresses such erroneous behaviors and maintains a higher tumble rate to correct its direction more efficiently.

We also tested with $Q^T \to 0$ at a high concentration level. However, the worm's performance is much better for $Q^T \to -1$ at high concentration level, indicating that a possible suppress of PHD activity at high concentration, either by its own sensory mechanism or synergistically by the high activity of AWA, could be critical to improve the searching efficiency. In fact, the GCaMP signal of PHD at 1x concentration stimulation (Figure 8) shows a negative value compared to the baseline. Hence, we have adopted the functional form for PHD response to behave as $\lim_{C\to 0} Q^T \to 0$ , $\lim_{C\to C_0} Q^T \to 1$ , and $\lim_{C\to \infty} Q^T \to -1$.

## Methods

### Key Resource Table

| REAGENT or RESOURCE | SOURCE | IDENTIFIER |
|---|---|---|
| **Bacterial and virus strains** | | |
| *E. coli* | Caenorhabditis Genetics Center (CGC) | WormBase: OP50; WormBase: WBStrain00041969 |
| **Experimental models: Organisms/strains** | | |
| *him-5 (e1490) V* | CGC | CB4088 (male enriched mutant) |
| *srd-1(eh1)* | CGC | CB5414 (*srd-1* mutant) |
| *syEx1972 [srd-1P::mCherry]; syEx1974 [unc-119::gfp]* | This study | PS10451 (*srd-1* reporter; pan-neural marker) |
| *syEx1973 [rab-3P::mCherry]; syIs912[srd-1P::Gal4(sk)::VP64]; syIs300 [15xUAS::GFP]* | This study | PS10448 (*srd-1* driver; GFP effector; pan-neural marker) |
| *syEx1972 [srd-1P::mCherry]; syIs913 [pkd-2P::Gal4(sk)::VP64]; syIs300 [15xUAS::GFP]* | This study | PS10449 (*srd-1* reporter; *pkd-2* driver; GFP effector) |

| | | |
|---|---|---|
| *syIs912[srd-1P::Gal4(sk)::VP64]* | This study | PS9477 (*srd-1* driver) |
| *syIs914[srd-1P::Gal4(sk)::VP64]* | This study | PS9478 (*srd-1* driver) |
| *syIs912[srd-1P::Gal4(sk)::VP64]; syIs300[UAS::GFP]* | This study | PS9473 (*srd-1* driver; GFP effector) |
| *syIs913[pkd-2P::Gal4(sk)::VP64]; syIs300 [15xUAS::GFP]* | This study | PS9681 (*pkd-2* driver; GFP effector) |
| *syIs838[lin-48dP::NLS::cGAL (DBD)::gp41-1::N-intein::let-858 3'UTR, srd-1P::NLS::gp41-1::C-intein::cGAL(AD)::let-858 3'UTR]* | This study | PS10007 (PHD driver) |
| *syIs838[lin-48dP::NLS::cGAL (DBD)::gp41-1::N-intein::let-858 3'UTR, srd-1P::NLS::gp41-1::C-intein::cGAL(AD)::let-858 3'UTR]; syIs300[15xUAS::GFP]* | This study | PS9573 (PHD driver; GFP effector) |
| *syIs888 [gpa-14P::NLS::cGAL (DBD)::gp41-1::N-intein::let-858 3'UTR, rig-3P::NLS::gp41-1::C-intein::cGAL(AD)::let-858 3'UTR]* | This study | PS10179 (AVA driver) |
| *syIs888[gpa-14P::NLS::cGAL (DBD)::gp41-1::N-intein::let-858 3'UTR, rig-3P::NLS::gp41-1::C-intein::cGAL(AD)::let-858 3'UTR] ]; syIs300[15xUAS::GFP]* | This study | PS10087 (AVA driver; GFP effector) |
| *syIs564 [odr-10P::Gal4(sk)::VP64]; syIs300 [15xUAS::GFP]* | This study | PS8293 (AWA driver; GFP effector) |
| *syIs340 [15xUAS::hChR (H134R)::EYFP::let-858 3'UTR]; him-5 (e1490) V* | This study | PS9782 (Chrimson effector; *him-5*) |
| *syIs340 [15xUAS::hChR (H134R)::EYFP::let-858 3'UTR]; him-5 (e1490) V* | This study | PS7043 (Chrimson effector) |
| *syIs371[15xUAS::HisCL::SL2::GFP::let-858 3'UTR]* | This study | PS7199 (HisCL effector) |
| *syIs612[15xUAS::GCaMP7b::SL2::mKate2]* | This study | PS9046 (GCaMP7b effector) |
| *syIs912[srd-1P::Gal4(sk)::VP64]; syIs612[15xUAS::GCaMP7b::SL2::mKate2]* | This study | PS9680 (*srd-1* driver; GCaMP7b effector) |
| *syIs912[srd-1P::Gal4(sk)::VP64]; syIs371[15xUAS::HisCL::SL2::GFP::let-858 3'UTR]* | This study | PS10005 (*srd-1* driver; HisCl effector) |
| *syIs912[srd-1P::Gal4(sk)::VP64]; syIs340 [15xUAS::hChR (H134R)::EYFP::let-858 3'UTR]; him-5 (e1490) V* | This study | PS9990 (*srd-1* driver; Chrimson effector) |
| *syIs838[lin-48dP::NLS::cGAL(DBD)::gp41-1::N-intein::let-858 3'UTR, srd-1P::NLS::gp41-1::C-intein::cGAL(AD)::let-858 3'UTR]; syIs371[15xUAS::HisCL::SL2::GFP::let-858 3'UTR]* | This study | PS10189 (PHD driver; HisCL effector) |
| *syIs838[lin-48dP::NLS::cGAL(DBD)::gp41-1::N-intein::let-858 3'UTR, srd-1P::NLS::gp41-1::C-intein::cGAL(AD)::let-858 3'UTR]; syIs340 [15xUAS::hChR(H134R)::EYFP::let-858 3'UTR]; him-5(e1490)V.* | This study | PS10187 (PHD driver; Chrimson effector) |
| *syIs888 [gpa-14P::NLS::cGAL (DBD)::gp41-1::N-intein::let-858 3'UTR, rig-3P::NLS::gp41-1::C-intein::cGAL(AD)::let-858 3'UTR]; syIs612[15xUAS::GCaMP7b::SL2::mKate2]* | This study | PS10181 (AVA driver; GCaMP7b effector) |
| *syIs564 [odr-10P::Gal4(sk)::VP64]; syIs340 [15xUAS::hChR (H134R)::EYFP::let-858 3'UTR]* | This study | PS9387 (AWA driver; Chrimson effector) |
| *hpIs675 [rgef-1P::GCaMP6s::3xNLS::mNeptune + lin-15(+)]; lin-15(n765) X; him-5 (e1490) V* | This study | ZM9627 (pan-neuronal nucleus localized |

| | | |
|---|---|---|
| | | mNeptune and GCaMP6s) |
| *hpIs675 [rgef-1P::GCaMP6s::3xNLS::mNeptune + lin-15(+)]; lin-15(n765) X; him-5 (e1490) V; srd-1(eh1)* | This study | PS10450 (pan-neuronal nucleus localized mNeptune and GCaMP6s in *srd-1(eh1)* background) |
| *lite-1(ce314); JAC66[ ift-20P:BFP; eat-4P::cyOFP1; unc-17P::mScarlet: acr-5P::BFP; hpIs675 [rgef-1P::GCaMP6s::3xNLS::mNeptune + lin-15(+)]; lin-15(n765) X* | This study | ADS1046 (pan-neuronal nucleus localized mNeptune, GCaMP6s, and neuron ID markers) |
| *lite-1(ce314); JAC66[ ift-20P:BFP; eat-4P::cyOFP1; unc-17P::mScarlet: acr-5P::BFP; hpIs675 [rgef-1P::GCaMP6s::3xNLS::mNeptune + lin-15(+)]; lin-15(n765) X; syIs912[srd-1P::Gal4(sk)::VP64]; syIs340 [15xUAS::hChR(H134R)::EYFP::let-858 3'UTR]; him-5(e1490).* | This study | PS10153 (pan-neuronal nucleus localized mNeptune, GCaMP6s, neuron ID markers; *srd-1* driver; Chrimson effector) |
| *Kp1368 [myo-2P::NLS::mCherry]; syIs371[15xUAS::HisCL::SL2::GFP::let-858 3'UTR]* | This study | PS8720 (muscle driver; HisCl effector) |
| *syIs334 [rabP::GAL4::gp41::N::let-858 3' UTR]; syIs340 [15xUAS::hChR(H134R)::EYFP::let-858 3'UTR]; him-5(e1490).* | This study | PS8026 (pan-neural driver; Chrimson effector) |
| **Software and algorithms** | | |
| Fiji | Schindelin et al., 2012 [104] | https://imagej.net/software/fiji/ |
| MaMuT 0.27 | Wolff et al., 2018 [105] | https://imagej.net/plugins/mamut/ |
| Target track | Park et al., 2018 [106] | https://www.nature.com/articles/s41592-023-02096-3 |
| Ilastik software | Berg et al., 2019 [107] | https://www.ilastik.org |
| **Other** | | |
| cGAL-UAS bipartite expression toolkit | Nava et al., 2023 [108] | https://www.pnas.org/doi/full/10.1073/pnas.2221680120 |

684

685 **Worm Strains**

686 Strains of *C. elegans* used in this study originated from the N2 (Bristol) wild-type lineage and were
687 maintained under standard laboratory conditions using Nematode Growth Medium (NGM) plates with *E.*
688 *coli* OP50 as the food source. Detailed information regarding the strains is provided in Key Resource
689 Stable.

690 **Imaging of Expression Patterns**

691 Animals were immobilized on a 4% ultrapure agarose pad using 3-5µL of 2-5mM levamisole. The imaging
692 was conducted using an inverted laser scanning confocal microscope, Zeiss LSM 980, integrated with a
693 Zeiss Axio Observer 7 with Definite Focus 2. Subsequent image processing was executed via FiJi (ImageJ)
694 software.

695 **Inhibition of PHD Neurons by the HisCl method and Modified Chemoattraction Assay**
696 Inhibition of PHD neurons was achieved through the histamine-gated chloride channel method, as
697 outlined in the study [109], with slight alterations. Nematode Growth Medium containing histamine
698 (NGM-HA) was prepared by incorporating histamine dihydrochloride from Sigma Aldrich (1 M stock
699 solution) into NGM agar at approximately 65 °C just prior to plate pouring. Control plates without
700 histamine were prepared simultaneously from the same batch of NGM. Plates supplemented with 10
701 mM histamine remained effective for a minimum of two weeks when refrigerated at 4 °C, verified by
702 preliminary testing with a control strain possessing the *myo-2* promoter-driven HisCl effector in the
703 cGAL-UAS system. L4-stage males were selected and isolated a day in advance of the assays. Histamine
704 treatments were conducted without the presence of food to eliminate confounding factors. Histamine-
705 induced inhibition occurred within ten mins of exposure. Once removed from histamine, the animals
706 typically require one to two hours to fully recover.

707 The chemoattraction assay plates were prepared using 1.5% agar, 25 mM NaCl, 1.5 mM Tris-base, and
708 3.5 mM Tris-Cl, and conducted according to the protocol described in the literature [5], but included
709 modifications to accommodate different plate dimensions, adjustments in the spatial distance between
710 the stimulus source and the starting point of the animals, and alterations in the sex pheromone
711 concentration, as depicted in the associated figures (see Figure 1 and S1).

712 Stimulus droplets are placed on the lid of the plate, and the location of the worms is recorded every 5
713 mins up to 30 mins post-stimulation to assess their response to the introduced stimulus. In our research,
714 we utilized two sizes of plates for the assays, with effective worm-moving surfaces measuring 5.5cm and
715 8.4cm in diameter. For simplicity and clarity in labeling, these were referred to as 6-cm and 8-cm plates,
716 respectively. In our study, we employed two types of 2D chemoattraction assays distinguished by the
717 setup and calculation of the Chemoattraction Index (C.I.). For Type 1 assays, constrained by the smaller
718 plate size, a control buffer spot was not included. Here, the C.I. was derived from the ratio of worms that
719 reached the test spot to the total number of worms introduced. Conversely, in Type 2 assays, the C.I. was
720 determined by subtracting the number of worms that reached the control spot from those that arrived
721 at the test spot, divided by the total number of worms. In each chemoattraction assay, we placed 20
722 worms at a designated starting point. To ensure the reliability and robustness of our data, we repeated
723 each assay 20 times across three distinct days.

724 **3D Chemoattraction Assay**
725 Worms prepared via the "Inhibition of PHD Neurons by HisCl Method" are used for a 3D chemoattraction
726 assay employing 0.3g of gellan gum in 100ml chemoattraction assay buffer to create a navigable gel
727 environment. This composition ensures that worms can navigate through the gel freely, without
728 becoming immobilized by water or causing structural damage to the gel through movement. The gellan
729 gum solution is adjusted to match the salt concentration of the chemoattraction assay plates utilized in
730 this research.

731 For plate preparation, 22ml of the gellan gum solution is poured into a 6-cm plate immediately after the
732 gellan gum is dissolved by heating in a microwave. The solution is allowed to cool to room temperature

733 before introducing the worms. To embed the worms within the gel, 0.5ml of the gellan gum gel is
734 removed from the center of the plate by pipetting. Then 20 worms are picked by worm picker and
735 placed. This cavity is then refilled with 0.7ml of gellan gum gel, ensuring the worms are fully embedded
736 within the gel. Unlike traditional chemoattraction assays, the stimulus is applied directly onto the surface
737 of the gel rather than on the lid of the plate (see Figure 1D-b,g). In this endpoint assay, trajectories are
738 not recorded; instead, the number of worms reaching the target spot is documented every 5 mins for up
739 to 30 mins post-stimulation to evaluate their responses to the introduced stimulus. To ensure the
740 reliability and robustness of our data, we repeated each assay 20 times across three distinct days.

741 **PHD laser ablation and Single-worm female searching assay.**
742 To explore the function of PHD neurons in male *C. elegans*' attraction to volatile pheromones, laser
743 ablation experiments were conducted on young adult males of the PS9477 strain. The procedure
744 involved mounting the worms on a glass slide with a 10% agar pad derived from NGM buffer and using a
745 coverslip to immobilize them with 0.2 µm latex beads (Polysciences, Inc.). Ablation of PHD neuron nuclei
746 on both sides was achieved using the MicroPoint (Andor) pulsed laser system, coupled with a 100x 0.95
747 NA Nikon Plan Apo objective. Post-ablation, males were transferred to NGM plates seeded with OP50
748 and allowed to recover overnight. Mock ablations served as controls. Behavioral assays were conducted
749 on 6-cm NGM plates seeded with OP50, using virgin adult *C. remanei* (*unc*) and *C. elegans (fog-2*)
750 females. We placed a single male and female worm 2cm apart on these plates and recorded their
751 interaction at 5Hz for 30 mins or until they made contact. For *fog-2*, both male and female trajectories
752 were traced with MAMUT software and de-noised using a Savitsky-Golay filter.

753 We measured the time taken by the male to reach the female, calculating the Mate Attraction Index
754 (MAI) as follows: MAI = normalized velocity * cos(Θ), where Θ is the angle indicating the direction of the
755 male's movement relative to the female. This index quantifies the male's navigational efficiency towards
756 the female, with 1 indicating direct movement towards the female at maximum speed, and -1 indicating
757 movement away at maximum speed. This method offers a refined analysis of male chemotaxis in
758 response to female pheromones post-PHD neuron ablation.

759 **Optogenetics Perturbation Velocity Analysis**
760 The optogenetics perturbation assay was conducted using Chrimson, a red-shifted channelrhodopsin,
761 following protocols outlined by the literature [78, 110, 111], with slight modifications. All-trans-retinal
762 (Sigma-Aldrich) was incorporated at a concentration of 500 µM into 6-cm diameter plates containing
763 20mL of chemoattraction assay solution. One-day-old adult animals were placed on these plates and
764 subjected to a red LED stimulus using a WormLab Tracking system (MBF Biosciences). Prior to
765 stimulation, allow 5 worms a 5-minute acclimation period on the assay plate. The LED stimulus was
766 administered in a pattern of 5 seconds baseline record before stimulation, and 10-60 seconds on,
767 followed by 7.5-30 seconds off, at 100% intensity across 6-8 cycles. Implement a 30-second inter-
768 stimulus interval for PHD activation. This provides sufficient time for the worm to return to a stable
769 forward movement state. Worm tracking was conducted using the same WormLab system.

770 **Dissecting Micro-behaviors Under Optogenetic Perturbation**
771 Experiments used 8-cm NGM agar plates seeded with a thin OP50 layer to prevent starvation-induced
772 behaviors. Males were transferred from ATR+ and ATR-culture plates to an assay plate. The plate was
773 mounted on a motorized stage controlled by a joystick. Individual males were tracked and recorded with
774 a 10x 0.3NA Nikon Plan Fluor objective at 10Hz. Illumination was provided by dim, red-filtered light using

775 a HOYA 52mm R(25A) filter to minimize disturbance to the worms. For the stimulation, we used a Sola
776 Light Engine (lumencor) light source and a 607/36 nm BrightLine excitation filter. The microscope's field
777 diaphragm was adjusted such that only a small area was illuminated when the excitation light was on.
778 We used the SOLA-SE2 software to control the light source. Prior to stimulation, allow a single worm a 5-
779 minute acclimation period on the assay plate. The male was tracked manually using the motorized stage
780 and the following stimulation regime was applied: 30 seconds without light, followed by twenty 2-
781 second tail pulses (2-second intervals), another 30-second dark period, then 30 seconds of head
782 stimulation, and a final 30-second interval without light.

783 After postprocessing, we divided the recording into 2-second segments. For each 2-second segment, we
784 tabulated the behavioral motif displayed by the male or the first behavioral transition that occurred
785 during that segment. The following behavioral motifs and transitions were included: forward, backward,
786 transition from forward to backward, transition from backward to forward movement, hesitation
787 (marked by frequent direction changes within the 2-second window), and self-exploration (where the
788 worm attempts to probe its own body). This analysis provides a detailed account of the nuanced
789 responses of male *C. elegans* to optogenetic perturbation, offering insights into the micro-behavioral
790 dynamics elicited by targeted neural stimulation.

791 **Pan-neuronal calcium imaging with optogenetic activation**
792 This experiment used the same sparse labeling makers, pan-neuronal calcium imaging strain mentioned
793 previously. For the experiments, males were prepared on 10% agar NGM buffer slides. Using a spinning
794 disc confocal setup, we navigated the challenge of simultaneous neuronal imaging and optogenetic
795 stimulation of Chrimson, which responds to both 488 nm and 578 nm light, by implementing a strategy
796 to exploit the GCaMP signal delay post-stimulation, as outlined in Lu et al. (2022) [112]. This involved
797 interlacing five 10-second imaging/stimulation intervals with 50-second breaks, applying 12% and 35%
798 intensities for the 488 nm and 561 nm lasers, respectively, while acknowledging potential mechanical
799 stimulation from objective movement as a confounding variable. During each 5-second
800 imaging/activation period the piezo-controlled objective was moving, whereas it was not moving
801 between these periods. We therefore cannot rule out mechanical stimulation that coincided with the
802 light stimulation as a confounding factor. To aid neuron identification, after the recording session, we
803 acquired additional volumes using the following combination of excitation lasers and emission filters:
804 30% 640 nm 617/73 nm (200 Hz), 40% 561 nm 578 nm (200 Hz), 35% 488 nm 578 nm (200 Hz), 15% 488
805 nm (200 Hz), 95% 405 nm 440 or 450 nm (50Hz).

806 The same pre-processing and neuron activity tracking via Targettrack was performed as outlined in "Sex
807 Pheromone-Induced Pan-neuronal calcium imaging in *C. elegans*" with minor modifications. For each
808 neuron, we created 3 ground truth points, 100 volumes apart. Activities of PHD neurons in ATR+ and
809 ATR- males were extracted and averaged (Fig 3). We calculated the correlation between the mean PHD
810 activity in ATR+ males and activity traces of other neurons in both ATR+ and ATR- males. A subset of 12
811 neurons was identified across all males and we used Generalized Procrustes analysis [113] and thin plate
812 splines [114] to register all male tail neurons to a common coordinate space. These landmark neurons
813 were: PHDR, PHDL, PLMR, PCAR, PCAL, HOA, PVY, PDC, PVX, VD12, VA10, and VA11. A visual inspection
814 identified two regions that contain neurons highly correlated with PHD (correlation cutoff >0.55). Here
815 we refer to these regions as ROI1 and ROI2 (see Figure 3 and S7). AWA, ASI, AVA and AVE are identified
816 based on sparse labeling makers, positioning and cell body size. The relative intensity values ($\Delta R/R0$) are
817 plotted following the methodology outlined in "Sex Pheromone-Induced Pan-neuronal Calcium Imaging

818 in *C. elegans*" with minor modifications. We normalized the ΔR/R0 values for each neuron in the ATR+
819 and ATR- groups to a range of 0 to 1. The dashed line indicated the starting point of each light
820 stimulation.

821 **Sex Pheromone-Induced Pan-neuronal Calcium Imaging**
822 For sex pheromone extraction, we processed 100 virgin *fog-2* female *C. elegans* by isolating them in 1ml
823 of NGM buffer within an Eppendorf tube, following a protocol slightly modified from the previous study
824 [5]. These females were washed five times to clear bacterial contamination, then incubated in 100µl of
825 NGM or M9 buffer for 6 hours. A parallel extraction process utilized for *C. remanei* involved similar steps
826 but with only 5 females.

827 In Figure 1C, to evaluate PHD activation upon exposure to the volatile pheromone, we performed
828 calcium imaging with a custom-built spinning disk confocal microscope setup [34, 70]. Utilizing the
829 ZM9627 strain, which marks all neuronal nuclei with GCaMP6s and mNeptune [70] and incorporates
830 *him-5(e1490)* mutation to enrich for males. We also crossed ZM9627 with the CB5414 *srd-1(eh1)* line.
831 Preparation for imaging involved isolating L4 males 15-20 hours in advance, placing them on 10% agar
832 NGM buffer slides, and employing the Thin Layer Micro-Diffusion (TLMD) protocol (see Figure S10).
833 Approximately 5 ul of 0.2 um latex beads (Polysciences, Inc.) were added to aid immobilization. Imaging
834 was conducted with a 40x 0.95 NA objective, achieving 200 Hz to record 10 volumes per second, with
835 each comprising 20 optical slices. Pheromone or control buffer introduction occurred 30 seconds after
836 initiating imaging, continuing for an additional 3.5-9.5 mins. Subsequent processing and registration
837 allowed for tracking PHD neuron nuclei using semi-automated methods in MAMUT [104]. Intensities
838 from GCaMP and mNeptune channels were extracted for analysis within defined ROIs, calculating
839 neuronal activity ratios and smoothing data with Savitzky-Golay filters. The activity was quantified by
840 normalizing GCaMP fluorescence against mNeptune. We used the ratio F=F(GCaMP)/F(mNeptune), after
841 applying Savitzky-Golay filtering to each channel (polynomial order 1 and length 13) [115]. Z-score was
842 calculated as follows. Zi= (Fi – mean (F0s: F30s))/SD (F0s: F30s) (confirm if this notation is correct),
843 enabling a precise assessment of PHD neuron activation following sex pheromone exposure.

844 In Figure 3E, our study employed the same custom-built spinning disk confocal microscope setup
845 mentioned above and a sparse labeling markers pan-neuronal calcium imaging strain, ADS1046, which
846 features a dual expression of the calcium indicator GCaMP6s and the red fluorescent protein mNeptune
847 in all neuronal nuclei, alongside the *lite-1(ce314)* mutation to eliminate undesired light-induced neural
848 activity. This strain also has sparse labeling markers (*Pift-20*:BFP, P*eat-4*:cyOFP1, P*unc-17*:mScarlet, P*acr-*
849 *5*:BFP) for neuron identification. Intracellular calcium dynamics were quantified by tracking the calcium
850 indicator GCaMP6s signals, which enhances green fluorescence intensity within cells. Concurrently,
851 mNeptune signals were captured to serve as a reference. The intensity ratio of GCaMP to mNeptune
852 (GFP/RFP) at each time point was plotted. To aid neuron identification, after the recording session, we
853 acquired additional volumes using the following combination of excitation lasers and emission filters:
854 30% 640 nm 617/73 nm (200 Hz), 40% 561 nm 578 nm (200 Hz), 35% 488 nm 578 nm (200 Hz), 15% 488
855 nm (200 Hz), 95% 405 nm 440 or 450 nm (50Hz).

856 We fit the activity of AVA neurons by a linear combination of AWA and PHD neurons by minimizing the
857 least-squared error (Figure 3G).

858 **Neuron Tracking**

Each neuron was automatically tracked through all 3D volumes with targettrack. We first applied a strong low pass filter to blur the whole image and thresholded to find the general location of the head or tail. After centering each volume by the region found above, we cropped a rectangular ROI which covered the whole region for 99% of the recording. Then, we manually identified AWA, ASI, AVA, AVE, PHD neurons in each recording and annotated an average of 5 frames per recording. We used targettrack [106] to automatically segment and track each neuron in every volume. We trained the 3DCN of targettrack for 10K gradient steps with a batch size of 3. The quality of the tracking was manually verified after tracking.

The xyz coordinates were used to extract pixel intensities around neuronal nuclei. These changes were then standardized against the baseline pre-stimulation background, resulting in the relative intensity values (ΔR/R0) being displayed. Data representation is in the form of mean ± standard error of the mean (s.e.m.), processed using Graphpad Prism 6 and Microsoft Excel for comprehensive analysis. Custom Matlab code was utilized for graphing, with the ΔR/R0 average depicted by a black line and the s.e.m. by a gray-shaded envelope. The duration of stimulation is visually encoded on the plots with a pink color bar.

**Microfluidic chip design and manufacturing**

The design of our microfluidic devices is accomplished using SolidWorks software, tailored to the specific requirements of our experiments. The fabrication process utilizes both photolithography and polydimethylsiloxane (PDMS) soft lithography, as detailed in the literature [36, 116]. Initially, 3-inch silicon wafers were prepared by coating with a layer of SU-8 photoresist. This layer was subsequently patterned through photolithography, transforming the wafer into a mold for PDMS casting. For constructs intended for male worm imaging, the SU-8 2015 photoresist was spun at 1450 rpm to achieve a thickness of 24-25 µm. Following PDMS casting, the microfluidic devices were bonded to glass coverslips using a plasma cleaner, employing settings of 50mW power for 30 seconds to ensure a robust bond. This fabrication procedure is designed to produce precise microfluidic devices, enabling the simultaneous and individual delivery of stimulus to the head and tail regions of *C. elegans* males, while also facilitating concurrent calcium imaging. This chip allows for accurate delivery of stimulus to both the head and tail regions separately, with 4 inlets dedicated to each region and an additional outlet for waste. An optimized worm trapper adaptor from a previous study [117], secures males for imaging while ensuring both ends remain exposed to the stimulus channels. Designed stoppers within the tail inlet channels prevent the worms from escaping during injection, without disrupting fluid flow. This approach allows for the detailed study of neural responses to localized stimuli in a controlled environment.

**Sex pheromone preparation for microfluidic experiments**

To obtain large quantities of crude sex pheromone for microfluidic experiments, we modified the standard extraction protocol to avoid the time-consuming isolation of L4 stage *fog-2* females. We used 5-day-old *daf-22* mutant *C. elegans* hermaphrodites, which lack ascaroside synthesis, to ensure the absence of confounding neuronal responses from this water-soluble sex pheromone stimulus. Bleach-synchronized *daf-22* mutant worms were washed five times with M9 buffer. L1 stage arrest was induced by rotating worms in M9 buffer for 12 hours before seeding on culture plates (8-cm NGM with OP50, approximately 500 L1 worms/plate). Adult worms were collected after three days (at the onset of egg-laying). Adults were washed from culture plates with M9 buffer and separated from eggs using the precipitation method (repeated 5-7 times until eggs were absent). Separated adults were transferred to

new OP50-seeded plates, and this washing process was repeated for 6 days to exhaust self-sperm. Sex pheromone extraction was performed as described in "sex pheromone-induced pan-neuronal calcium imaging" with the following modification: instead of 100 worms/mL, we used 50µl of packed worm volume per 1mL of M9 buffer (see Figure S11 B, C). Three batches of extracted pheromone were tested for quality using a chemoattraction assay and combined to create a 100ml homogenous stimulus for microfluidic experiments.

**Microfluidic experiment calcium imaging and data analysis**

Young adult *C. elegans* males (PS10181) were loaded into a custom microfluidic chip that allows selective exposure of head and tail to odor solutions of choice. Solution administration was directed by an array of 8 memory-shape alloy valves (Takasago Fluidics Inc., Japan) individually addressed by an ESP32 microcontroller. Imaging was performed using a Leica DM6000 B microscope equipped with a X-Cite XLED1 Multi-Triggering LED illumination system (Excelitas Technologies) and iXon EMCCD detectors (Oxford Instruments Andor). Image acquisition and microfluidic stimulation administration were controlled and synchronized by a custom Python graphic interface using the Pycro-Manager interface for the Micro-Manager microscope control software [118]. Time-lapse image segmentation was performed using the pixel classification function of the Ilastik software and intensity values of GCaMP and RFP were extracted using a custom Jupyter notebook. The calcium imaging traces were calculated as the ratio of GCaMP6s/RFP fluorescence to correct for out-of-plane imaging artifacts. Because of the high background activity of the AVA neuron, baseline values for the calculation of the $\Delta R/R_0$ metric were estimated using the peakutils Python package. The relative intensity values ($\Delta R/R_0$) are plotted following the methodology outlined in "Sex Pheromone-Induced Pan-neuronal calcium imaging in *C. elegans*," with minor modifications. To quantify the effect of suppression/excitation on AVA neuron, we performed area-under-curve (AUC) analysis. We first compute the baseline AVA activity by averaging over the 3 mins before stimulation given at the most dilute concentration and subtract this baseline value from all signals. Then we integrate the area under curve for each worm data for 2 mins after the stimulation. For suppression, we only account for time intervals when the signal is lower than the baseline value; for excitation, we only account for time intervals when the signal is higher than the baseline value so that to naturally terminate the integration of area when the signal disappears. In Figure 4D, we compute the linear combination of AVA neuron activities with only head or tail stimulation (AVAhead+AVAtail) and compare that with the AVA neuron activity with simultaneous head and tail stimulation (AVAdual).

**Trajectory display and dot-display trajectory analysis of total/radial velocity**

Squared distance from the source and total velocity are computed to characterize the trajectories. For a random walk process that reaches the target point, the squared distance will decrease linearly with time.

A 3rd order Savitzky-Golay filter was used to preprocess the recorded trajectories and filter out high frequency twists of worm motions. We then computed the instantaneous velocities $\boldsymbol{v}(t)$ from the filtered trajectories, as well as the angle θ between the velocity direction and the direction towards the target in each frame. The total velocity is the magnitude $\boldsymbol{v}(t)$ of the computed velocities, and the radial velocity is the projection of velocities along the line connecting the worm position and the target $\boldsymbol{v}(t)\, cos\, \theta$.

For velocity statistics, we filtered the trajectory segments to remove those during turning and only used segments with $D_q < 0.2 \times \max(D_q)$ (see definition of $D_q$below).

**Concentration field simulation**

The concentration evolution inside the petri dishes was simulated using the Finite Element method. The simulated plates consist of a top layer of 4mm thick air and a bottom layer of 9mm thick agar. The diffusion coefficient of the sex pheromone was estimated $1.6\ mm^2/s$ in the air and $10^{-3}\ mm^2/s$ in the agar. The initial condition was set as concentration at the surface of the droplet $c_0 = 0.01\ mol/m^3$ while $c_0 = 0$ elsewhere. No-flux boundary condition was applied to the walls of the plate. For the dynamical simulations of worm searching, we take the 2D cross-section of the concentration field at z=-0.5 mm inside the agar (the air-agar interface is at z=0).

**Navigation simulation**

The navigation processes were simulated using an in-house extension of the HOOMD-Blue package. Mathematically, worm locomotion dynamics are described by the following equations:

$$d\boldsymbol{r} = \boldsymbol{Uqdt}, \boldsymbol{q} = (\cos\boldsymbol{\theta}, \sin\boldsymbol{\theta}), \boldsymbol{d\theta} = \sqrt{\boldsymbol{2D_R}}\boldsymbol{dW_S} + \boldsymbol{\gamma dW_T}.$$

Here, $\boldsymbol{r}$ is the position of the worm, U the velocity magnitude, **q** the orientation direction, $D_R$ the rotary diffusivity of the orientation angle $\theta$. $dW_S$ and $dW_T$ denote the standard Brownian motion on a circle $-\pi < \theta < \pi$ and a Poisson jump process respectively. $\boldsymbol{\gamma}$ is the intensity of the jump process, i.e., the tumbling rate. It has been observed[119] that during tumbles (large angle turns), the turning angle distribution displays a peak near π. Empirically, we represent the turning angle distribution as a mixture of uniform distribution and a wrapped Gaussian distribution:

$$T(\theta, \theta') = \alpha T_0 + (1-\alpha)T_1.$$

Here the turning kernel $T(\theta, \theta')$ is the probability of turning from $\theta'$ direction to $\theta$ direction. $T_0 = 1/(2\pi)$ is the uniform distribution and $T_1 = e^{-\frac{(\theta-\pi)^2}{2\sigma^2}}$ is a wrapped Gaussian distribution.

We adopt the following functional forms to reflect the above observed sensory neuron dynamics:

$$f_H = \frac{\dot{C}}{\dot{C}_0}\frac{1+tanh(log(C/C_0))}{2},$$

$$f_T =.$$

In the simulations, we fix $D_R = 0.02$, $\eta = 1$, $k_1 = 1/60$, $k_2^{H,T} = 1$.

# Figures and Figure Legends

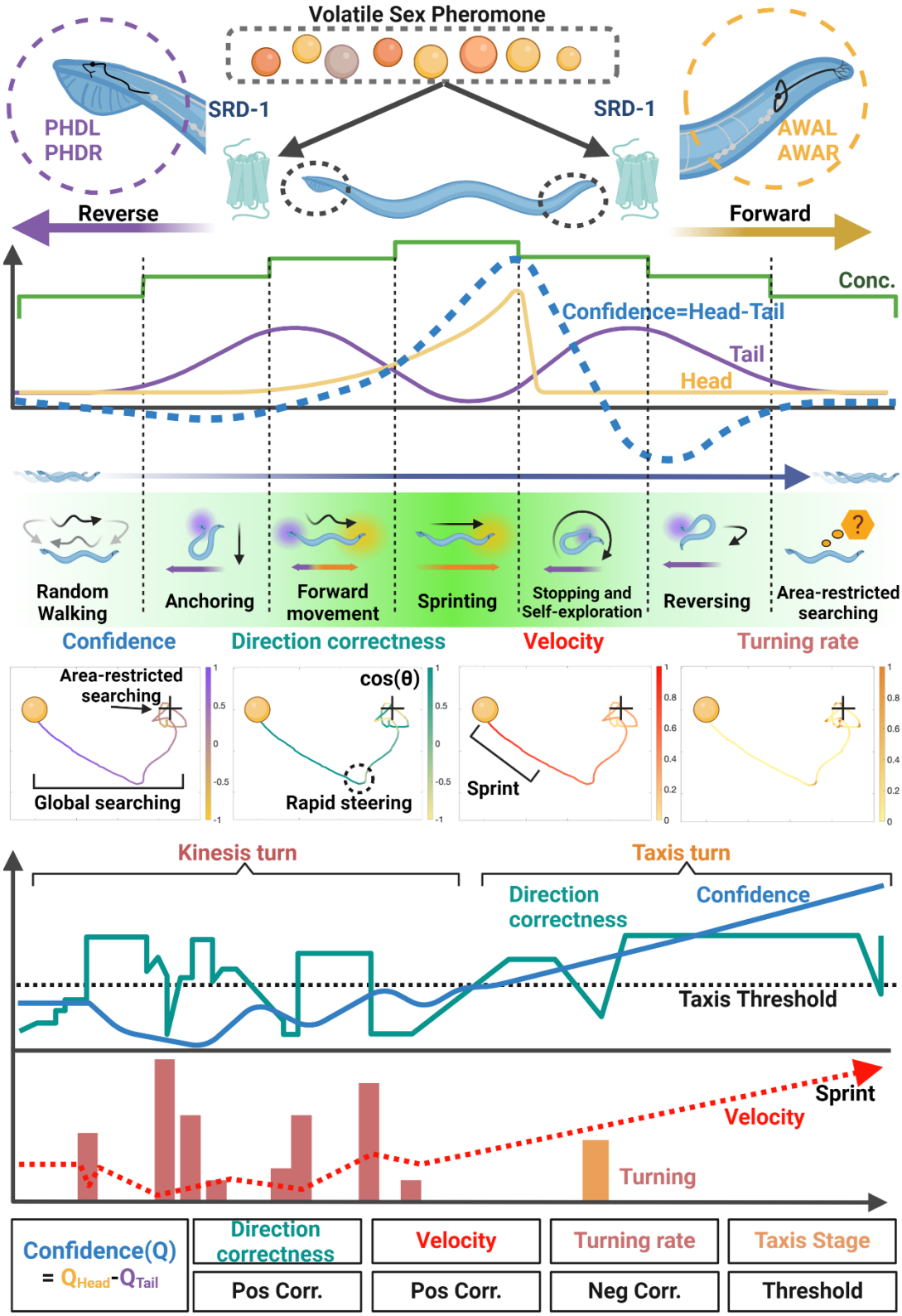

**Graphical abstract: Spatially separated pheromone detection drives adaptive navigation in *C. elegans* males**.

The **upper panel** illustrates how *C. elegans* males utilize spatially separated pairs of sensory neurons, AWA (head) and PHD (tail), that detect the same volatile sex pheromone molecule via the receptor SRD-1. Despite sharing this receptor, head neurons detect gradient changes and activate when concentration increases, suppressing turning, and promoting forward movement and acceleration. In contrast, tail neurons detect absolute concentration and activate at preferred moderate concentrations, inducing reversals and deceleration. The **middle panel** shows that upon initial pheromone introduction, simultaneous activation of head and tail neurons cancels each other out, causing males to transition from random walking to a stationary anchoring state, preventing them from chasing the concentration wave initially. As pheromone concentration increases, head neurons dominate, driving forward locomotion and acceleration. At the highest concentrations, tail neurons become less active while head neurons are highly activated, leading to rapid, goal-directed movement (sprinting). Incorrect directional choices result in AWA deactivation and persistent PHD activity, inducing pausing and local exploration. Repeated unsuccessful attempts trigger area-restricted searching. The **bottom panel** depicts our computational model which recapitulates these behaviors by integrating inputs from head and tail neurons. A confidence metric, which is positively correlated with directional accuracy and speed and negatively correlated with turning, is introduced. Once confidence surpasses a threshold, the model transitions from more random (kinesis) to more directed (taxis) movement. The depicted trajectories represent simulated behavior based on this confidence-driven model.

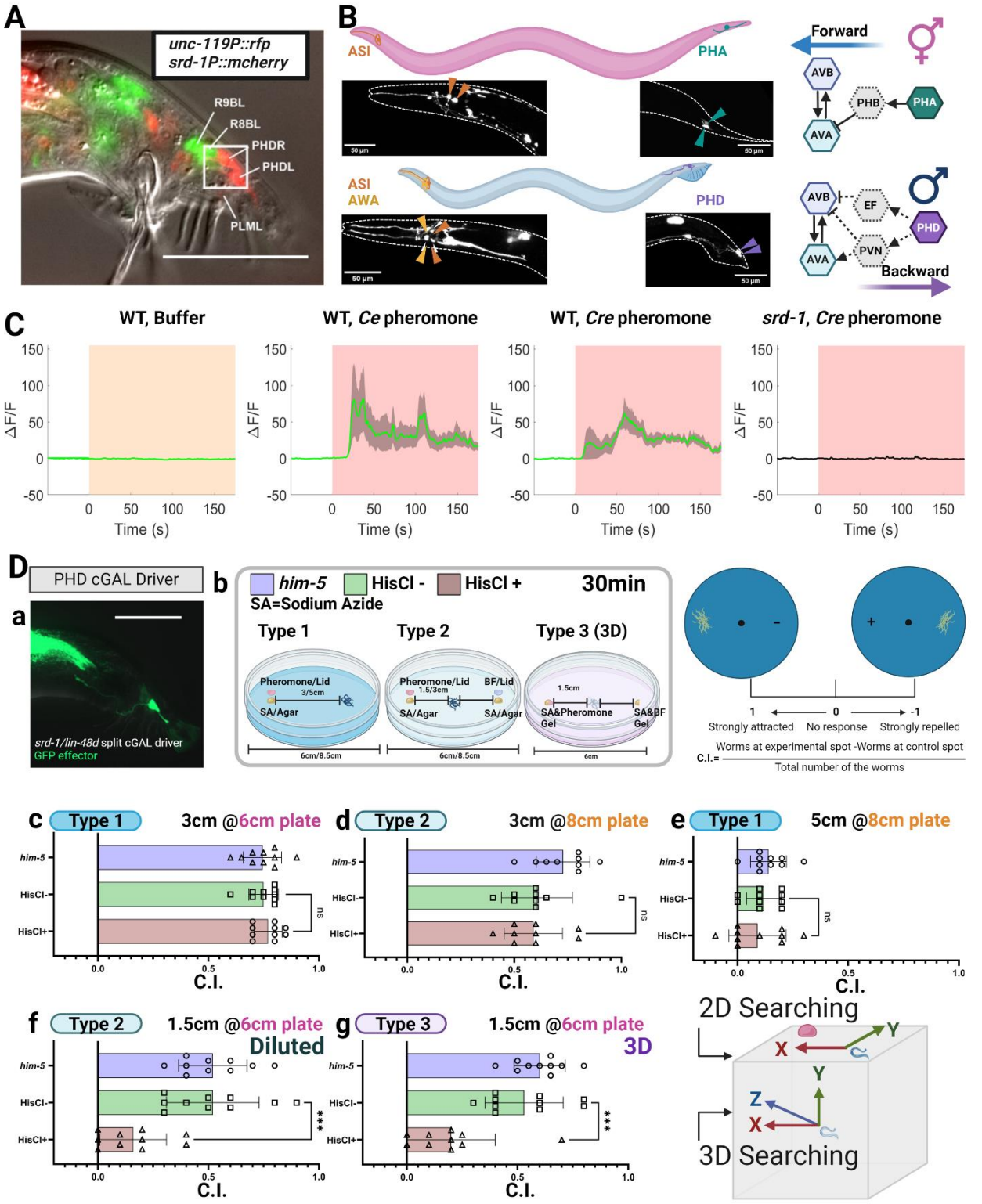
A
unc-119P::rfp
srd-1P::mcherry
R9BL
R8BL
PHDR
PHDL
PLML
B
ASI
PHA
Forward
AVB
PHB
PHA
AVA
ASI
AWA
PHD
AVB
EF
PHD
PVN
AVA
Backward
C
WT, Buffer
WT, Ce pheromone
WT, Cre pheromone
srd-1, Cre pheromone
ΔF/F
Time (s)
D
PHD cGAL Driver
a
srd-1/lin-48d split cGAL driver
GFP effector
b
him-5
HisCl -
HisCl +
30min
SA=Sodium Azide
Type 1
Type 2
Type 3 (3D)
Pheromone/Lid
3/5cm
SA/Agar
Pheromone/Lid
1.5/3cm
BF/Lid
SA/Agar
SA/Agar
1.5cm
SA&Pheromone Gel
SA&BF Gel
6cm/8.5cm
6cm/8.5cm
6cm
1
0
-1
Strongly attracted
No response
Strongly repelled
C.I.=
Worms at experimental spot -Worms at control spot
Total number of the worms
c
Type 1
3cm @6cm plate
d
Type 2
3cm @8cm plate
e
Type 1
5cm @8cm plate
him-5
HisCl-
HisCl+
ns
C.I.
f
Type 2
1.5cm @6cm plate
Diluted
g
Type 3
1.5cm @6cm plate
3D
***
**
2D Searching
3D Searching
X
Y
Z

1061

**Figure 1: *srd-1* sexual dimorphism in expression patterns and male PHD neuron excitation triggered by sex pheromone depends on the chemoreceptor SRD-1. (A)** Expression pattern of *srd-1*::mCherry in male tail. *srd-1* is expressed in a pair of PHD cells located in tail region of male *C. elegans*. PHD neurons are defined based on its location in the tail ganglia, and its process morphology, with P*unc-119*::rfp indicating all neuronal cell bodies. SRD-1 is not expressed in Ray B neurons (Figure S1) as reported in the literature before the existence of PHD was known[67, 68]. **(B)** Sexual dimorphic expression of *srd-1* in both head and tail: *srd-1* GFP reporter expression in AWAs, ASIs and male-specific neuron PHDs in males and in ASIs and PHAs in hermaphrodites. *rab-3P::mCherry* marks all neurons; an integrated cGAL-UAS line *(srd-1P*::GAL4; UAS::GFP*)* reports *srd-1* expression. The right panel shows the expression pattern summary of *srd-1* in both males and females, along with the predicted neural circuits it might be involved in, based on their connectome and functional connectome insights. **(C)** Sex pheromone-triggered activation of PHD neurons, exhibiting SRD-1-dependent excitation, was observed through pan-neuronal calcium imaging with *rgef-1P*::GcaMP6s; a pan-neural marker (*rgef-1P*::mNeptune) indicated all neuron cell body locations (sample size: 5-7 worms). Shaded areas represent the s.e.m. **(D)** Exploring the role of PHD neurons in mate-searching efficiency. **(a)** Verification of SRD-1 expression in the PHD neuron using a split cGAL driver with *lin-48d* and *srd-1* promotor. This approach also generated a PHD-specific driver for targeted manipulation of the PHD neuron. Male tail image of cGAL-UAS line: *lin-48d*p::NLS::cGAL (DBD); *srd-1p*::NLS::cGAL (AD), 15XUAS::GFP. **(b)-(g)** Impact of PHD inhibition on male mate-searching efficacy under varied task complexities. **(b)** Schematic representation of the chemoattraction assay and the calculation of the Chemoattraction Index (C.I.). **(c)-(g)** Males with HisCl induced PHDs inhibition (split cGAL-UAS bipartite system line: *lin-48dP*-NLS-cGAL (DBD); *srd-1P*-NLS-cGAL (AD) driver; UAS:: HisCl effector) can effectively locate sex pheromones in basic navigation tasks as control lines ( WT and HisCl-absent sample); however, their ability to detect a 10X diluted sex pheromone and navigate through 3D environments is significantly impaired. The sample size for each assay consisted of 110-120 worms. ***$P < 0.001$, not significant (ns): $P > 0.05$. Two-tailed unpaired t-test. Error bars represent the s.e.m.

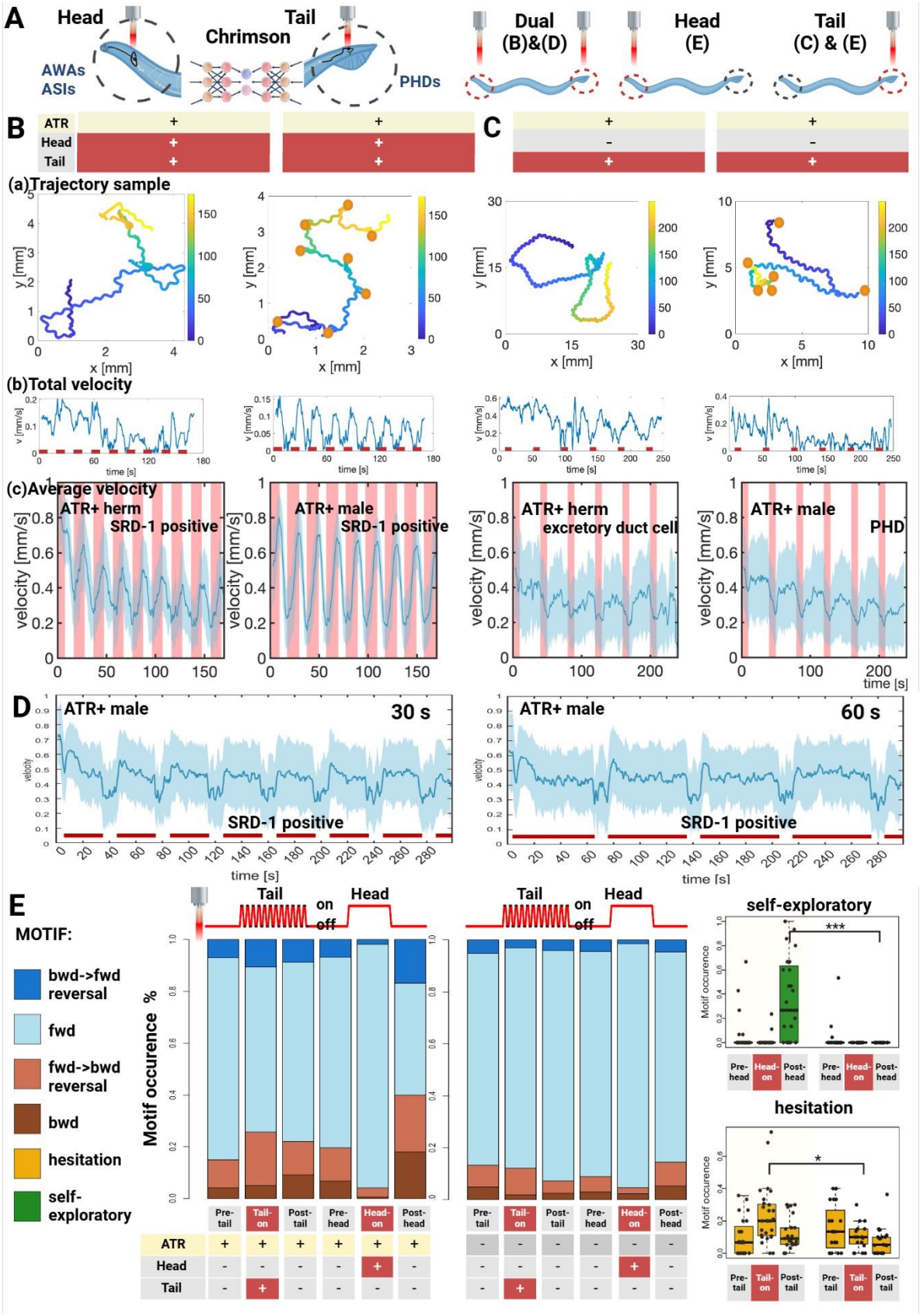
A
Head
Tail
Chrimson
AWAs
ASIs
PHDs
Dual (B)&(D)
Head (E)
Tail (C) & (E)
B
ATR
Head
Tail
C
(a)Trajectory sample
x [mm]
y [mm]
(b)Total velocity
v [mm/s]
time [s]
(c)Average velocity
ATR+ herm
SRD-1 positive
ATR+ male
SRD-1 positive
ATR+ herm
excretory duct cell
ATR+ male
PHD
velocity [mm/s]
time [s]
D
ATR+ male
30 s
60 s
SRD-1 positive
velocity
time [s]
E
MOTIF:
bwd->fwd reversal
fwd
fwd->bwd reversal
bwd
hesitation
self-exploratory
Motif occurence %
Tail on off
Head
Pre-tail
Tail-on
Post-tail
Pre-head
Head-on
Post-head
self-exploratory
hesitation
Motif occurence
***
*

1109

**Figure 2: Contrasting locomotor responses to optogenetics activation of SRD-1 positive neurons and PHD neurons. (A)** Schematic diagram of the optogenetic experiment: Using *srd-1* or PHD-specific drivers with Chrimson effector in cGAL-UAS lines and region-specific light sources, we precisely targeted the head or tail regions of freely moving males to evaluate locomotion effects and characterize distinct micro-behaviors. **(B)** Sex-specific locomotor responses to SRD-1 positive neuron activation in *C. elegans*. SRD-1 positive neurons (*srd-1*P-NLS-cGAL driver) were activated in both sexes using Chrimson (UAS::Chrimson effector). The stimulation protocol consisted of 12.5-second light-on intervals followed by 7.5-second light-off intervals, forming a 20-second cycle. Light stimulation is represented by the pink bar in the figure. **(C)** PHD neuron activation effects on male locomotion: triggers slowdown and reversal. Targeting PHD neurons with a split cGAL-UAS bipartite system line: *lin-48dP*-NLS-cGAL (DBD); *srd-1P*-NLS-cGAL (AD) driver). The stimulation protocol consisted of 10-second light-on intervals followed by 30-second light-off intervals, forming a 40-second cycle. Light stimulation is represented by the pink bar in the figure. **(a, b)** A representative trajectory sample and its corresponding total velocity time series, V(t), are shown. The red line indicates periods of light stimulation. **(c)** V(t) averaged over 30 samples. Red shade indicates light stimulation. (c), (d) Shaded areas represent the std. **(D)** Persistent enhancement of forward movement upon activation of SRD-1 positive neurons, sustained for up to 60 seconds. The stimulation protocol involved 30- or 60-second light-on intervals followed by 10-second light-off intervals. Sample size: 100–110 worms. **(E)** Characterizing micro-behavioral responses to optogenetic stimulation of SRD-1 positive neurons in male *C. elegans*' anterior and posterior regions. With *srd-1* drivers and Chrimson effectors in cGAL-UAS lines combined with region-specific light sources, we precisely targeted the head or tail regions of freely moving males to analyze locomotion effects and characterize specific micro-behaviors. Region-specific stimulation of SRD-1 positive neurons results in varied behavioral responses, underscoring the distinct roles of these neuron groups in locomotion. The sample size for ATR+ group consisted of 18 worms. The sample size for ATR- group consisted of 12 worms. ***$P < 0.001$; **$P < 0.005$; *$P < 0.05$.

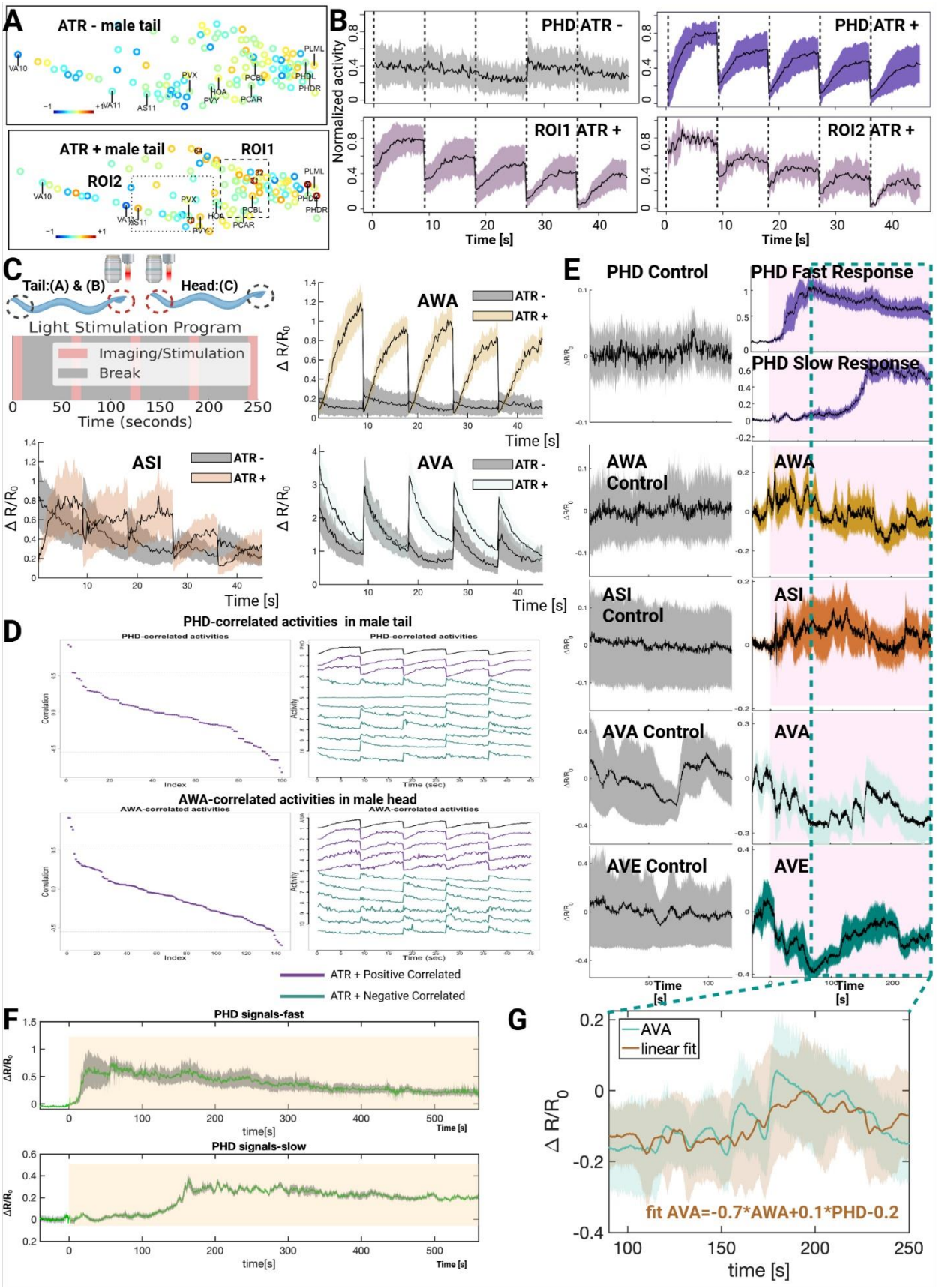
A
ATR - male tail
ATR + male tail
ROI1
ROI2
B
PHD ATR -
PHD ATR +
ROI1 ATR +
ROI2 ATR +
Normalized activity
Time [s]
C
Tail:(A) & (B)
Head:(C)
Light Stimulation Program
Imaging/Stimulation
Break
Time (seconds)
AWA
ASI
AVA
ATR -
ATR +
Δ R/R0
Time [s]
D
PHD-correlated activities in male tail
AWA-correlated activities in male head
ATR + Positive Correlated
ATR + Negative Correlated
E
PHD Control
PHD Fast Response
PHD Slow Response
AWA Control
AWA
ASI Control
ASI
AVA Control
AVA
AVE Control
AVE
Time [s]
F
PHD signals-fast
PHD signals-slow
time[s]
G
AVA
linear fit
fit AVA=-0.7*AWA+0.1*PHD-0.2
time [s]

1156

**Figure 3: neural activation and correlation patterns following srd-1 positive neuron optogenetic stimulation and pheromone exposure. (A)** Representative activation patterns were observed in male tail neurons upon optogenetic stimulation of SRD-1 positive neurons. Through visual analysis, two regions, designated as ROI1 and ROI2, were identified as containing neurons with strong correlations to PHD activity (correlation coefficient >0.55) (See Figure S7). **(B)** PHD neurons exhibited increased activity upon light stimulation of SRD-1 positive neurons in the tail region in ATR+ males (top right), but not in ATR- males (top left).Bottom: traces of neuronal activities of neurons correlated with PHD ATR+, in two regions (ROI1 and ROI2) which often contained neurons strongly correlated with PHD. The sample sizes: control (n=9) and experimental (n=12). **(C)** Upper left panel: Schematic representation of the optogenetic activation protocol, consisting of five 10-second imaging/stimulation intervals interspersed with 50-second breaks. Neuronal activation of AWA, ASI and AVA neurons after optogenetic activation of SRD-1 positive neurons on head region; sample sizes: control and experimental groups (n=8 each). **(D)** Representative neural activity correlation with SRD-1 positive neuron optogenetic stimulation in male tail and head regions. Sample sizes were n(head)=7 and n(tail)=12. Color key: Yellow denotes positive correlation with target neuron activity (ATR+ samples), light green denotes negative correlation. **(E)** Calcium responses in PHD, AWA, ASI, and reversal commanding neurons AVA and AVE upon 250 seconds of pheromone stimulation in both tail and head regions. Sample sizes for both regions are control (n=5) and experimental (n=8). (B), (C), and (E) Shaded areas represent the s.e.m. **(F)** Calcium responses of PHD neurons over 9.5 mins of pheromone stimulation, with data grouped by response initiation time into two categories. **(G)** Fitting AVA neuron activity data using a linear combination of AWA and PHD neuron activity, focusing on the period both AWA and PHD neurons activated. The best-fit equation for AVA activity is: AVA activity=−0.7×AWA activity+0.1×PHD activity−0.2. This model indicates a weighted influence of AWA and PHD neuron activities on AVA neuronal response.

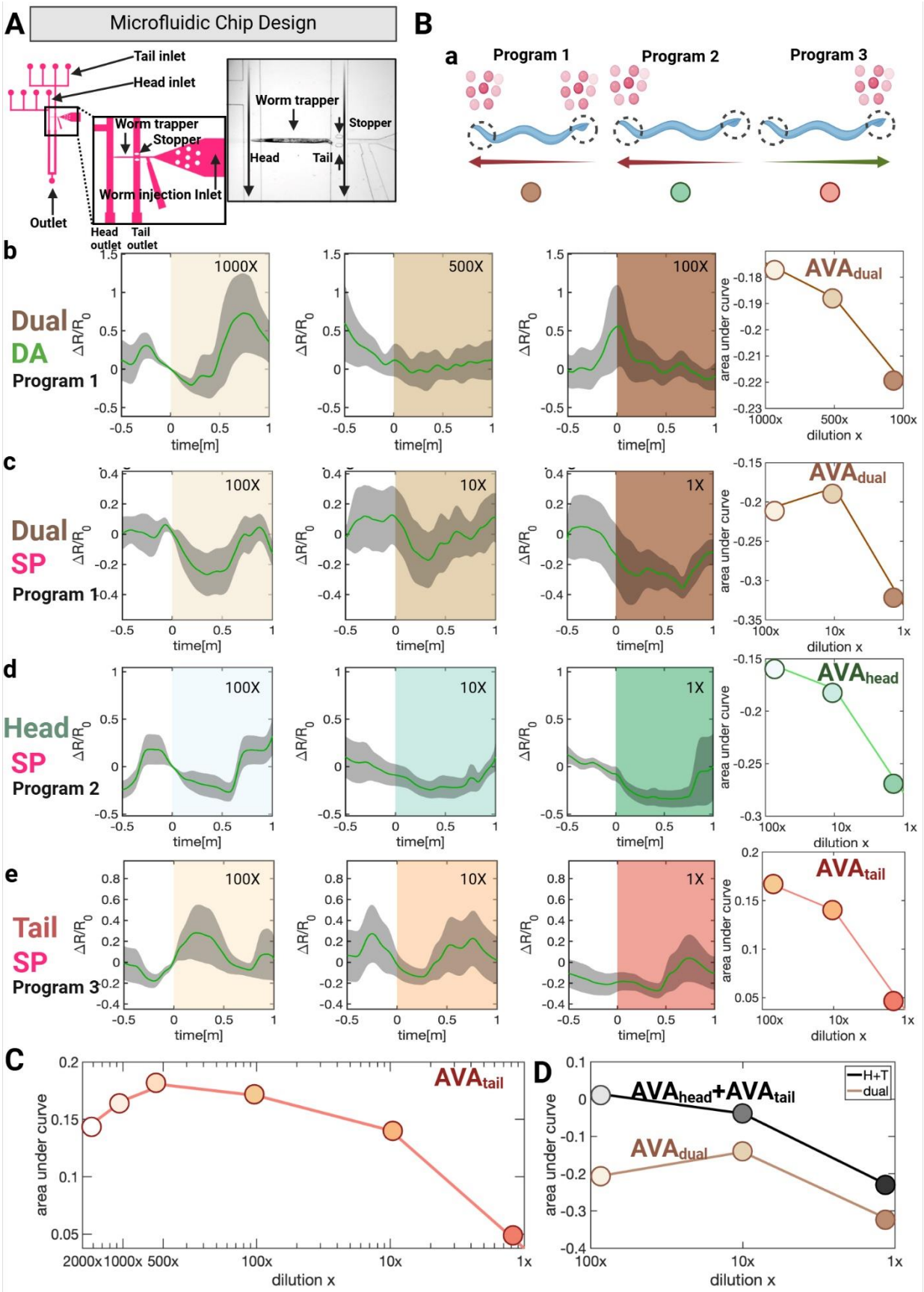
A
Microfluidic Chip Design
Tail inlet
Head inlet
Worm trapper
Stopper
Worm injection Inlet
Outlet
Head outlet
Tail outlet
Worm trapper
Stopper
Head
Tail
B
a
Program 1
Program 2
Program 3
b
Dual
DA
Program 1
1000X
500X
100X
AVAdual
c
Dual
SP
Program 1
100X
10X
1X
AVAdual
d
Head
SP
Program 2
100X
10X
1X
AVAhead
e
Tail
SP
Program 3
100X
10X
1X
AVAtail
ΔR/R0
time[m]
area under curve
dilution x
C
AVAtail
area under curve
dilution x
D
AVAhead+AVAtail
AVAdual
H+T
dual
area under curve
dilution x

1194

**Figure 4: Dissecting reversal command neuron responses across different sex pheromone concentrations by microfluidic experiment (A)** Schematic of the head and tail microfluidic chip designed for precise, independent delivery of target concentration stimuli to the head and tail regions separately. This chip allows for controlled, localized stimulation, enabling the delivery of different stimuli to the head and tail simultaneously. The chip includes four inlets on both the head and tail sides with a male-size-adapted worm trapper connected to a worm injection inlet. Two stoppers within the trapper intersect the tail inlet region, preventing worm escape into the tail inlet or outlet during injection. All inlets converge into a wider outlet for efficient waste and used worm collection. **(B) (a)** Schematic diagram of stimulation program and predicted behavioral outcomes. **(b)-(e)** Effects of diacetyl and sex pheromone stimulation on AVA reversal command interneuron activity in *C. elegans* males. The calcium indicator GCaMP6s was used to monitor calcium dynamics in the AVA neuron. The AVA-specific split cGAL driver construct consisted of *gpa-14P*::NLS::cGAL (DBD)::gp41-1::N-intein::*let-858* 3'UTR and *rig-3P*::NLS::gp41-1::C-intein::cGAL(AD)::*let-858* 3'UTR, paired with the GCaMP effector construct 15xUAS::GCaMP7b::SL2::mKate2. Diacetyl and dual-sided sex pheromone stimulation reduce AVA activity, as does head-specific pheromone stimulation, whereas tail-specific pheromone stimulation activates AVA neurons. Shaded areas represent the standard error of the mean (s.e.m.). The right panel shows area-under-curve (AUC) analysis (see Method), indicating that dual-sided diacetyl and sex pheromone stimulation, as well as head-specific pheromone stimulation, exert the strongest inhibitory effects on AVA at the highest tested concentration. Tail-specific pheromone stimulation produces peak AVA activation at the lowest tested concentration (100-fold dilution). **(C)** Further testing of three additional diluted concentrations reveals that tail-specific stimulation elicits the highest activation of the AVA neuron at an intermediate concentration (500-fold dilution), with activation levels decreasing at both higher and lower concentrations. **(D)** The area under the curve (AUC) for AVA neuron activation resulting from head-specific stimulation combined with tail-specific stimulation closely matches the trend observed with dual stimulation alone.

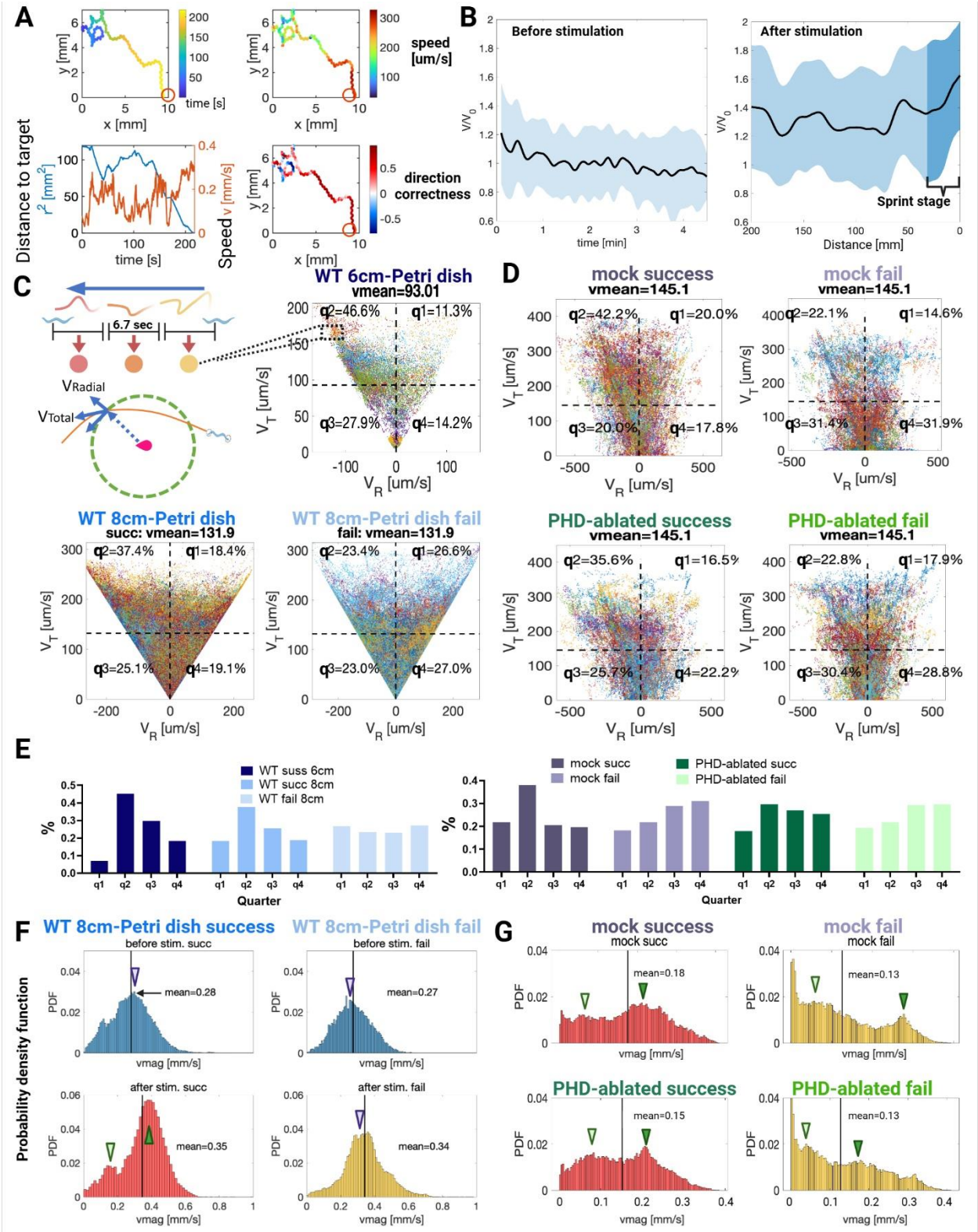


1238
1239
1240

**Figure 5: PHD neuron ablation disrupts orthokinetic responses to sex pheromone in males. (A)** A representative trajectory of WT adult males navigating toward sex pheromone, with colors indicating escape time, speed, and directional accuracy in respective panels. The bottom left panel shows the squared distance from the pheromone source (blue) and absolute velocity (red) over time. Velocity adapts to changes in pheromone concentration, as reflected by fluctuations in the squared distance from the source. Velocity values are averaged over 20 frames. **(B)** Velocity before (left) and after (right) pheromone stimulation of sex pheromone droplet search in 8-cm plate. After placing worms on an agar plate for acclimation (2 mins), video recording started to capture their pre-stimulation behavior for 5 mins. Subsequently, a drop of sex pheromone was introduced, initiating the stimulation phase. Recording continued for an additional 15 mins to observe post-stimulus behavior. $V_0$ is the average velocity of each worm before the stimulation. Left: velocity fluctuations before stimulation. Right: velocity (normalized by $V_0$) as a function of distance to the source. A sprint stage is identified when worms are very close to the source. Shaded areas represent the std. **(C)** Dot-display trajectory analysis (see Method) of WT *C. elegans* males during sex pheromone-triggered navigation in 6- and 8-cm Petri dishes. Trajectories were segmented into 6.7-second intervals (50 frames), with radial velocity plotted on the x-axis and total velocity on the y-axis. The gating strategy for analyzing the dot plots includes the mean total velocity of all worms under the same test condition and initial positions. The gating mean total velocity is indicated at the top of each panel. All tested males successfully located the target in the 6-cm plate condition. **(D)** The same trajectory analysis as in 5(C) was applied to control mock worms and PHD-laser ablated males navigating toward freely moving *fog-2* females. To ensure a fair comparison, the gating strategy for dot plot analysis includes the mean total velocity of all worms from both subgroups and their initial positions. The gating mean total velocity is indicated at the top of each panel. (C) and (D) illustrate differences in velocity dynamics based on target movement. In Panel C, where the target is fixed, the total velocity always exceeds the radial velocity, resulting in a defined boundary along the plot edge. In contrast, Panel D shows data for a moving target, where the target's motion can oppose the worm's trajectory, leading to instances where total velocity is less than radial velocity. This results in a more dispersed shape without a clear boundary, reflecting the complex interactions between worm movement and target direction. **E)** Bar plot illustrating the percentage distribution for each quarter as derived from the data in panels C and D. **(F)** Velocity distribution patterns during sex pheromone droplet search in an 8-cm plate. The upper panels display velocity distributions prior to pheromone stimulation, while the lower panels show distributions after stimulation. Samples are divided into two subgroups based on whether the individuals successfully located the target or not. **(G)** Velocity distribution patterns during freely moving *fog-2* females navigation in mock and PHD-laser ablated groups. The panels show velocity distributions for each condition, with groups separated by navigation outcome (success vs. failure). For (F) and (G), the black line indicates the mean velocity for each group. Statistical analysis was performed using a two-tailed unpaired t-test. Significance thresholds are indicated as ***$p < 0.001$ and not significant (ns): $p > 0.05$. Sample sizes for the WT animal study include 100 and 102 worms for experiments conducted on 6-cm and 8-cm Petri dishes, respectively. The mock group consists of 30 worms, and the PHD-laser ablated group consists of 31 worms.

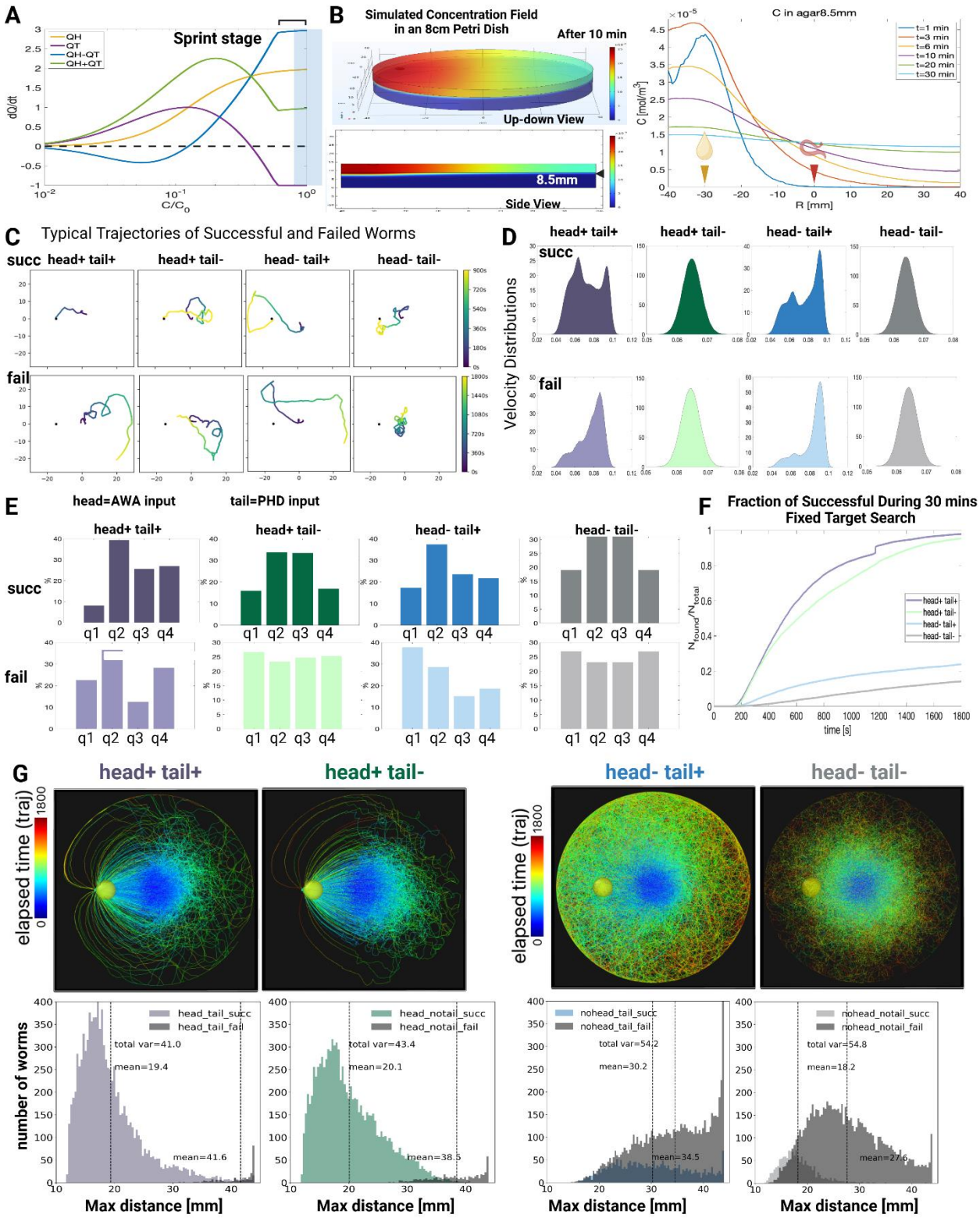
A
Sprint stage
QH
QT
QH-QT
QH+QT
dQ/dt
C/C0
B
Simulated Concentration Field in an 8cm Petri Dish
After 10 min
Up-down View
8.5mm
Side View
C in agar8.5mm
t=1 min
t=3 min
t=6 min
t=10 min
t=20 min
t=30 min
C [mol/m3]
R [mm]
C
Typical Trajectories of Successful and Failed Worms
succ
fail
head+ tail+
head+ tail-
head- tail+
head- tail-
D
Velocity Distributions
E
head=AWA input
tail=PHD input
q1 q2 q3 q4
F
Fraction of Successful During 30 mins Fixed Target Search
time [s]
G
elapsed time (traj)
number of worms
Max distance [mm]
head_tail_succ
head_tail_fail
total var=41.0
mean=19.4
mean=41.6
head_notail_succ
head_notail_fail
total var=43.4
mean=20.1
mean=38.5
nohead_tail_succ
nohead_tail_fail
total var=54.2
mean=30.2
mean=34.5
nohead_notail_succ
nohead_notail_fail
total var=54.8
mean=18.2
mean=27.6

**Figure 6: Simple dynamic model for a navigation mechanism with antagonistic detectors. (A)** Schematic plot illustrating how confidence change rates depend on absolute concentration $C$ in the model. $C_0$ is the reference concentration at the pheromone source. For head input $Q^H$, a fixed concentration change rate is assumed for the sensory input. At low $C$, both head ($Q^H$) and tail ($Q^T$) inputs accumulate slowly. At intermediate $C$, tail input accumulates faster than head input. However, as $C$ further increases, tail input starts to accumulate slower and is eventually suppressed, while head input signal is monotonically stronger as $C$ increases until saturation at very high $C$. The high $C$ regime corresponds to large $Q^H - Q^T$ which leads to the sprint behavior. **(B)** The left panel illustrates the simulated concentration field within an 8-cm Petri dish 10 mins after stimulus introduction. The experimental setup involved placing stimulus on the lid of a Plate half-filled with agar (9mm thickness), establishing a dual-layer distribution for the volatile component. The black arrowhead marks the layer position corresponding to the details provided in the right panel. The right panel captures the evolution of the concentration field at the air and agar interface (8.9mm) over a 30-minute duration. **(C-G)** Simulation results to compare the roles of head and tail inputs. **(C)** Typical trajectories of successful and failed subgroups under different conditions of head/tail inhibition. **(D)** Velocity distributions under each condition for both groups. Regardless of head activation, tail activation results in bimodal distributions for the successful group similar to experiment observations, while tail inhibition results in always monomodal distributions. **(E)** Statistics for orthokinesis under four different head or tail input-enabled conditions are shown, with a bar plot illustrating the percentage distribution for each quarter as derived from the dot-display trajectory analysis (see Method and Figure 5C). **(F)** Fraction of worms that have found source during 30min search task under each condition. Tail activation results in slightly better performance for head-activated worms (compare purple and green curves) and about twice better for head-inhibited worms (compare blue and grey curves). No taxis happen under head inhibition. **(G)** The upper panel shows the simulation snapshots comparing four head/tail input-enabled conditions, showing the maximum distances each worm reaches from the pheromone source over 30 mins, starting at an average distance of 15 mm. The figure displays trajectories of 1,000 randomly selected worms from 10,000 stimulation events that are color-coded by elapsed time. The bottom panel shows the maximum distance reached on the X-axis and the number of worms on the Y-axis for successful and failed attempts across four different head or tail input-enabled conditions, with a simulated data sample size of 10,000. The mean of maximum distance and total variance are indicated in each panel.

1324 **Supplementary Figure and Legends**

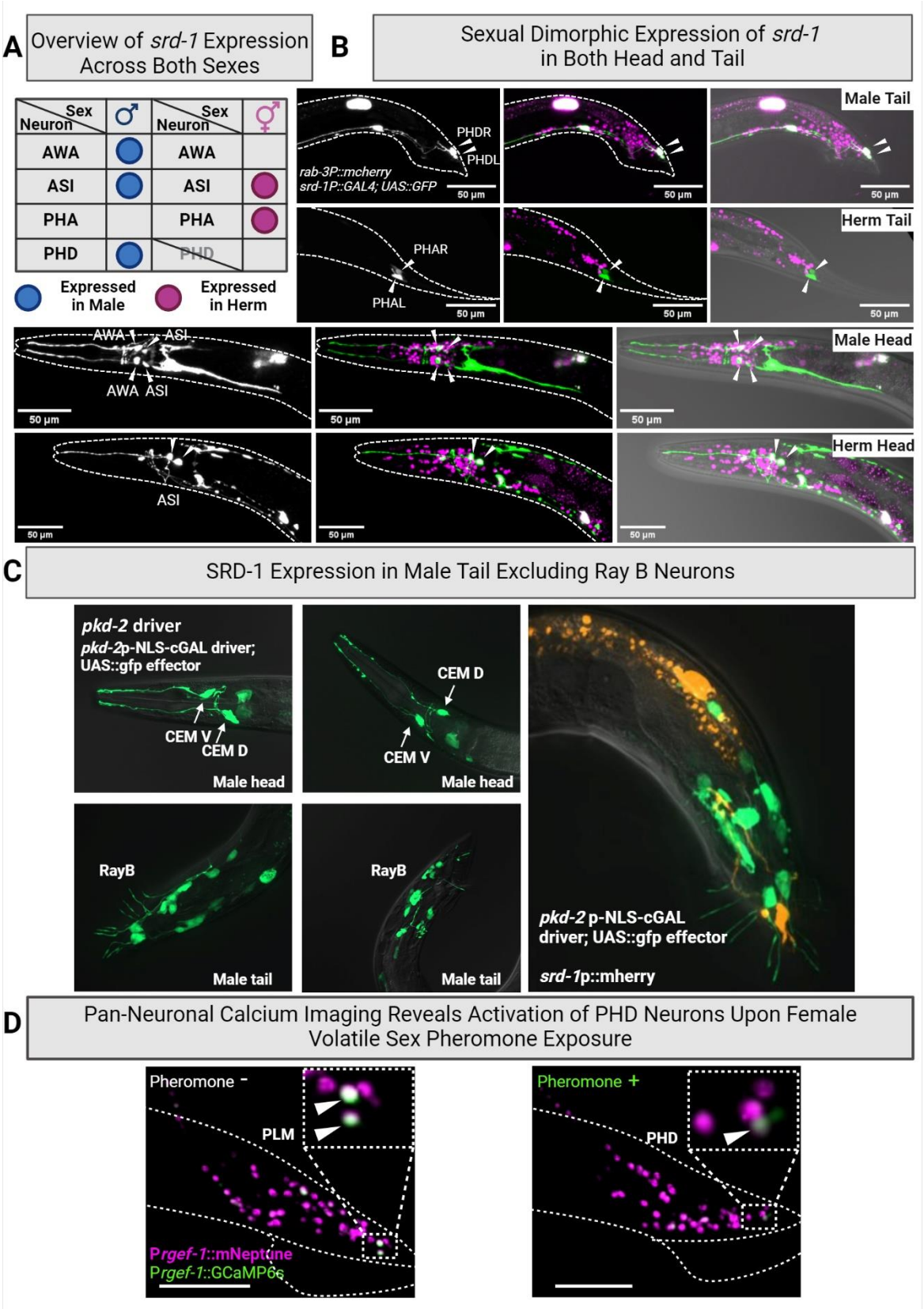

**Figure S1: Localization of SRD-1 expression in the male tail, excluding ray B neurons. (A)** Overview of *srd-1* expression patterns in both sexes. **(B)** Sexual dimorphic expression of *srd-1* in both head and tail: *srd-1* GFP reporter expression in AWAs, ASIs and male-specific neuron PHDs in males and in ASIs and PHAs in hermaphrodites. *rab-3P::mCherry* marks all neurons; an integrated cGAL-UAS line *(srd-1P*::GAL4; UAS::GFP*)* reports *srd-1* expression. **(C)** Visualization of *pkd-2* expression in the male tail region using a cGAL-UAS system: *pkd-2P*-NLS-cGAL driver combined with a UAS::gfp effector. PKD-2 is known to be expressed in CEM neurons in the head and Ray B neurons in the tail. The figure presents two representative males. Absence of overlap between PKD-2 (GFP) and SRD-1 (mCherry) expressions in the male tail region, utilizing *pkd-2p*-NLS-cGAL driver and UAS::*gfp* effector in combination with *srd-1p*::mCherry, demonstrating distinct expression domains. **(D)** Excitation of GCaMP6s reporter in PHD neurons observed in pan-neuronal calcium imaging upon sex pheromone stimulation. PLMs are spontaneously activated before stimulation, and PHDs are activated after applying sex pheromone.

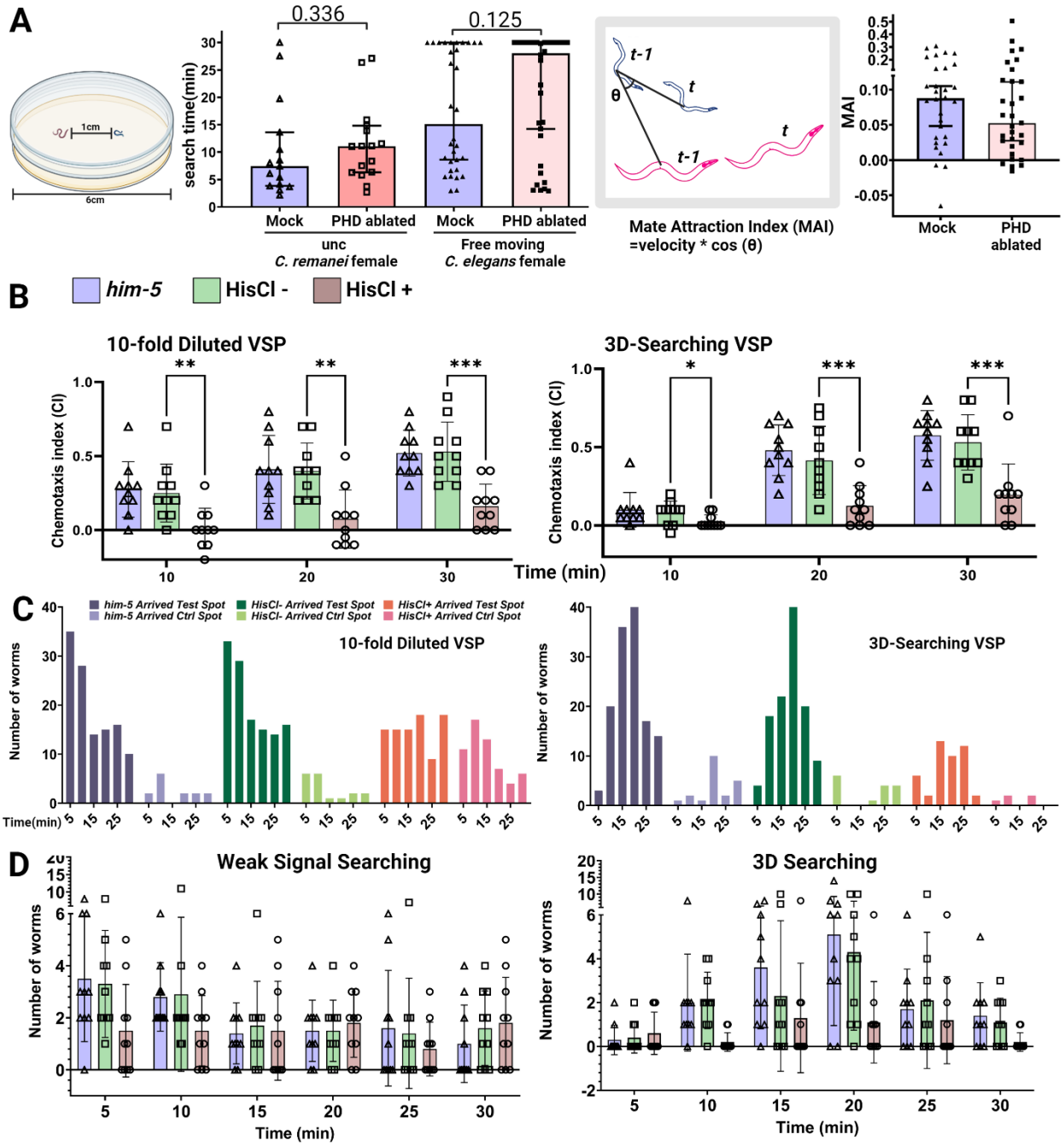


1356

1357
1358
1359
1360
1361
1362
1363

**Figure S2: Impaired ability of males to locate *fog-2* females over distance and their chemotaxis performance in weak signal and 3D searching. (A)** Female-seeking efficacy: PHD-laser ablated males experience slight delays in finding uncoordinated *C. remanei* (*unc*) and more obverse delays in finding free-moving *C. elegans* (*fog-2*) females compared to controls. Also, PHD-laser ablated males are less attracted by *C. elegans* females. The sample size for each assay consisted of 26-30 worms. Error bars represent the s.e.m. **(B)** The distribution of worms at various intervals following stimulus shows a consistently low chemotaxis index in PHD-inhibited males. **(C)** Presents the number of worms reaching a pheromone target spot at various time points during weak signal searching and 3D searching assays. The analysis of worm distribution at multiple time points after the introduction of the stimulus indicated a consistently low number of the PHD-inhibited males arrived at the test spot across all intervals, highlighting their compromised chemotactic ability. **(D)** Different navigational deficits in PHD-inhibited males across different exploration tasks: in weak signal tasks, their even distribution between test and control spots led to a low chemotaxis index; in 3D tasks, the low index resulted from fewer males reaching the target. *$P < 0.05$, **$P < 0.01$, ***$P < 0.001$, not significant (ns): $P > 0.05$. Two-tailed unpaired t-test. Error bars represent the s.e.m.

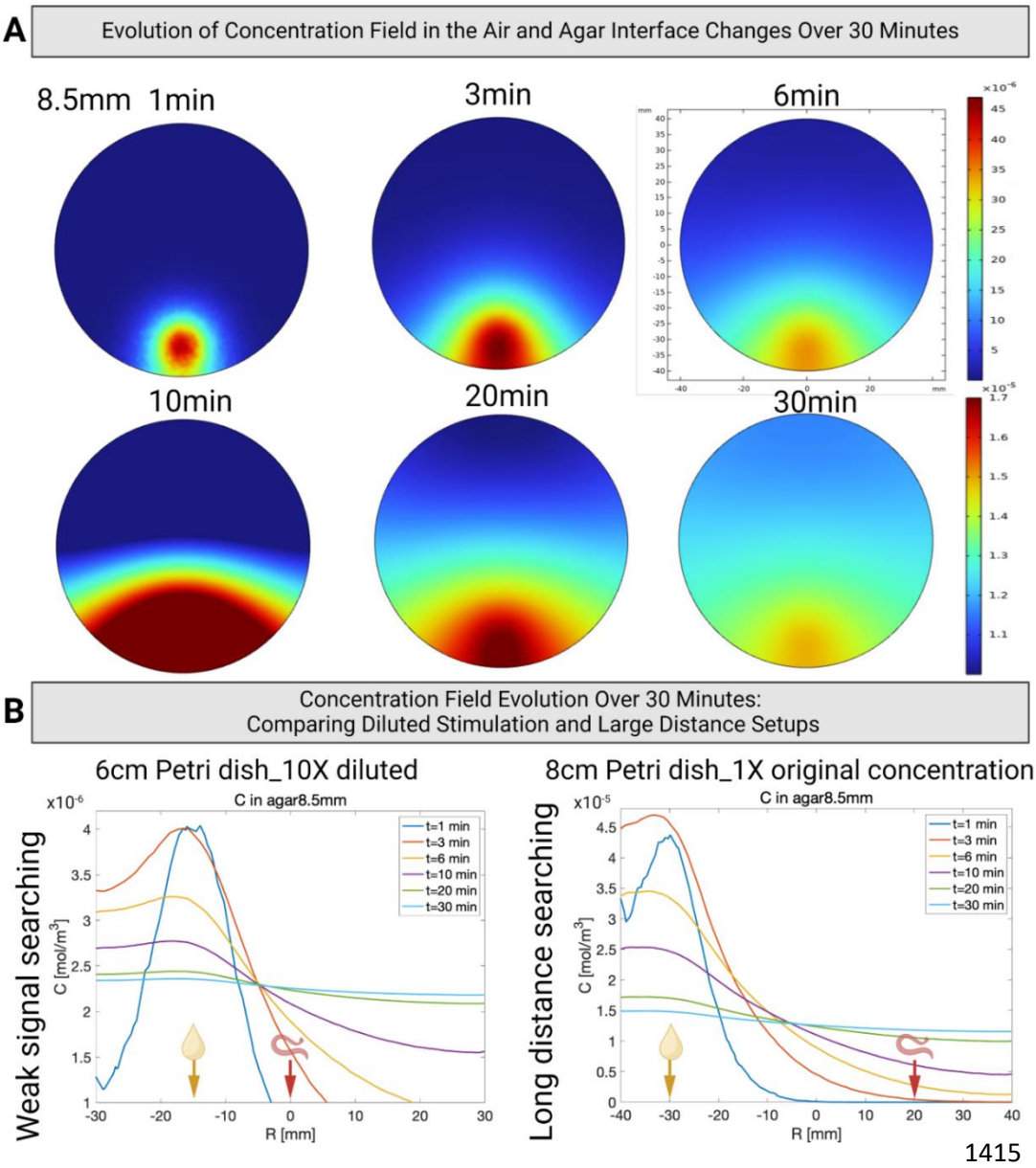


**Figure S3: Visualization and dynamics of pheromone concentration fields in chemoattraction assays. (A)** Captures the evolution of the concentration field at the air and agar interface (8.9mm) over a 30-minute duration. The color scales for 1min, 3min, and 6min intervals are consistent, as are those for 10min, 20min, and 30min intervals, as indicated on the right side of the panel, illustrating the dynamic changes in pheromone distribution. **(B)** Compares the evolution of the concentration field over 30 mins between diluted stimulation and large distance setups. The concentration field simulation shows that in scenarios where males are positioned far from the pheromone source, they experience areas of low absolute concentration lacking a clear gradient. In contrast, proximity to a diluted pheromone source results in a Gaussian distribution with a discernible gradient, despite the overall low concentration level, indicating different challenges in pheromone detection and navigation based on distance and concentration.

Impaired Free Moving *fog-2* female Search
in PHD Neuron Laser Ablated males

## Mock Control

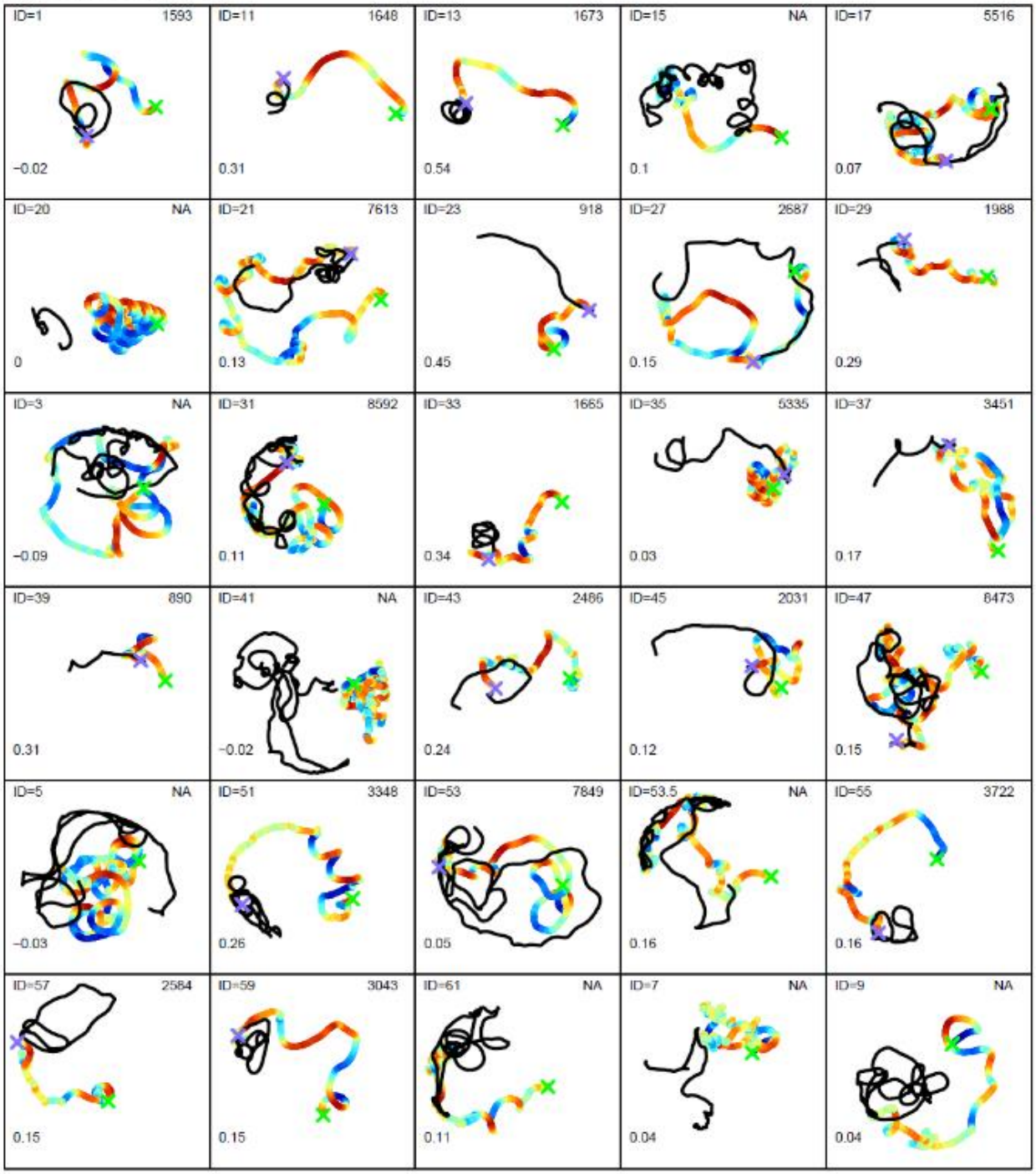

Impaired Free Moving *fog-2* female Search
in PHD Neuron Laser Ablated males

# PHD-laser Ablated

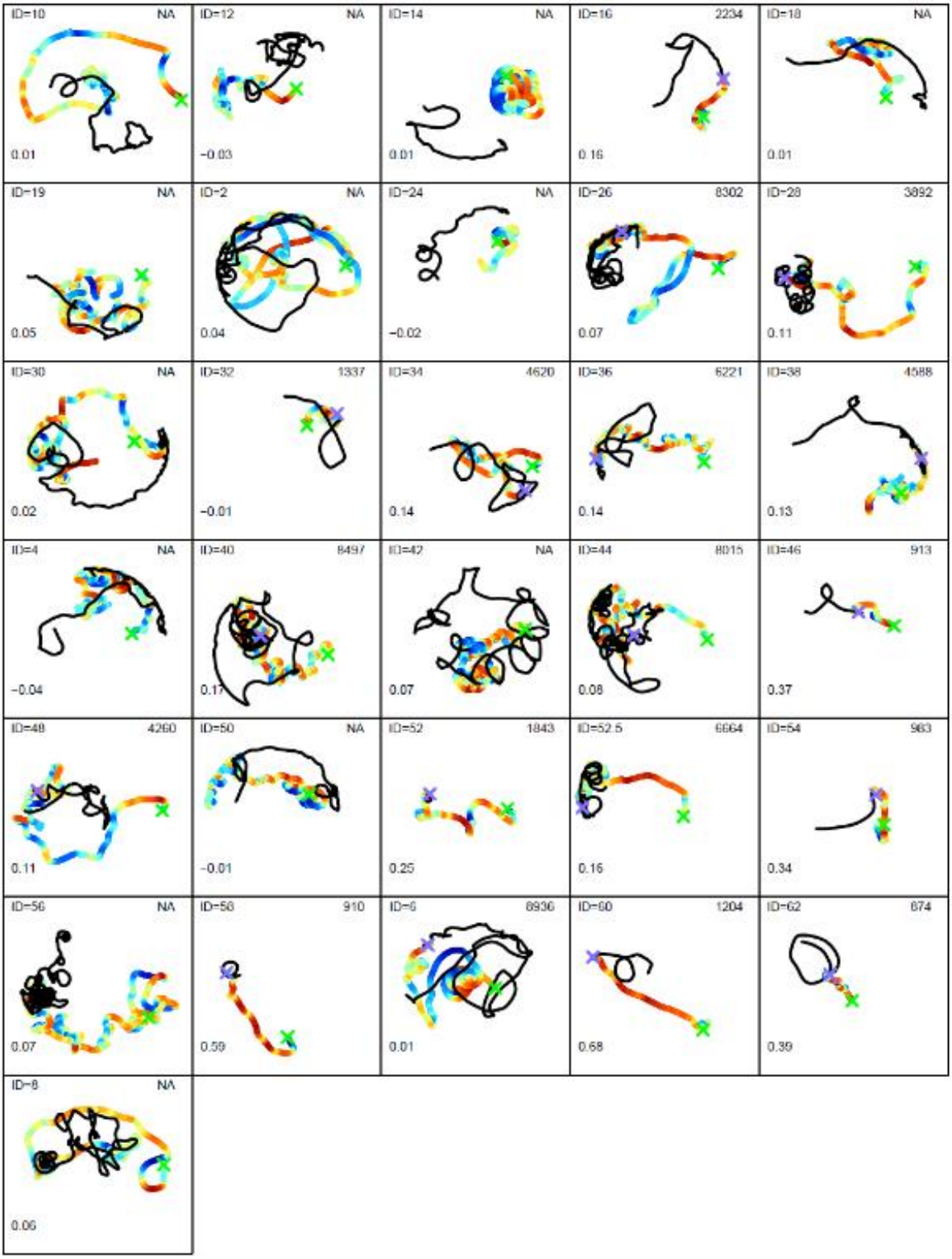


1429

**Figure S4: Navigational deficits in PHD neuron laser-ablated males during *fog-2* female tracking.** Depicts behavioral assays evaluating the impact of PHD neuron ablation on the ability of male *C. elegans* to locate freely moving *fog-2* mutant females. The experiments underscore the essential function of PHD neurons in facilitating accurate mate detection during natural mate-searching behaviors. Behavioral tests were carried out on 6-cm NGM agar plates inoculated with OP50 bacteria the previous night, providing a consistent experimental environment. Each assay involved placing a virgin adult *fog-2* female and a single male worm 2 cm apart on the same plate. Their interactions were recorded at 5 frames per second for a period of 30 mins or until the male succeeded in contacting the female, whichever occurred sooner. The black lines indicated the female trajectories, the color line indicated the male trajectory and the color scale indicated the mate attraction index. The figure illustrates individual movement paths for control (mock-treated) males versus males with PHD neurons laser ablated. The dataset includes trajectories from 30 mock-treated males and 31 males subjected to PHD neuron ablation, offering detailed insights into the behavioral ramifications of disrupting PHD neuron function.

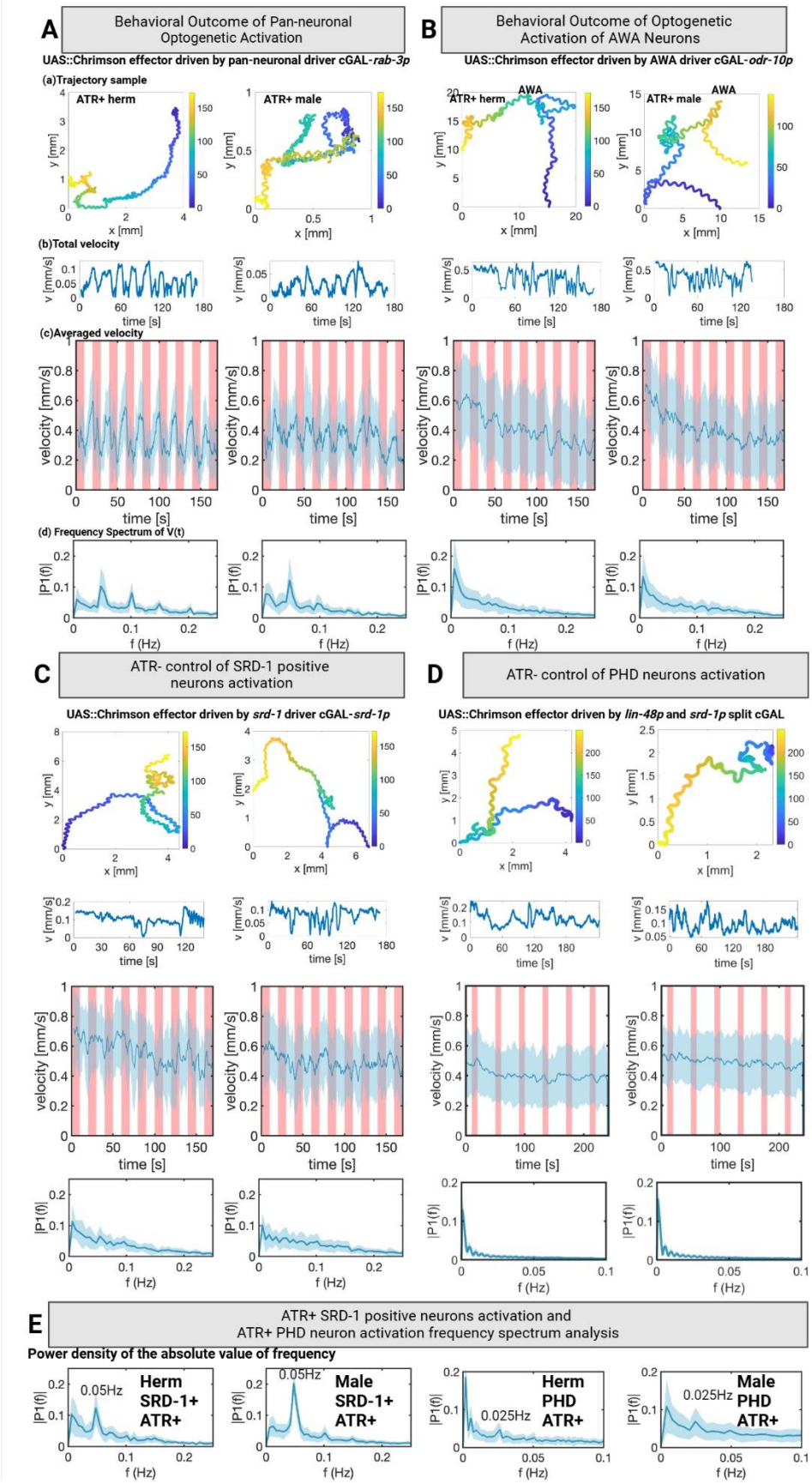
A
Behavioral Outcome of Pan-neuronal Optogenetic Activation
UAS::Chrimson effector driven by pan-neuronal driver cGAL-rab-3p
B
Behavioral Outcome of Optogenetic Activation of AWA Neurons
UAS::Chrimson effector driven by AWA driver cGAL-odr-10p
(a)Trajectory sample
ATR+ herm
ATR+ male
AWA
(b)Total velocity
(c)Averaged velocity
(d) Frequency Spectrum of V(t)
C
ATR- control of SRD-1 positive neurons activation
UAS::Chrimson effector driven by srd-1 driver cGAL-srd-1p
D
ATR- control of PHD neurons activation
UAS::Chrimson effector driven by lin-48p and srd-1p split cGAL
E
ATR+ SRD-1 positive neurons activation and ATR+ PHD neuron activation frequency spectrum analysis
Power density of the absolute value of frequency
0.05Hz
Herm SRD-1+ ATR+
Male SRD-1+ ATR+
0.025Hz
Herm PHD ATR+
Male PHD ATR+

1463

**Figure S5: Effects of Pan-Neural and AWA Neuron Activation on *C. elegans* Locomotion and ATR- Control of SRD-1 Positive Neuron and PHD Neuron Activation. (A)** Demonstrates global neuronal activation via the Chrimson system in *C. elegans*, employing a pan-neuronal promoter (*rab-3p*-NLS-cGAL driver) to drive UAS::Chrimson effector expression. This approach achieved effective neuronal stimulation across the nervous system in both male and female worms, leading to a temporary cessation of movement during light exposure, with immediate resumption of normal behavior upon cessation of the stimulus. The frequency of movement cessation closely followed the stimulation protocol, showing a dominant frequency at 0.05Hz, indicating the system's effectiveness in modulating worm locomotion through pan-neural activation. **(B)** Explores the specific activation of AWA neurons and its impact on locomotion in both sexes of *C. elegans*, utilizing a targeted cGAL-UAS system (*odr-10p*-NLS-cGAL driver for AWA specificity) to activate AWA neurons. Contrary to the pan-neural activation results, selective stimulation of AWA neurons did not alter the average velocity of the worms during a 20-second period of light exposure. This outcome suggests that AWA neuron activation alone may not be sufficient to initiate forward movement, or it may reflect limitations in the activation efficacy of the *odr-10* promoter used. Notably, the frequency analysis of this experimental setup did not exhibit the expected peak at 0.05Hz. The figure includes (a)(b) a representative trajectory sample alongside its total velocity time series V(t), with the red line marking periods of light stimulation; (c) the averaged V(t) across 30 samples, highlighted by a red shade during light stimulation; and (d) the frequency spectrum of V(t), illustrating the differential response patterns to pan-neural versus AWA-specific activation. The sample size for the pan-neural activation assay included 50 worms per sex, while the AWA activation assay involved 110-120 worms per sex. Error bars represent the std. **(C)** Locomotor responses to SRD-1 positive neuron activation in both sexes of *C. elegans*. SRD-1 positive neurons (*srd-1*P-NLS-cGAL driver) were activated in both sexes using Chrimson (UAS::Chrimson effector). The control, without all-trans retinal (ATR), had no change in behavior, eliminating any light effects. **(D)** Locomotor responses to PHD neuron activation in both sexes of *C. elegans*. PHD neurons (split cGAL-UAS line: *lin-48d*P-NLS-cGAL (DBD); *srd-1*P-NLS-cGAL (AD) driver) were activated in both sexes using Chrimson (UAS::Chrimson effector). The control, without all-trans retinal (ATR), also had no change in behavior, eliminating any light effects. **(E)** Frequency spectrum analysis of \( V(t) \) from Figure 2A and B demonstrates that optogenetic activation of SRD-1 positive neurons and PHD neurons produces expected peaks at 0.05 Hz and 0.025 Hz, corresponding to the 20-second and 40-second stimulation intervals, respectively.

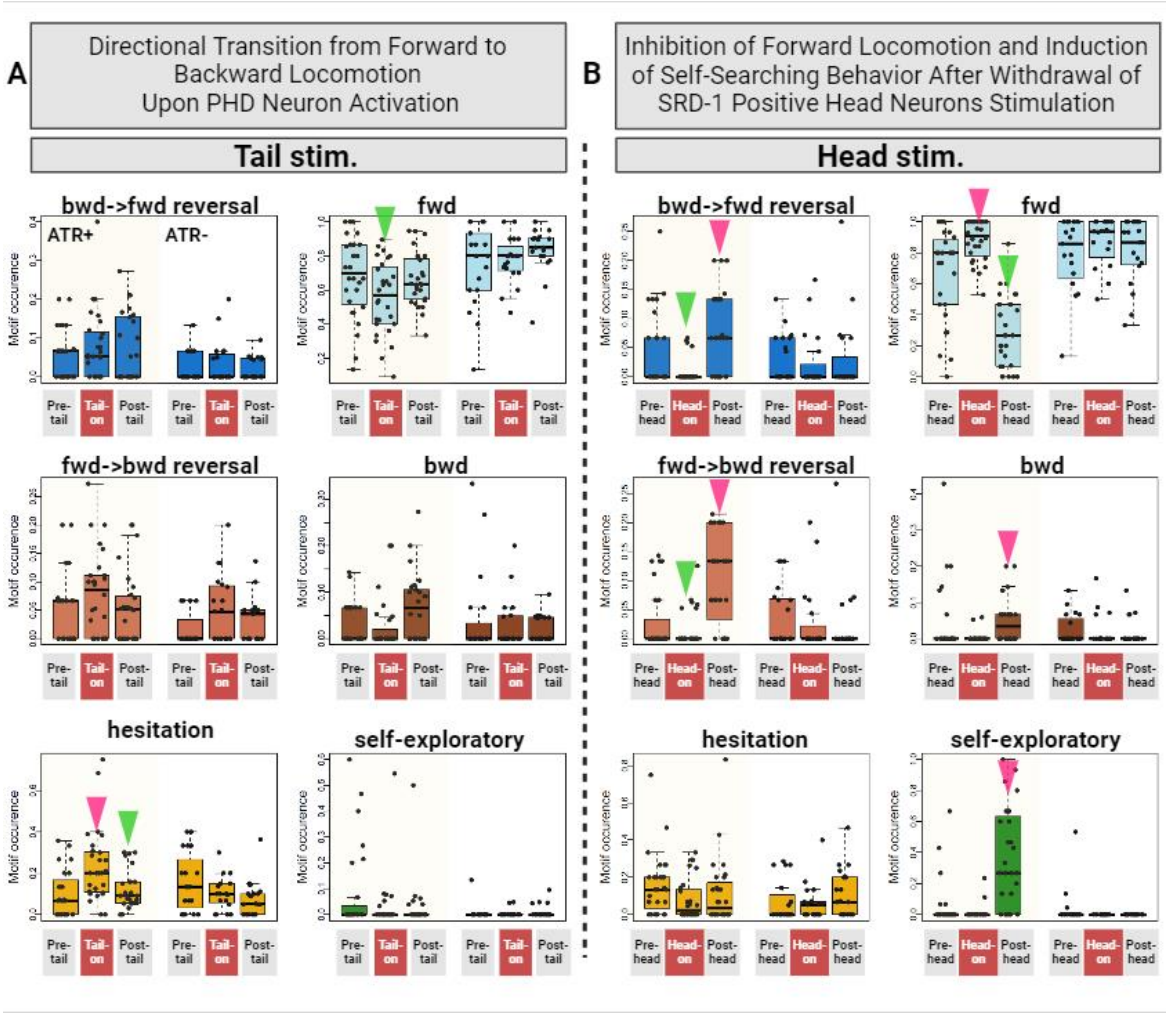


**Figure S6: Differential locomotion responses to optogenetic stimulation of SRD-1 positive neurons in male *C. elegans.*** Utilizes the *srd-1* Chrimson cGAL-UAS system for precise optogenetic stimulation of SRD-1 positive neurons in the head and tail regions of male *C. elegans*, revealing distinct locomotive responses. Tail-targeted light pulses induced transitions from forward to backward movement and hesitancy in movement direction. Continuous head stimulation resulted in sustained forward motion and exploratory post-stimulation behaviors. Experiment included ATR+ (n=18) and ATR- (n=12) groups, with sequential recording periods before, during, and after stimulation in both regions, to assess the nuanced impact on locomotion. **(A)** Tail activation effects on locomotion. A short light pulse targeting the tail induced a notable transition from forward to backward movement and increased hesitancy in movement direction during stimulation. **(B)** Head activation and subsequent behaviors. Continuous head stimulation for 30 seconds prompted sustained forward movement during light exposure and immediate directional adjustments post-stimulation. After head stimulation, males engaged in self-exploratory behaviors, using their tails for body probing. Each worm was recorded for 30 seconds before tail stimulation, followed by a 2-second alternating light pulse targeting the tail over 12 cycles. Post-tail stimulation, there was another 30-second recording period before initiating head stimulation, then the head stimulation lasted for 30 seconds. The worm was then recorded for an additional 30 seconds after the light stimulation concluded. Error bars represent the s.e.m.

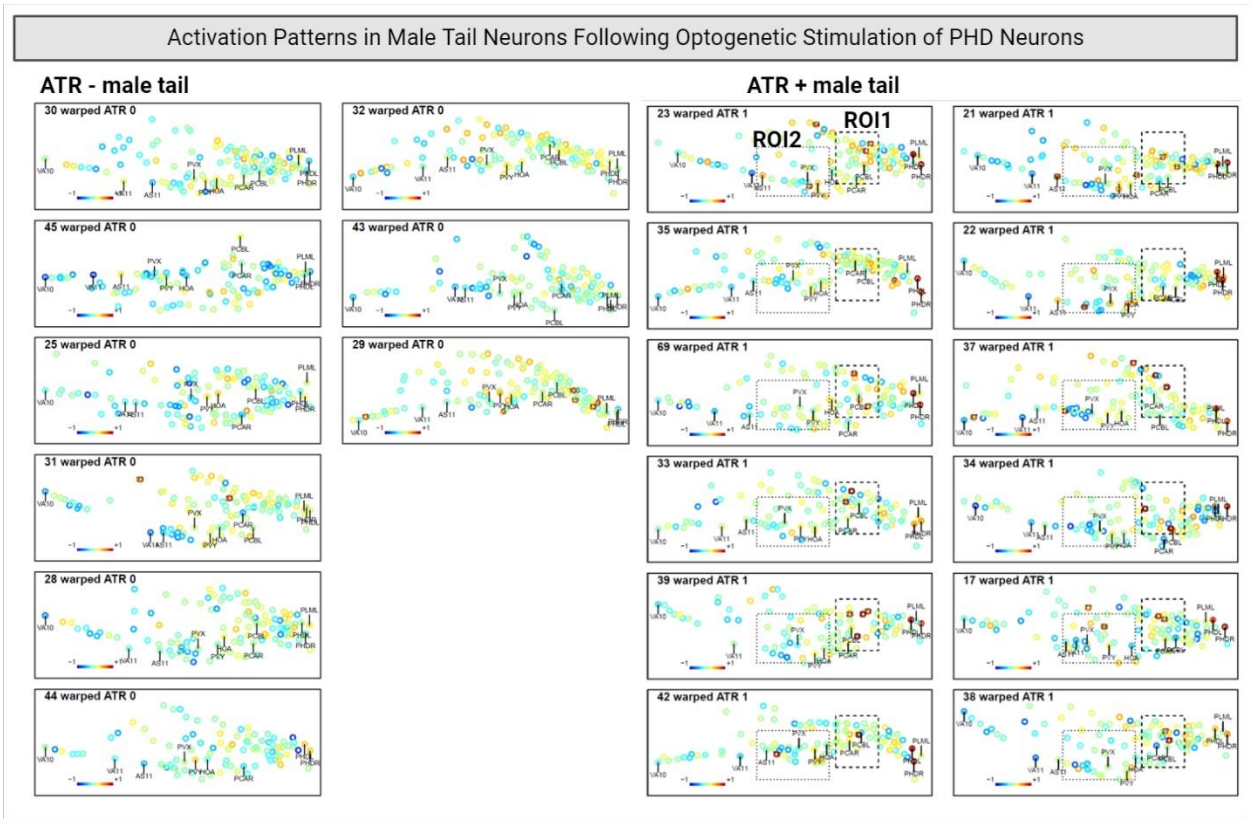


**Figure S7: Activation patterns observed in male tail neurons upon optogenetic stimulation of PHD neurons.** Visual analysis identified two regions, designated ROI1 and ROI2 in multiple males, which contain neurons with strong correlations to PHD activity in ATR+ group, but not ATR- group (correlation coefficient >0.55).

**Figure S8: Neural activity correlations with PHD optogenetic stimulation in tail regions.** Yellow and purple indicate positive correlations with target neuron activity in ATR- and ATR+ samples, respectively. Light green and green denote negative correlations in ATR- and ATR+ samples, respectively. Sample sizes: control (n=9) and experimental (n=12).

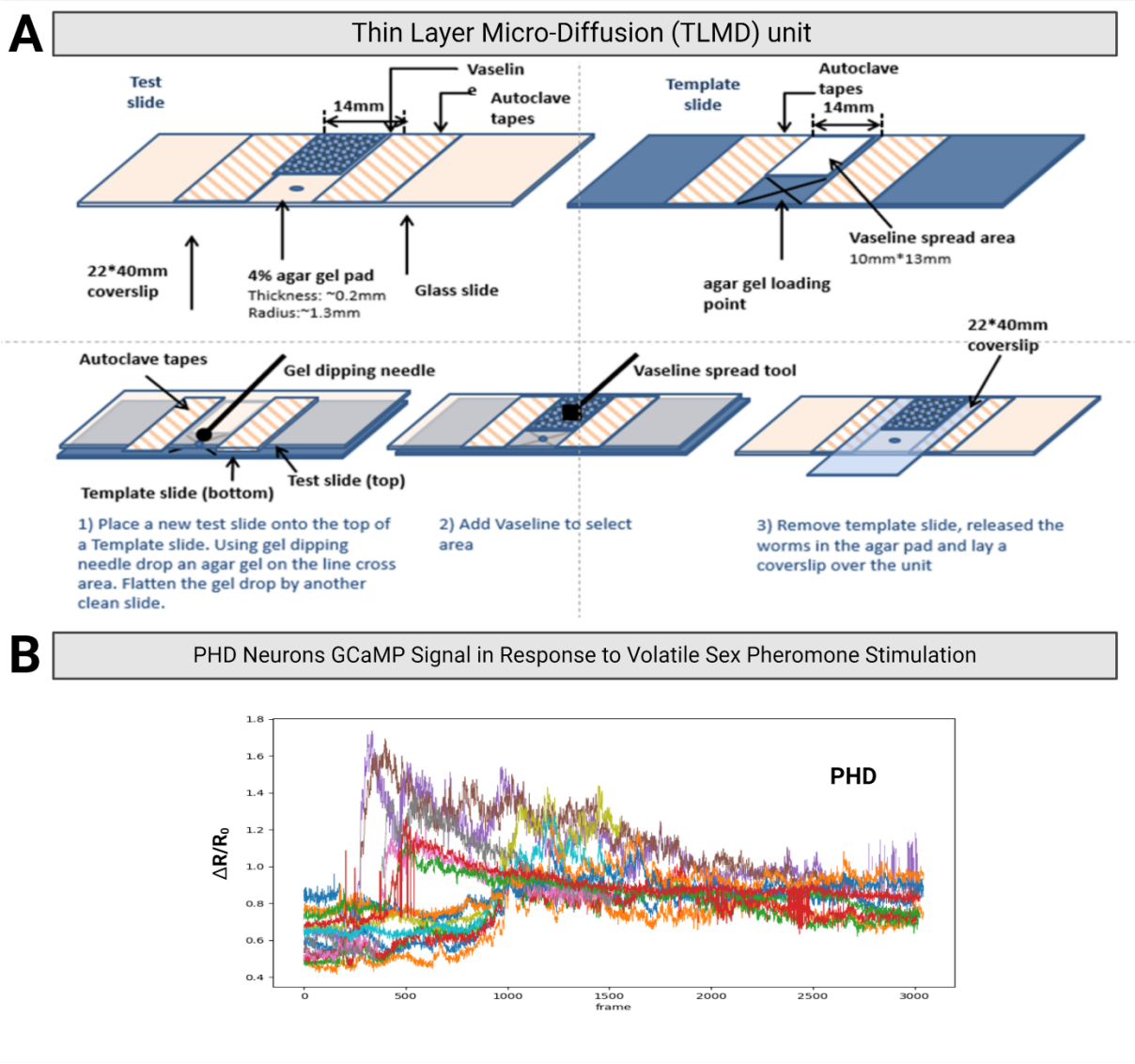


**Figure S9: TLMD unit for neuronal activation and calcium response measurement. (A)** Depicts the Thin Layer Micro-Diffusion (TLMD) unit setup for detecting changes in intracellular calcium signaling via GCaMP6s fluorescence intensity. The device consists of a 4% agarose pad placed between autoclave tapes, used with 0.2µl of 1mM levamisole to partially immobilize well-prepared transgenic worms. Test chemicals are introduced at 30 seconds, with rapid diffusion facilitated by capillary action. **(B)** Calcium responses of PHD neurons during 9.5 mins of pheromone stimulation, with individual animals distinguished by color coding. Experimental conditions were applied to control (n=5) and experimental (n=8) groups. Shaded areas represent the s.e.m.

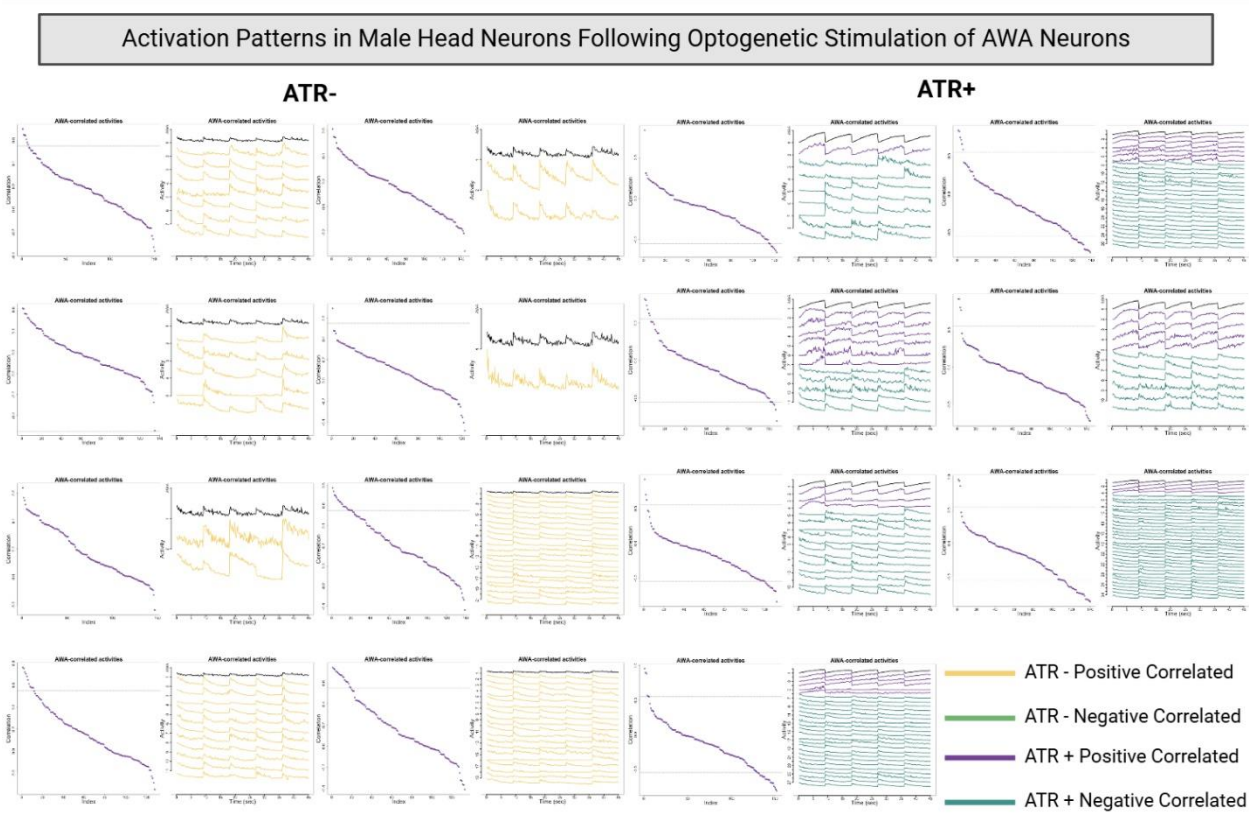


**Figure S10: Neural activity correlations with AWA and ASI optogenetic stimulation in head regions.** Yellow and purple indicate positive correlations with target neuron activity in ATR- and ATR+ samples, respectively. Light green and green denote negative correlations in ATR- and ATR+ samples, respectively. Sample sizes: control (n=8) and experimental (n=7).

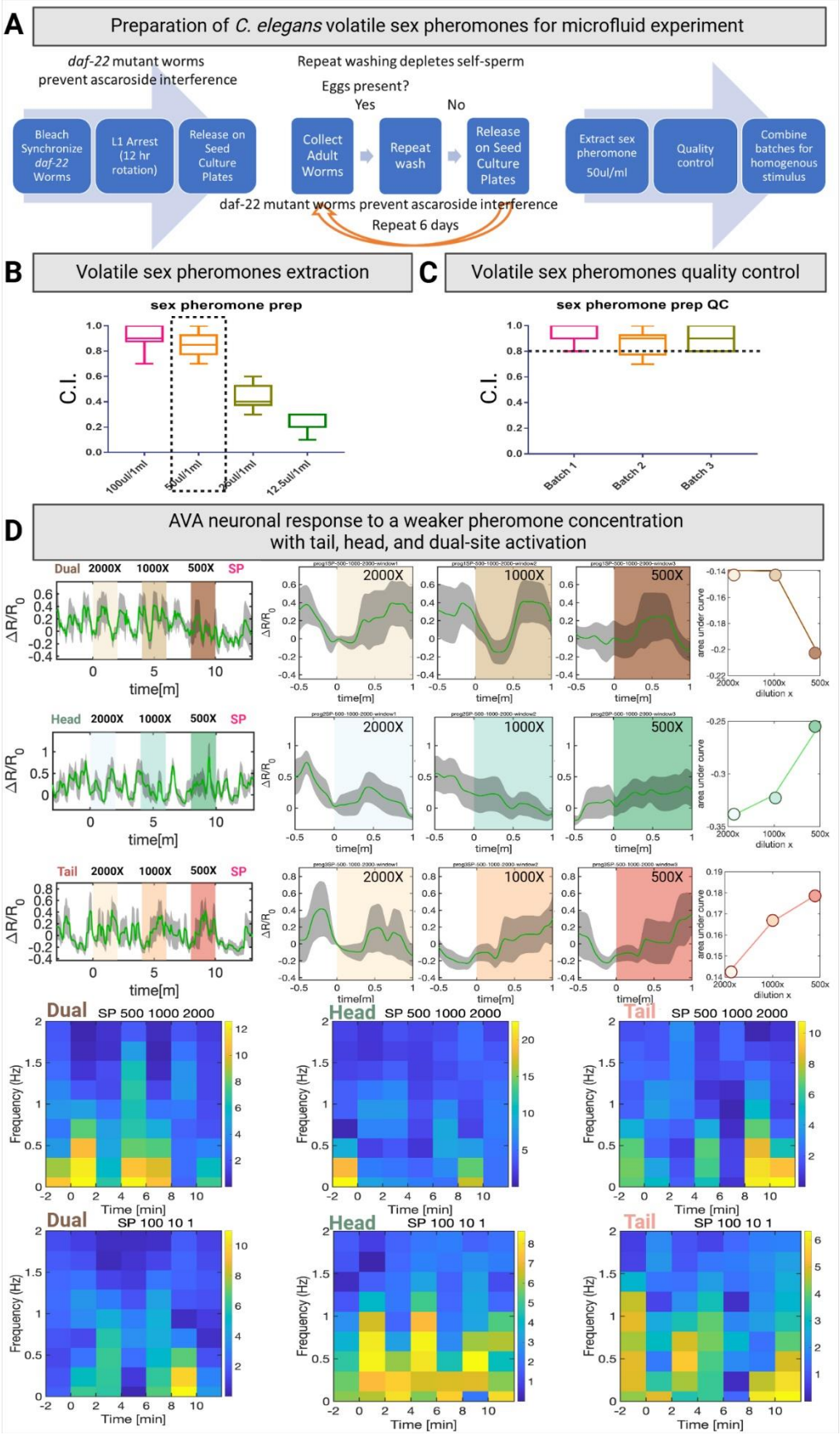
A
Preparation of C. elegans volatile sex pheromones for microfluid experiment
daf-22 mutant worms prevent ascaroside interference
Repeat washing depletes self-sperm
Eggs present?
Yes
No
Bleach Synchronize daf-22 Worms
L1 Arrest (12 hr rotation)
Release on Seed Culture Plates
Collect Adult Worms
Repeat wash
Release on Seed Culture Plates
Extract sex pheromone 50ul/ml
Quality control
Combine batches for homogenous stimulus
daf-22 mutant worms prevent ascaroside interference
Repeat 6 days
B
Volatile sex pheromones extraction
sex pheromone prep
C.I.
100ul/1ml
50ul/1ml
25ul/1ml
12.5ul/1ml
C
Volatile sex pheromones quality control
sex pheromone prep QC
C.I.
Batch 1
Batch 2
Batch 3
D
AVA neuronal response to a weaker pheromone concentration with tail, head, and dual-site activation
Dual
Head
Tail
2000X
1000X
500X
SP
ΔR/R0
time[m]
area under curve
dilution x
SP 500 1000 2000
SP 100 10 1
Frequency (Hz)
Time [min]

**Figure S11: Sex pheromone preparation for microfluidic experiment. (A)** Modified Sex Pheromone Extraction Protocol for Microfluidics. To obtain large quantities of crude sex pheromone for microfluidic experiments, we streamlined the standard protocol. We used *daf-22* mutant *C. elegans* hermaphrodites, eliminating confounding ascaroside signals. Worms were synchronized and repeatedly washed to deplete self-sperm, and the sex pheromone extraction ratio was optimized. **(B)** Ratio Optimization: We tested four ratios (100µl/ml, 50µl/ml, 25µl/ml, 12.5µl/ml) for their attractiveness to males using a chemoattraction assay. The 50µl/ml ratio exhibited attractiveness comparable to 100µl/ml, with attractiveness declining at lower concentrations. Therefore, 50µl/ml was chosen for sex pheromone extraction. **(C)** Quality Control and Homogenization: Three independent batches of extracted pheromone were quality-controlled using the chemoattraction assay, all exceeding a predetermined quality threshold suggested by previous studies (C.I. = 0.8). Finally, the quality-controlled batches were combined to create a homogenous stimulus for microfluidic experiments. (B) and (C) Error bars represent the s.e.m. **(D)** Effects of sex pheromone stimulation on AVA reversal command interneuron activity in *C. elegans* males at Higher Dilutions. The calcium indicator GCaMP6s was used to monitor calcium dynamics in the AVA neuron. The AVA-specific split cGAL driver construct consisted of gpa-14P::NLS::cGAL (DBD)::gp41-1::N-intein::let-858 3'UTR and rig-3P::NLS::gp41-1::C-intein::cGAL(AD)::let-858 3'UTR, paired with the GCaMP effector construct 15xUAS::GCaMP7b::SL2::mKate2. The upper panel shows the calcium-shaded areas representing the s.e.m. This set of microfluidic experiments used 500X, 1000X, and 2000X fold diluted pheromones. The right panel shows area-under-curve (AUC) analysis (see Method). The bottom panel displays oscillation frequency distributions, revealing spontaneous oscillations in AVA neuron activity upon exposure to 500X, 1000X, and 2000X diluted pheromones. Heatmaps represent the frequency responses of AVA neurons under varying stimulation conditions. Each panel corresponds to specific activation sites (head, tail, and dual activation) and serial pheromone dilutions (set 1: 1X, 10X, 100X; set 2: 500X, 1000X, 2000X). The heatmaps depict the oscillation frequency dynamics of AVA activity over 12 mins for each stimulus program, with color coding indicating the distribution and intensity of oscillation frequencies.

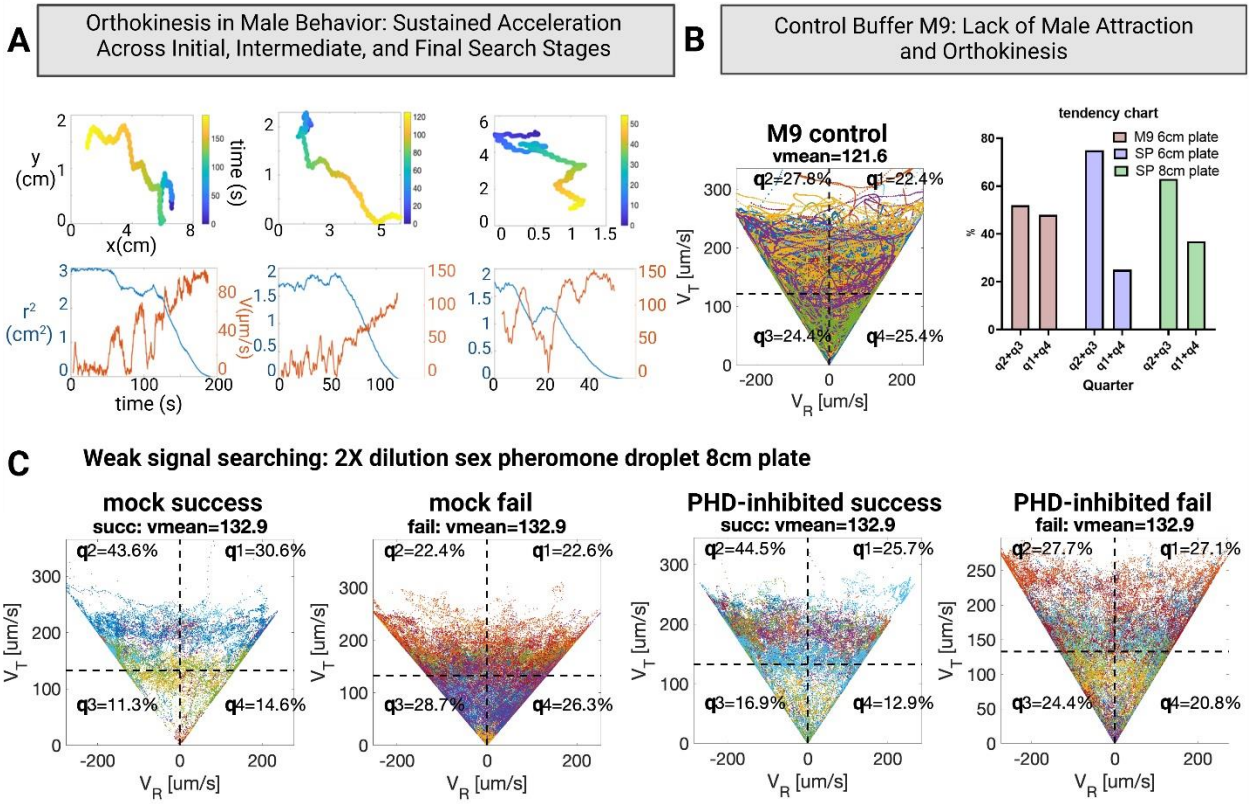


**Figure S12: Orthokinesis and trajectory analysis during sex pheromone navigation in *C. elegans* males. (A)** Additional sample of males accelerate as they approach source of pheromone. The top figure shows trajectory sample of WT adult males toward sex pheromone. In the bottom figure y-axis is squared distance from the pheromone source in blue color and absolute velocity [mm/s] plot in red color. Velocity adapts in response to concentration variations, as evidenced by the squared distance from the pheromone source. Velocity averaged over 20 frames. The sample size for the 8-cm plate study comprised 50 worms. **(B)** Demonstrates a predominance of trajectories moving towards the attractant in successful attempt subgroups compare with M9 buffer control and fail attempt subgroups, with a higher density of dots located on the left side (q2+q3) compared to the right side (q1+q4) in the dot display. This innovative analysis provides a nuanced alternative to the traditional chemotaxis index calculation. The dataset corresponds to that presented in Figure 8C (Male SP 8-cm Plate). **(C)** The dot display of trajectories for PHD-inhibited males in weak sex pheromone (2X diluted) signal search in 8-cm plate. Trajectories are segmented into 6.7-second intervals, with radial velocities on the x-axis and total velocities on the y-axis. The analysis employs a gating strategy focusing on mean total velocity and original positions for radial velocity assessment. The sample size for each data was comprised 60 worms.

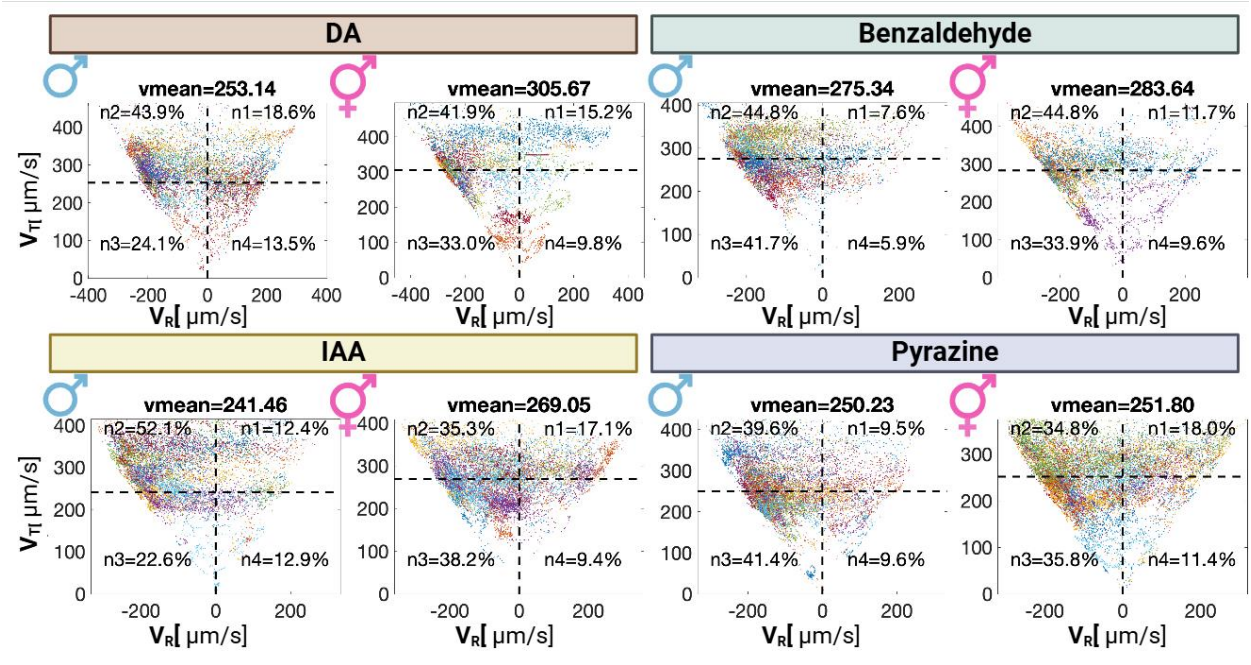


**Figure S13: Correlation between acceleration and attraction to volatile compounds in *C. elegans* in both sexes.** Presents an extended analysis of *C. elegans'* responses to additional volatile attractants, including pyrazine, diacetyl, benzaldehyde, and indole-3-acetic acid (IAA), revealing a significant positive correlation between acceleration and movement towards these chemicals in both sexes. This data further substantiates the role of orthokinesis in the navigational behavior of *C. elegans* towards volatile odor targets. Utilizing the same dot display analysis methodology as seen in Figures 7C, 7F, 7G, and S9A, this study underscores the consistency of orthokinetic responses across a range of attractive compounds in both sexes.

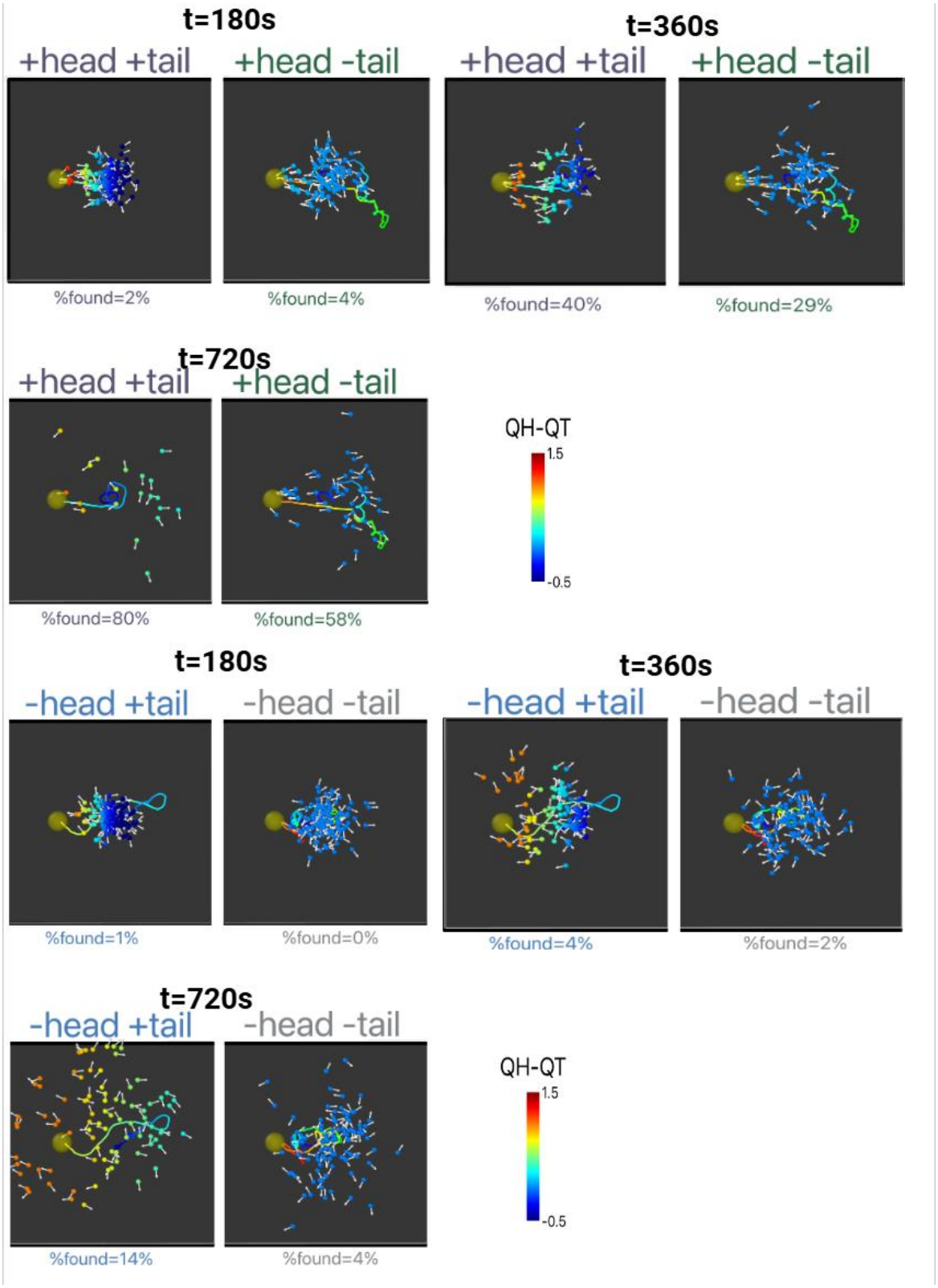


**Figure S14:** Each panel shows simulation snapshots comparing head/tail input-enabled conditions. In each snapshot with a time point, 100 randomly chosen worms from 10,000 stimulation events are displayed as spheres, colored by their instantaneous confidence $Q^H - Q^T$.

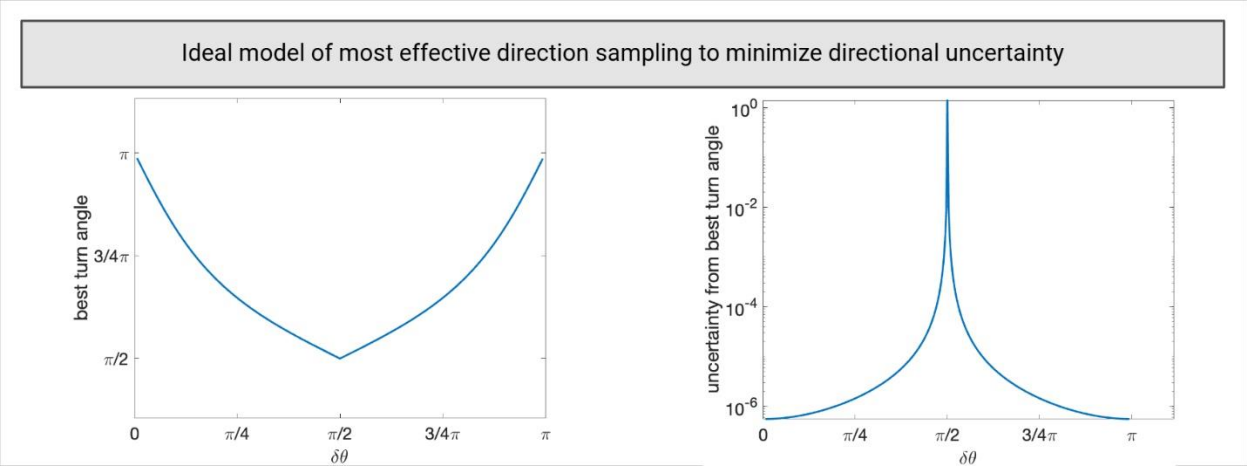


**Figure S15:** Ideal model for effective direction sampling to minimize directional uncertainty. δθ is the angle between the first sampled direction and the concentration gradient. The left panel shows the best angle to turn to sample the second direction. The right panel shows the directional uncertainty associated with the best turn angle. Averaging over an assumed uniform distribution of δθ results in a best turn angle close to 120 degrees.

**Supplementary video legends**

Video S1-4: *C. elegans* are represented by spheres, colored by their instantaneous confidence (QH-QT). Arrows indicate the head direction of each worm. A typical trajectory is displayed for each set of parameters, colored by the elapsed time. The transparent yellow region represents the pheromone droplet. Worms inside the droplet are deleted for visual clarity.

**Author contributions**

X.W. and P.W.S. conceived the study and designed the experiments. X.W. and V.S. performed the behavioral assays, imaging, and optogenetics experiments. T.Z. and X.W. developed the computational models and performed the data analysis. X.W. and A.G. performed the microfluidic experiment. C.F.P. provided a whole-brain imaging data analysis platform. X.W., T.Z., and P.W.S. wrote the initial draft of the manuscript. All authors discussed the results and contributed to the final version of the manuscript. P.W.S., A.D.T.S., and P.W.S. supervised the project.

**ACKNOWLEDGMENTS:**

We are grateful to David Aguirre, Wilber Palma, Stephanie Nava, and Zachary Blumenfeld for their contributions during the early stages of this project. We also thank Helena Casademunt and Nicholas Markarian for their discussion and suggestions during the manuscript preparation. Additionally, we acknowledge Elena Ruiz and Natalie Sim for data analysis. This work was supported by funding: R01 NS113119 (PWS, ADTS), a Tianqiao and Chrissy Chen senior postdoc fellowship, and the Tianqiao and Chrissy Chen Institute for Systems Neuroscience Awards.

**DISCLOSURES:**

The authors have no conflicts of interest to disclose.

**Data availability**

Source data are provided with this paper.

1687 **Code availability**

1688 All code for data analysis is available at https://github.com/edmondztt/pheromone-traj-analysis.

1689 **Reference list:**

1690


1691 1. Simon, J.M. and P.W. Sternberg, *Evidence of a mate-finding cue in the hermaphrodite nematode*
1692 *Caenorhabditis elegans.* Proceedings of the National Academy of Sciences, 2002. **99**(3): p. 1598-
1693 1603.
1694 2. Lipton, J., et al., *Mate searching in Caenorhabditis elegans: a genetic model for sex drive in a*
1695 *simple invertebrate.* The Journal of neuroscience : the official journal of the Society for
1696 Neuroscience, 2004. **24**(34): p. 7427-7434.
1697 3. Chasnov, J.R., et al., *The species, sex, and stage specificity of a Caenorhabditis sex pheromone.*
1698 Proceedings of the National Academy of Sciences of the United States of America, 2007. **104**(16):
1699 p. 6730-6735.
1700 4. Leighton, D.H., et al., *Communication between oocytes and somatic cells regulates volatile*
1701 *pheromone production in Caenorhabditis elegans.* Proc Natl Acad Sci U S A, 2014. **111**(50): p.
1702 17905-10.
1703 5. Wan, X., et al., *SRD-1 in AWA neurons is the receptor for female volatile sex pheromones in C.*
1704 *elegans males.* EMBO Rep, 2019. **20**(3).
1705 6. Lockery, S.R., *The computational worm: spatial orientation and its neuronal basis in C. elegans.*
1706 Current opinion in neurobiology, 2011. **21**(5): p. 782-790.
1707 7. Schone, H., *Spatial orientation: The spatial control of behavior in animals and man*. Vol. 588.
1708 2014: Princeton University Press.
1709 8. Grasso, F.W. and J.A. Basil, *How lobsters, crayfishes, and crabs locate sources of odor: current*
1710 *perspectives and future directions.* Current opinion in neurobiology, 2002. **12**(6): p. 721-727.
1711 9. Peckol, E.L., E.R. Troemel, and C.I. Bargmann, *Sensory experience and sensory activity regulate*
1712 *chemosensory receptor gene expression in Caenorhabditis elegans.* Proceedings of the National
1713 Academy of Sciences of the United States of America, 2001. **98**(20): p. 11032-11038.
1714 10. Ludewig, A.H., et al., *Pheromone sensing regulates Caenorhabditis elegans lifespan and stress*
1715 *resistance via the deacetylase SIR-2.1.* Proc Natl Acad Sci U S A, 2013. **110**(14): p. 5522-7.
1716 11. Golden, J.W. and D.L. Riddle, *A pheromone influences larval development in the nematode*
1717 *Caenorhabditis elegans.* Science, 1982. **218**(4572): p. 578-80.
1718 12. Butcher, R.A., et al., *Small-molecule pheromones that control dauer development in*
1719 *Caenorhabditis elegans.* Nature chemical biology, 2007. **3**(7): p. 420-422.
1720 13. Jeong, P.Y., et al., *Chemical structure and biological activity of the Caenorhabditis elegans dauer-*
1721 *inducing pheromone.* Nature, 2005. **433**(7025): p. 541-5.
1722 14. Butcher, R.A., et al., *A potent dauer pheromone component in Caenorhabditis elegans that acts*
1723 *synergistically with other components.* Proc Natl Acad Sci U S A, 2008. **105**(38): p. 14288-92.
1724 15. Aprison, E.Z. and I. Ruvinsky, *Counteracting Ascarosides Act through Distinct Neurons to*
1725 *Determine the Sexual Identity of C. elegans Pheromones.* Curr Biol, 2017. **27**(17): p. 2589-2599
1726 e3.
1727 16. Aprison, E.Z. and I. Ruvinsky, *Sex Pheromones of C. elegans Males Prime the Female Reproductive*
1728 *System and Ameliorate the Effects of Heat Stress.* PLoS Genet, 2015. **11**(12): p. e1005729.
1729 17. Kaplan, F., et al., *Ascaroside expression in Caenorhabditis elegans is strongly dependent on diet*
1730 *and developmental stage.* PLoS One, 2011. **6**(3): p. e17804.
1731 18. Srinivasan, J., et al., *A modular library of small molecule signals regulates social behaviors in*
1732 *Caenorhabditis elegans.* PLoS biology, 2012. **10**(1): p. e1001237.

19. Srinivasan, J., et al., *A blend of small molecules regulates both mating and development in Caenorhabditis elegans.* Nature, 2008. **454**(7208): p. 1115-1118.
20. Ludewig, A.H. and F.C. Schroeder, *Ascaroside signaling in C. elegans.* WormBook, 2013: p. 1-22.
21. Choe, A., et al., *Ascaroside signaling is widely conserved among nematodes.* Curr Biol, 2012. **22**(9): p. 772-80.
22. von Reuss, S.H., et al., *Comparative metabolomics reveals biogenesis of ascarosides, a modular library of small-molecule signals in C. elegans.* J Am Chem Soc, 2012. **134**(3): p. 1817-24.
23. Choe, A., et al., *Sex-specific mating pheromones in the nematode Panagrellus redivivus.* Proc Natl Acad Sci U S A, 2012. **109**(51): p. 20949-54.
24. Hsueh, Y.P., et al., *Nematode-trapping fungi eavesdrop on nematode pheromones.* Curr Biol, 2013. **23**(1): p. 83-6.
25. Pungaliya, C., et al., *A shortcut to identifying small molecule signals that regulate behavior and development in Caenorhabditis elegans.* Proc Natl Acad Sci U S A, 2009. **106**(19): p. 7708-13.
26. Izrayelit, Y., et al., *Targeted metabolomics reveals a male pheromone and sex-specific ascaroside biosynthesis in Caenorhabditis elegans.* ACS chemical biology, 2012. **7**(8): p. 1321-1325.
27. Fagan, K.A., et al., *A Single-Neuron Chemosensory Switch Determines the Valence of a Sexually Dimorphic Sensory Behavior.* Curr Biol, 2018. **28**(6): p. 902-914 e5.
28. Kato, S., et al., *Temporal responses of C. elegans chemosensory neurons are preserved in behavioral dynamics.* Neuron, 2014. **81**(3): p. 616-628.
29. Luo, L., et al., *Dynamic encoding of perception, memory, and movement in a C. elegans chemotaxis circuit.* Neuron, 2014. **82**(5): p. 1115-1128.
30. Wang, L., et al., *A gustatory neural circuit of Caenorhabditis elegans generates memory-dependent behaviors in Na+ chemotaxis.* Journal of Neuroscience, 2017. **37**(8): p. 2097-2111.
31. Satoh, Y., et al., *Regulation of experience-dependent bidirectional chemotaxis by a neural circuit switch in Caenorhabditis elegans.* Journal of Neuroscience, 2014. **34**(47): p. 15631-15637.
32. Kunitomo, H., et al., *Concentration memory-dependent synaptic plasticity of a taste circuit regulates salt concentration chemotaxis in Caenorhabditis elegans.* Nature communications, 2013. **4**(1): p. 2210.
33. Ji, N., et al., *Corollary discharge promotes a sustained motor state in a neural circuit for navigation.* Elife, 2021. **10**: p. e68848.
34. Venkatachalam, V., et al., *Pan-neuronal imaging in roaming Caenorhabditis elegans.* Proceedings of the National Academy of Sciences, 2016. **113**(8): p. E1082-E1088.
35. Zhen, M. and A.D. Samuel, *C. elegans locomotion: small circuits, complex functions.* Current opinion in neurobiology, 2015. **33**: p. 117-126.
36. Chalasani, S.H., et al., *Dissecting a circuit for olfactory behaviour in Caenorhabditis elegans.* Nature, 2007. **450**(7166): p. 63-70.
37. Gray, J.M., J.J. Hill, and C.I. Bargmann, *A circuit for navigation in Caenorhabditis elegans.* Proceedings of the National Academy of Sciences, 2005. **102**(9): p. 3184-3191.
38. Larsch, J., et al., *A circuit for gradient climbing in C. elegans chemotaxis.* Cell Reports, 2015. **12**(11): p. 1748-1760.
39. Dobosiewicz, M., Q. Liu, and C.I. Bargmann, *Reliability of an interneuron response depends on an integrated sensory state.* Elife, 2019. **8**: p. e50566.
40. Luo, L., et al., *Bidirectional thermotaxis in Caenorhabditis elegans is mediated by distinct sensorimotor strategies driven by the AFD thermosensory neurons.* Proceedings of the National Academy of Sciences, 2014. **111**(7): p. 2776-2781.
41. Colbert, H.A. and C.I. Bargmann, *Environmental signals modulate olfactory acuity, discrimination, and memory in Caenorhabditis elegans.* Learning & memory (Cold Spring Harbor, N.Y.), 1997. **4**(2): p. 179-191.

42. Wen, J.Y.M., et al., *Mutations that prevent associative learning in C. elegans.* Behavioral neuroscience, 1997. **111**(2): p. 354.
43. Saeki, S., M. Yamamoto, and Y. Iino, *Plasticity of chemotaxis revealed by paired presentation of a chemoattractant and starvation in the nematode Caenorhabditis elegans.* The Journal of experimental biology, 2001. **204**(Pt 10): p. 1757-1764.
44. Nuttley, W.M., K.P. Atkinson-Leadbeater, and D. Van Der Kooy, *Serotonin mediates food-odor associative learning in the nematode Caenorhabditiselegans.* Proceedings of the National Academy of Sciences of the United States of America, 2002. **99**(19): p. 12449-12454.
45. Zhang, Y., H. Lu, and C.I. Bargmann, *Pathogenic bacteria induce aversive olfactory learning in Caenorhabditis elegans.* Nature, 2005. **438**(7065): p. 179-184.
46. Vellai, T., et al., *Effects of sex and insulin/insulin-like growth factor-1 signaling on performance in an associative learning paradigm in Caenorhabditis elegans.* Genetics, 2006. **174**(1): p. 309-316.
47. Kauffman, A., et al., *C. elegans positive butanone learning, short-term, and long-term associative memory assays.* J Vis Exp, 2011(49).
48. Sakai, N., et al., *A sexually conditioned switch of chemosensory behavior in C. elegans.* PLoS One, 2013. **8**(7): p. e68676.
49. Stein, G.M. and C.T. Murphy, *C. elegans positive olfactory associative memory is a molecularly conserved behavioral paradigm.* Neurobiol Learn Mem, 2014. **115**: p. 86-94.
50. Hong, M., et al., *Early Pheromone Experience Modifies a Synaptic Activity to Influence Adult Pheromone Responses of C. elegans.* Curr Biol, 2017. **27**(20): p. 3168-3177 e3.
51. Gordus, A., et al., *Feedback from network states generates variability in a probabilistic olfactory circuit.* Cell, 2015. **161**(2): p. 215-227.
52. Albrecht, D.R. and C.I. Bargmann, *High-content behavioral analysis of Caenorhabditis elegans in precise spatiotemporal chemical environments.* Nature methods, 2011. **8**(7): p. 599-605.
53. Cheung, B.H., et al., *Experience-dependent modulation of C. elegans behavior by ambient oxygen.* Current Biology, 2005. **15**(10): p. 905-917.
54. Bretscher, A.J., et al., *Temperature, oxygen, and salt-sensing neurons in C. elegans are carbon dioxide sensors that control avoidance behavior.* Neuron, 2011. **69**(6): p. 1099-113.
55. Ryu, W.S. and A.D. Samuel, *Thermotaxis in Caenorhabditis elegans analyzed by measuring responses to defined thermal stimuli.* Journal of Neuroscience, 2002. **22**(13): p. 5727-5733.
56. Bargmann, C.I., *Chemosensation in C. elegans.* WormBook : the online review of C.elegans biology, 2006: p. 1-29.
57. Gabel, C.V., et al., *Neural circuits mediate electrosensory behavior in Caenorhabditis elegans.* Journal of Neuroscience, 2007. **27**(28): p. 7586-7596.
58. Sawin, E.R., R. Ranganathan, and H.R. Horvitz, *C. elegans locomotory rate is modulated by the environment through a dopaminergic pathway and by experience through a serotonergic pathway.* Neuron, 2000. **26**(3): p. 619-631.
59. Pierce-Shimomura, J.T., T.M. Morse, and S.R. Lockery, *The fundamental role of pirouettes in Caenorhabditis elegans chemotaxis.* Journal of Neuroscience, 1999. **19**(21): p. 9557-9569.
60. Iino, Y. and K. Yoshida, *Parallel use of two behavioral mechanisms for chemotaxis in Caenorhabditis elegans.* Journal of Neuroscience, 2009. **29**(17): p. 5370-5380.
61. Miller, A.C., et al., *Step-response analysis of chemotaxis in Caenorhabditis elegans.* Journal of Neuroscience, 2005. **25**(13): p. 3369-3378.
62. Zariwala, H.A., et al., *Step response analysis of thermotaxis in Caenorhabditis elegans.* Journal of Neuroscience, 2003. **23**(10): p. 4369-4377.
63. Hilliard, M.A., C.I. Bargmann, and P. Bazzicalupo, *C. elegans responds to chemical repellents by integrating sensory inputs from the head and the tail.* Current Biology, 2002. **12**(9): p. 730-734.

64. Gat, A., et al., *Integration of spatially opposing cues by a single interneuron guides decision-making in C. elegans.* Cell Reports, 2023. **42**(9).
65. Quintin, S., et al., *Distinct mechanisms underlie H2O2 sensing in C. elegans head and tail.* Plos one, 2022. **17**(9): p. e0274226.
66. Gat, A., et al., *Integration of spatially opposing cues by a single interneuron guides decision making in C. elegans.* bioRxiv, 2023: p. 2023.01. 23.525194.
67. Troemel, E.R., et al., *Divergent seven transmembrane receptors are candidate chemosensory receptors in C. elegans.* Cell, 1995. **83**(2): p. 207-218.
68. Yi, W., J.M. Ross, and D. Zarkower, *Mab-3 is a direct tra-1 target gene regulating diverse aspects of C. elegans male sexual development and behavior.* Development, 2000. **127**(20): p. 4469-80.
69. Molina-García, L., et al., *Direct glia-to-neuron transdifferentiation gives rise to a pair of male-specific neurons that ensure nimble male mating.* Elife, 2020. **9**: p. e48361.
70. Susoy, V., et al., *Natural sensory context drives diverse brain-wide activity during C. elegans mating.* Cell, 2021. **184**(20): p. 5122-5137. e17.
71. Sengupta, P., J.H. Chou, and C.I. Bargmann, *odr-10 encodes a seven transmembrane domain olfactory receptor required for responses to the odorant diacetyl.* Cell, 1996. **84**(6): p. 899-909.
72. Ferkey, D.M., P. Sengupta, and N.D. L'Etoile, *Chemosensory signal transduction in Caenorhabditis elegans.* Genetics, 2021. **217**(3): p. iyab004.
73. Im Choi, J., et al., *Odor-dependent temporal dynamics in Caenorhabitis elegans adaptation and aversive learning behavior.* PeerJ, 2018. **6**: p. e4956.
74. Bargmann, C.I., E. Hartwieg, and H.R. Horvitz, *Odorant-selective genes and neurons mediate olfaction in C. elegans.* Cell, 1993. **74**(3): p. 515-527.
75. Tran, A., et al., *C. elegans avoids toxin-producing Streptomyces using a seven transmembrane domain chemosensory receptor.* Elife, 2017. **6**: p. e23770.
76. Zhou, Y., et al., *Potential Nematode Alarm Pheromone Induces Acute Avoidance in Caenorhabditis elegans.* Genetics, 2017. **206**(3): p. 1469-1478.
77. Chasnov, J.R., et al., *The species, sex, and stage specificity of a Caenorhabditis sex pheromone.* Proc Natl Acad Sci U S A, 2007. **104**(16): p. 6730-5.
78. Klapoetke, N.C., et al., *Independent optical excitation of distinct neural populations.* Nature methods, 2014. **11**(3): p. 338-346.
79. Cook, S.J., et al., *Whole-animal connectomes of both Caenorhabditis elegans sexes.* Nature, 2019. **571**(7763): p. 63-71.
80. Cohen, N. and J.E. Denham, *Whole animal modeling: piecing together nematode locomotion.* Current Opinion in Systems Biology, 2019. **13**: p. 150-160.
81. Kato, S., et al., *Global brain dynamics embed the motor command sequence of Caenorhabditis elegans.* Cell, 2015. **163**(3): p. 656-669.
82. Meng, J., et al., *A tonically active master neuron modulates mutually exclusive motor states at two timescales.* 2023.
83. Choi, M.-K., et al., *NMDAR-mediated modulation of gap junction circuit regulates olfactory learning in C. elegans.* Nature Communications, 2020. **11**(1): p. 3467.
84. Marvin, J.S., et al., *An optimized fluorescent probe for visualizing glutamate neurotransmission.* Nature methods, 2013. **10**(2): p. 162-170.
85. Schimansky-Geier, L., et al., *Structure formation by active Brownian particles.* Physics Letters A, 1995. **207**(3-4): p. 140-146.
86. Berg, H.C., *E. coli in Motion*. 2004: Springer.
87. Anderson, J.L., L.T. Morran, and P.C. Phillips, *Outcrossing and the maintenance of males within C. elegans populations.* Journal of heredity, 2010. **101**(suppl_1): p. S62-S74.

88. Barriere, A. and M.A. Felix, *High local genetic diversity and low outcrossing rate in Caenorhabditis elegans natural populations.* Curr Biol, 2005. **15**(13): p. 1176-84.
89. Kawano, T., et al., *Lifespan extending activity of substances secreted by the nematode Caenorhabditis elegans that include the dauer-inducing pheromone.* Biosci Biotechnol Biochem, 2005. **69**(12): p. 2479-81.
90. Noguez, J.H., et al., *A novel ascaroside controls the parasitic life cycle of the entomopathogenic nematode Heterorhabditis bacteriophora.* ACS Chem Biol, 2012. **7**(6): p. 961-6.
91. Kiontke, K.C., et al., *A phylogeny and molecular barcodes for Caenorhabditis, with numerous new species from rotting fruits.* BMC evolutionary biology, 2011. **11**: p. 1-18.
92. Ross, J.A., et al., *Caenorhabditis briggsae recombinant inbred line genotypes reveal inter-strain incompatibility and the evolution of recombination.* PLoS genetics, 2011. **7**(7): p. e1002174.
93. Page, J.L., et al., *Staying the course: chemical signal spatial properties and concentration mediate cross-stream motion in turbulent plumes.* Journal of Experimental Biology, 2011. **214**(9): p. 1513-1522.
94. Gomez-Marin, A., et al., *Mechanisms of odor-tracking: multiple sensors for enhanced perception and behavior.* Frontiers in cellular neuroscience, 2010. **4**: p. 1374.
95. Borst, A. and M. Heisenberg, *Osmotropotaxis in Drosophila melanogaster.* Journal of comparative physiology, 1982. **147**(4): p. 479-484.
96. Budick, S.A. and M.H. Dickinson, *Free-flight responses of Drosophila melanogaster to attractive odors.* Journal of experimental biology, 2006. **209**(15): p. 3001-3017.
97. Taylor, S.R., et al., *Molecular topography of an entire nervous system.* Cell, 2021. **184**(16): p. 4329-4347.e23.
98. Yemini, E., et al., *NeuroPAL: a multicolor atlas for whole-brain neuronal identification in C. elegans.* Cell, 2021. **184**(1): p. 272-288. e11.
99. Vidal, B., et al., *An atlas of Caenorhabditis elegans chemoreceptor expression.* PLoS Biol, 2018. **16**(1): p. e2004218.
100. Pereira, L., et al., *Timing mechanism of sexually dimorphic nervous system differentiation.* Elife, 2019. **8**.
101. Ibarra-Soria, X., et al., *The olfactory transcriptomes of mice.* PLoS genetics, 2014. **10**(9): p. e1004593.
102. Gomez-Diaz, C. and R. Benton, *The joy of sex pheromones.* EMBO Rep, 2013. **14**(10): p. 874-83.
103. Kohl, J., et al., *A bidirectional circuit switch reroutes pheromone signals in male and female brains.* Cell, 2013. **155**(7): p. 1610-1623.
104. Schindelin, J., et al., *Fiji: an open-source platform for biological-image analysis.* Nature methods, 2012. **9**(7): p. 676-682.
105. Wolff, C., et al., *Multi-view light-sheet imaging and tracking with the MaMuT software reveals the cell lineage of a direct developing arthropod limb.* Elife, 2018. **7**: p. e34410.
106. Park, C.F., et al., *Automated neuron tracking inside moving and deforming C. elegans using deep learning and targeted augmentation.* Nature Methods, 2024. **21**(1): p. 142-149.
107. Berg, S., et al., *Ilastik: interactive machine learning for (bio) image analysis.* Nature methods, 2019. **16**(12): p. 1226-1232.
108. Nava, S., et al., *A cGAL-UAS bipartite expression toolkit for Caenorhabditis elegans sensory neurons.* Proceedings of the National Academy of Sciences, 2023. **120**(51): p. e2221680120.
109. Pokala, N., et al., *Inducible and titratable silencing of Caenorhabditis elegans neurons in vivo with histamine-gated chloride channels.* Proc Natl Acad Sci U S A, 2014. **111**(7): p. 2770-5.
110. Cao, M., et al., *Application of the red-shifted channel rhodopsin Chrimson for the Caenorhabditis elegans cGAL bipartite system.* MicroPubl Biol, 2018. **2018**.

111. Schild, L.C. and D.A. Glauser, *Dual color neural activation and behavior control with chrimson and CoChR in Caenorhabditis elegans.* Genetics, 2015. **200**(4): p. 1029-1034.
112. Lu, Y., et al., *Extrasynaptic signaling enables an asymmetric juvenile motor circuit to produce symmetric undulation.* Current Biology, 2022. **32**(21): p. 4631-4644. e5.
113. Gower, J.C., *Generalized procrustes analysis.* Psychometrika, 1975. **40**: p. 33-51.
114. Wood, S.N., *Thin plate regression splines.* Journal of the Royal Statistical Society Series B: Statistical Methodology, 2003. **65**(1): p. 95-114.
115. Orfanidis, S.J., *Introduction to signal processing*. 1995: Prentice-Hall, Inc.
116. Zhou, T., et al., *AI-aided geometric design of anti-infection catheters.* Science Advances, 2024. **10**(1): p. eadj1741.
117. Chronis, N., M. Zimmer, and C.I. Bargmann, *Microfluidics for in vivo imaging of neuronal and behavioral activity in Caenorhabditis elegans.* Nature methods, 2007. **4**(9): p. 727-731.
118. Pinkard, H., et al., *Pycro-Manager: open-source software for customized and reproducible microscope control.* Nature methods, 2021. **18**(3): p. 226-228.
119. Appleby, P.A., *The role of multiple chemotactic mechanisms in a model of chemotaxis in C. elegans: different mechanisms are specialised for different environments.* Journal of computational neuroscience, 2014. **36**: p. 339-354.